Time-Resolved Photoelectron Diffraction

Dissertation

zur

Erlangung der naturwissenschaftlichen Doktorwürde
(Dr. sc. nat.)

vorgelegt der

Mathematisch-naturwissenschaftlichen Fakultät

der

Universität Zürich

von

Michael Eberhard Greif
aus Deutschland

Promotionskomitee

Prof. Dr. Jürg Osterwalder
Dr. Matthias Hengsberger
Prof. Dr. Peter Krüger

Zürich 2015

Abstract

The natural time scale of nuclear motion is the femtosecond time scale. In this dissertation a route towards the measurement of structural dynamics with femtosecond time and atomic spatial resolution is presented, in order to follow nuclear motion in real time. The method developed here is time-resolved photoelectron diffraction.
Photoelectron diffraction is a method that probes the structure in the vicinity of the emitter atom. When an electron is emitted through light irradiation, it follows an unscattered and a scattered path through the crystal. Both paths have fixed phase relations in the detection plane and therefore their amplitudes add to an angle dependent interference pattern that carries information about the local crystal structure around the emitter. By selecting the scanned electron energy emitters can be discriminated by their chemical nature.
With the combination of photoelectron diffraction with light pulses from higher harmonics generation (HHG), a pump-probe scheme becomes possible, in which the fundamental IR wavelength acts as pump pulse and the higher harmonic pulses in the extreme ultraviolet (XUV) are used to excite the photoelectrons.
In the first chapters apart from the methodology like photoelectron diffraction and pump-probe measurements the technical setup of the experiments is outlined. In a following chapter routines for the recording of photoelectron diffraction measurements with a wide angle lens (WAL) electron analyzer are presented. It is shown how the x-ray photoelectron diffraction (XPD) map of a Bi 4f core level from a Bi(111) crystal is recorded with the 2-dimensional detector and how the detector coordinates are projected on the spherical coordinates of the crystal system. Moreover binning routines are presented that account for oversampling effects. The efficiency of the 2D detection scheme and its routines are underlined by a comparison of measurement durations of full XPD maps between the WAL detector and a conventional channeltron detector. It comes out that recording times can be faster by a factor of ten, provided the same measurement geometry is maintained. Additionally a Cu Fermi surface map is recorded with ultraviolet (uv) light and gives proof that the recording procedures can also be applied to do angle-resolved photoelectronelectron spectroscopy (ARPES).
In a next chapter the sensitivity of not only XPD but also ultraviolet photoelectron diffraction (UPD) is demonstrated by measurements of the geometric structure of tin-phthalocyanine (SnPc) molecules adsorbed on a Ag(111) surface. It is demonstrated that XPD and UPD are complementary methods. While structural parameters such as azimuthal rotation and flattening of the basket shaped molecules upon adsorption can be identified with XPD, the mean bond distance between the tin atom and the surface ($d_{Sn-Ag} = 2.30$ Å) can be obtained from UPD measurements.
The ability of UPD to measure structural parameters with sub-Ångstrom resolution is a key requirement to use the method for time-resolved experiments in the subsequent chapter: By intense IR laser pulses a displacive excitation of coherent phonons (A_{1g} mode) in Bi(111) is triggered. In delay scans between IR pump and XUV probe pulses oscillations of electron density on the

one hand and UPD signal on the other hand can be observed. At normal emission well known cosine-like oscillations of the electronic density of states (DOS) around the Fermi energy are observed. At a polar angle of $\theta = 50°$ in the $\bar{\Gamma}\bar{\mathrm{K}}$ direction a part of the UPD map from the fully integrated valence band is measured. The phase of the oscillation in the UPD signal is shifted by π with respect to the one observed at normal emission and thus directly follows the nuclear motion of the lattice. Single scattering cluster (SSC) calculations reproduce the signal oscillation found in this region of the Brillouin zone. Tight binding calculations of the phonon dependent DOS alone cannot explain the magnitude of the oscillation at this angular position. This highlights that transient structural effects measured via time-resolved UPD play an important role here. In another measurement states close to the L and X point of the Brillouin zone are compared, showing a change of phase again. The UPD signal might be dominating at locations where only few electronic states are available.
In the final chapter a theory study of time-dependent XPD is shown, that also gives an outlook to future perspectives of the method. A pump-probe experiment is simulated in which a 2 THz pulse resonantly excites CO molecules adsorbed on a Pt(111) surface. The excitation results in a coherent wagging motion of the molecules that can be probed by XPD. Excitation and coherent movement are simulated with density functional theory (DFT) and molecular dynamics (MD) calculations and the XPD measurement is simulated applying SSC calculations. Averaging over 50 different molecular trajectories shows that during excitation the CO molecules align azimuthally and coherently oscillate with increasing amplitudes of the hindered translational mode. After the pulse has passed, the molecules relax, what can be seen in an increasing azimuthal isotropy. This way a molecular movie in real time is simulated.

Zusammenfassung

Die natürliche Zeitskala, auf der sich Atomkerne in Festkörpern bewegen, ist die Femtosekundenzeitskala. Diese Dissertation handelt von der Umsetzung einer Messmethode, die das Ziel verfolgt strukturelle Veränderungen mit Femtosekundenzeit- und mit atomarer räumlicher Auflösung zu messen. Somit kann die Bewegung von Atomrümpfen in Echtzeit verfolgt werden. Die dabei verwendete Methode heißt zeitaufgelöste Photoelektronendiffraktion.
Durch Photoelektronenbeugung ist es möglich, die Struktur in der atomaren Umgebung des Photoemitters zu messen. Dabei macht man sich zunutze, dass ein Elektron, das durch Photonenabsorption emittiert wird, mehrere Wege verfolgen kann, bevor es die Probe verlässt, um detektiert zu werden. Das Elektron kann entweder direkt, ohne mit den Nachbaratomen zu streuen, in den Detektor gelangen oder es wird an den Nachbaratomen gestreut. Da zwischen direkter und gestreuter Elektronenwelle eine feste Phasenbeziehung erhalten ist, summieren sich die Amplituden der Wellen entlang einzelner Pfade kohärent und in der Detektionsebene entsteht ein winkelabhängiges Interferenzmuster.
Indem man die Energie der detektierten Elektronen wählt, kann man bestimmen, welche Art von Emitteratomen hinsichtlich ihrer atomaren Umgebung untersucht werden soll. Dies ist möglich, da das emittierende Atom abhängig von der Elementart Elektronen mit charkteristischer Energie entsendet.
Um die Methode zeitaufgelöst zu betreiben, verwendet man eine Pump-Abfrage Technik. In diesem Fall wird das untersuchte System mit infrarotem (IR) Licht angeregt, also gepumpt, und mit ultraviolettem (UV) Licht abgefragt. Die UV-Laserpulse werden durch die Erzeugung höherer harmonischer Schwingungen der fundamentalen IR-Wellenlänge (HHG) erzeugt. Die Abfrage besteht aus einer Messung des Elektronenbeugungssignals und wird mit variierender Verzögerung zum Pumppuls gemessen.
In den ersten Kapiteln werden neben einer methodischen Einführung Aufbau und Durchführung des Experiments beschrieben. In einem darauffolgenden Kapitel werden Abläufe beschrieben, um mit einem zweidimensionalen Elektronenanalysator mit einer Weitwinkellinse Elektronendiffraktionsmuster zu messen. Als Beispiel dient die Aufnahme des Beugungsmusters eines Bi 4f Rumpfni-veaus von einem Bi(111)-Kristall. Es werden Formeln für eine Projektion der Detektorkoordinaten auf die Kugelkoordinaten des Kristallsystems entwickelt und darüberhinaus eine Prozedur, um Werte von mehrfach detektierten Emissionsrichtungen zu mitteln. Das Ergebnis zeigt, dass unter gleichbleibender Messgeometrie mit einem Weitwinkellinsenanalysator zehn mal schneller gemessen werden kann, als mit einem konventionellen Channeltrondetektor. Weiterhin wird demonstriert, dass sämtliche Prozeduren auch für winkelaufgelöste Elektronenspektroskopie verwendet werden können, wie anhand der Aufnahme einer Cu-Fermifläche gezeigt wird.
Im anschließenden Kapitel wird Photoelektronenbeugung sowohl mit Röntgen- (XPD), als auch mit ultravioletem (UPD) Licht verwendet, um speziell das Potential von UPD hinsichtlich der Bestimmung von Strukturparametern zu testen; dazu werden Zinn-Phthalocyanine (SnPc) auf

Ag(111) adsorbiert. In dem Kapitel wird gezeigt, dass die Kombination von XPD und UPD komplementäre Ergebnisse liefert. Mit XPD kann die azimuthale Ausrichtung der Adsorbatmoleküle sowie ein Abflachen der urspünglich konvexen Moleküle beobachtet werden. UPD hingegen liefert zusätzlich den mittleren Bindungsabstand der Zinnatome vom Silbersubstrat ($d_{Sn-Ag} = 2.30$Å). Da mithilfe der UPD-Methode Strukturen mit sub-Ångstrom-Auflösung bestimmt werden können, eignet sich diese, um im darauffolgenden Kapitel zur zeitaufgelösten Methode erweitert zu werden. Mit intensiven Infrarotpulsen werden in einem Bi(111)-Kristall kohärente Phononen (A_{1g}-Mode) durch Verschieben der Elektronendichte angeregt. Mit den höherharmonischen UV-Pulsen wird in Normalemission, in Abhängigkeit der Verzögerung zwischen IR und UV, die wohlbekannte kosinusartige Oszillation der elektronischen Zustandsdichte (DOS) im Bereich der Fermienergie beobachtet. Bei einem größeren Polarwinkel $\theta = 50°$ kann in $\bar{\Gamma}\bar{\mathrm{K}}$-Richtung eine Oszillation von Teilen des UPD-Signals vom vollständig integrierten Valenzband gemessen werden. Dabei zeigt sich, dass die Phase der UPD-Signalschwingung um π gegenüber der Schwingung der elektronischen Struktur bei Normalemission verschoben ist. Somit folgt die gemessene Schwingung direkt der Auslenkung der einzelnen Gitteratome. Dieses Schwingungsverhalten des zeitaufgelösten UPD-Signals wird durch "single scattering cluster"-Rechnungen (SSC) bestätigt. Weiterhin wird mittels des "tight binding"-Modells die DOS-Schwingung in Abhängigkeit der Gitterauslenkung berechnet, wobei sich zeigt, dass die Stärke der Oszillation nicht allein durch "tight binging"-Rechnungen erklärt werden kann. Daher spielen Änderungen der Gitterstruktur, wie sie mit zeitaufgelöstem UPD gemessen werden, eine wichtige Rolle. Zusätzlich werden in einer weiteren Messung Zustände in der Nähe des L- und X-Punktes der Brillouinzone gemessen. Ein Vergleich zeigt, dass dort, wo wenige Zustände in der Bandstruktur verfügbar sind, möglicherweise wieder UPD-Effekte bemerkbar sind.
Im letzten Kapitel wird schließlich eine Theoriebetrachtung zu zeitaufgelöstem XPD angestellt, was zugleich als Ausblick für mögliche Anwendungen gilt. Es wird ein Pump-Abfrage Experiment simuliert, in dem ein 2 THz-Puls CO-Moleküle auf einer Pt(111)-Oberfläche zu kohärenten Kippschwingungen anregt. Mit XPD kann ein zeitlich variierendes Signal gemessen werden. Anregung und kohärente Schwingung werden durch Rechnungen mittels der Dichtefunktionaltheorie (DFT) und Molekulardynamik-Rechnungen (MD), die XPD-Messung durch SSC-Rechnungen simuliert. Eine Mittelung über 50 verschiedene Molekültrajektorien zeigt, dass sich die Moleküle durch die Anregung azimuthal ausrichten und mit zunehmender Amplitude der Kippschwingung kohärent zu oszillieren beginnen. Nachdem der Puls vorüber ist, relaxieren die Moleküle, wobei die azimuthale Ordnung zunehmend verloren geht, also isotroper wird. Auf diese Weise wird der Film einer Molekülbewegung in Echtzeit simuliert.

Contents

1 Introduction

"If you want to understand function, study structure," Francis Crick the co-discoverer of the DNA structure has supposedly said [1]. This statement emphasizes the importance of structural analysis on atomic scales. However structural determination of smaller objects like cellular tissue, molecular or even atomic structure demands the aid of technical devices. It has been achieved to resolve single atoms using various methods like atomic force or scanning tunneling microscopy. Moreover structural parameters of solids with sub-Ångstom resolution can also be found using x-ray diffraction or electron diffraction.
But an important aspect the term "function" implies, is dynamics. So in order to follow physical and chemical processes on the atomic scale in real time, atomic resolution has to be combined with femtosecond time-resolution, as the natural scale of nuclear motion is the femtosecond timescale. In the 1980s through pioneering work by Zewail and others, the field of femtochemistry was developed and it became possible to follow structural dynamics like the dissociation of molecules in real time, *i. e.* with femtosecond time-resolution [2]. In the nineties first works appeared, in which structural dynamics were recorded in a very direct way using ultrafast electron diffraction with a resolution of only a few picoseconds [3, 4]. In those measurements the structural changes of molecules in the gas phase were recorded. The dynamics of the structural changes were followed by using the well established pump-probe method, in which femtosecond laser pulses served as pump and picosecond electron pulses as probe. Later, ultrafast electron diffraction was further developed to resolve structural dynamics on the femtosecond scale [5].
Now a direct method existed to follow nuclear dynamics in real time and the generation of a molecular movie came within reach. Such a powerful tool enables the observation of chemical processes as they occur in real time. This makes the identification of key reactive modes in complex reactions possible, thereby revealing insight into function of complex molecules [6].
However time resolution of ultrafast electron diffraction was limited by the temporal width of the electron pulses. With the advent of pulsed x-rays for example by the use of slicing techniques [7] the tools for time-resolved x-ray diffraction were existing. With femtosecond x-ray pulses as probe, the time-resolution of measurements could further be improved but only at the cost of lower scattering cross sections compared to electron diffraction. Still progress was soon reported about ultrafast structural measurements with femtosecond time-resolution. Processes such as lattice strain propagation and solid-liquid phase transitions were observed [8, 9].
The present dissertation about time-resolved photoelectron diffraction also pursues the goal to show measurements of time-resolved structural dynamics on the femtosecond time scale. The method joins advantages of both electron and x-ray diffraction. With the diffracted particles also being electrons, large cross sections are combined with a time-resolution that is only limited by the duration of few-femtoseconds laser pulses. Thus photoelectron diffraction, a method renowned for its powerful abilities to resolve structure with atomic resolution [10–12], is extended to a time-resolved method using a pump-probe setup. Instead of using pulsed x-rays, XUV laser pulses from

higher harmonics generation (HHG) with durations of a few femtosecond are applied [13, 14].
The route towards the realization of the measurement is described stepwise. In a first step a new chamber including a wide angle lens 2D electron analyzer had to be set up. Subsequently the performance of the analyzer and its capability to measure angle resolved spectra is demonstrated. Thereby the projection of the detector coordinates onto spherical coordinates of the crystal system are derived.
In the next step the sensitivity of photoelectron diffraction in the ultraviolet (UPD) and in the x-ray regime (XPD) is tested in experiments with SnPc adsorbed on a Ag(111) surface. Since structural parameters of the system could be derived with sub-Ångstrom resolution, UPD is then extended to time-resolved measurements.
The realization of a proof of principle measurement applying time-resolved UPD is shown. With IR pulses as pump, coherent optical phonons (A_{1g}) in a Bi(111) crystal are excited and the time-dependent structural changes are probed with UPD using pulsed XUV light from HHG. Thus nuclear motion can be followed in a very direct way and with femtosecond time-resolution.
Finally a theoretical study shows how the method can be further expanded into the x-ray regime to follow the resonantly excited wagging motion of CO molecules adsorbed on Pt(111). The periodic motion of the carbon atoms becomes visible as another version of a molecular movie. For a realization of this study THz pump and x-ray probe pulses are required as they are soon available at the Paul Scherrer Institute for example [15].

2 Methodology

2.1 Photoelectron Spectroscopy

One of the fundamental findings that demonstrated the limits of classical physics and paved the way for modern quantum mechanics, was that of the particle-wave dualism of light. The observation of the photo-electric effect by Heinrich Hertz in 1887 [16] and its explanation by Albert Einstein in 1905 [17] established the view on light, to be either particle or wave, depending on which experiment was conducted. In case of the photo-electric effect Einstein assumed that light consists of discrete particles, namely photons, that are able to transfer enough energy to electrons in order to emit them from solids. The equation

$$E_{kin} = h\nu - E_B - \Phi \tag{2.1}$$

describes the residual kinetic energy E_{kin} of a photo-emitted electron after absorption of a photon with energy $E_p = h\nu$ and having overcome the binding energy E_B and the work function Φ. Commonly E_B is taken with respect to the Fermi energy E_F, *i. e.* $E_B = 0$ eV, if it equals the Fermi energy.

Three step model The process of photon absorption itself can be described in different ways. First the semi-classical and intuitive three-step model for solids is outlined here [18]. The three steps of the model include

1. Absorption of the photon $h\nu$ that leads to an electronic transition from a bound initial state $|\psi_i\rangle$ with binding energy E_B to a final state $|\psi_f\rangle$ with kinetic energy $E_{kin,s}$ in the solid. $E_{kin,s}$ refers to its zero at the bottom of the valence band E_0.

2. Transport of the electron as wave with wave vector $\boldsymbol{k} = \sqrt{2mE_{kin,s}/\hbar^2}$ through the solid. Thereby the wave can scatter inelastically and is damped exponentially. The damping constant is the inelastic mean free path (IMFP).

3. Transition from the solid into the vacuum. The wave has to overcome the surface potential step $V_0 = \Phi + (E_F - E_0)$, which causes a reduction of the $\boldsymbol{k}_\perp$ component of $\boldsymbol{k}$ and leaves the $\boldsymbol{k}_\parallel$ component unchanged, resulting in a refraction at the surface. $E_F - E_0$ is the difference between bottom of the valence band and the Fermi energy. Waves with too small $\boldsymbol{k}_\perp$ cannot escape.

Finally the kinetic energy outside the crystal is $E_{kin,v} = E_{kin,s} - V_0$. To relate the refracted angle of the electron emission direction outside the solid θ with the one inside θ', the relation $\frac{\hbar^2 k^2}{2m} = E$

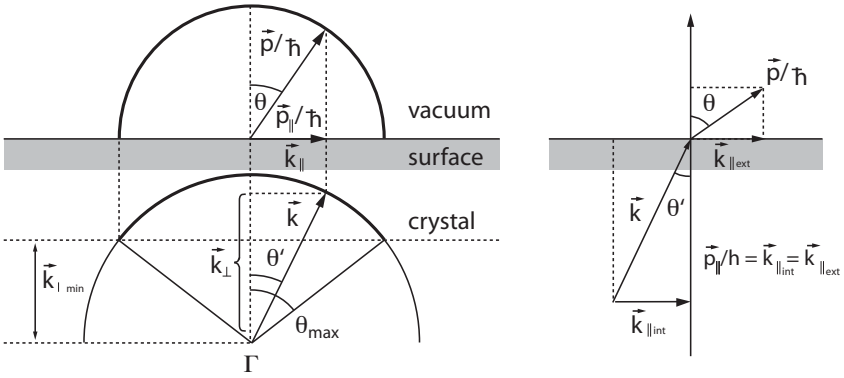

Figure 2.1: Emission and refraction of electrons at the surface. (All vectors are displayed in bold letters) *Left*: Electrons with $\boldsymbol{k}$ inside the solid lose part of the $\boldsymbol{k}_\perp$ component when leaving the solid. $\boldsymbol{k}_\parallel$ is conserved. The thick lines indicate the escape cone inside and outside of the crystal, where particles with $\boldsymbol{k}_\perp < \boldsymbol{k}_{\perp,min}$ cannot escape. *Right*: Snell's law for electrons crossing the surface. The figure is taken from [19]

is used to express Snell's law for electrons on surfaces:

$$\sin\theta = \sin\theta' \sqrt{\frac{E_{kin,v} + V_0}{E_{kin,v}}}. \tag{2.2}$$

As a consequence the wave vector components inside the solid can be written as:

$$\boldsymbol{k}_\parallel = \frac{1}{\hbar}\sqrt{2mE_{kin,v}}\sin\theta \qquad \boldsymbol{k}_\perp = \frac{1}{\hbar}\sqrt{2m(E_{kin,v}+V_0)}\cos\theta' \tag{2.3}$$

It becomes obvious that the inner potential V_0 has to be known in order to measure the dispersion relation $E(k_\perp)$. Figure 2.1 illustrates the electron transition into vacuum.

Quantum mechanical description Later in a quantum mechanical theory the light matter interaction was described by the Schrödinger equation applying an electric field with vector potential $\mathbf{A}(\mathbf{r},t)$ on an electron wave function $\psi(\mathbf{r},t)$ [20]:

$$i\hbar\frac{\partial}{\partial t}\psi(\mathbf{r},t) = \Big(\frac{1}{2m}\big(\mathbf{p}(\mathbf{r}) - \frac{e}{c}\mathbf{A}(\mathbf{r},t)\big)^2 + \hat{V}(\mathbf{r})\Big)\psi(\mathbf{r},t) = H\psi(\mathbf{r},t) \tag{2.4}$$

Assuming weak electric fields ($\mathbf{A}^2(\mathbf{r},t) \approx 0$) and taking advantage of the Coulomb gauge ($\mathbf{p}(\mathbf{r}) \cdot \mathbf{A}(\mathbf{r},t) \propto \nabla \cdot \mathbf{A}(\mathbf{r},t) = 0$) leaves

$$H = \frac{\mathbf{p}(\mathbf{r})^2}{2m} + V(\mathbf{r}) - \frac{e}{mc}\mathbf{A}(\mathbf{r},t)\cdot\mathbf{p}(\mathbf{r}) = H_0 + H_{int} \tag{2.5}$$

with

$$H_{int} = -\frac{e}{mc}\mathbf{A}_0(\mathbf{r})e^{i(\mathbf{kr}-\omega t)}\mathbf{p}(\mathbf{r}) \tag{2.6}$$

reflecting the oscillatory behavior of the electric field. Thus the wave functions are not stationary anymore and electron transitions become possible. Due to the weak-field assumption perturbation

theory can be applied and leads to Fermi's golden rule, expressing the transition probability between initial and final state:

$$W_{if} = \frac{2\pi}{\hbar} |\underbrace{\langle \psi_f | H_{int} | \psi_i \rangle}_{M_{if}}|^2 \cdot \delta(E_f - E_i - h\nu) \tag{2.7}$$

The δ-function makes sure energy is conserved and M_{if} is the so-called transition matrix element. In its explicit form it now reads:

$$M_{if} = -\frac{e}{mc} \boldsymbol{A}_0(\boldsymbol{r}) \langle\, \psi_f \mid e^{i(\boldsymbol{kr}-\omega t)} \boldsymbol{p(r)} \mid \psi_i \,\rangle \tag{2.8}$$

$$\approx -\frac{e}{mc} \boldsymbol{A}_0(\boldsymbol{r}) e^{-i\omega t} \langle\, \psi_f \mid 1 \cdot \boldsymbol{p(r)} \mid \psi_i \,\rangle \tag{2.9}$$

In equation (2.9) large enough wave lengths are assumed so that $\boldsymbol{kr} \ll 1$. Relevant distances $\boldsymbol{r}$ are of the order of atomic dimensions [21]. Then only the first term of the Taylor expansion of the exponential term $e^{i\mathbf{kr}}$ is used (**dipole approximation**). To express M_{if} in the typical dipole form using the position operator $\boldsymbol{r}$ some mathematical transformations have to be done. First one has to show that the identity

$$\boldsymbol{p(r)} = \frac{im}{\hbar}[H_0, \boldsymbol{r}] \tag{2.10}$$

holds, with $[H_0, \boldsymbol{r}]$ as the commutator between the unperturbed Hamiltonian and the position operator [21].

$$\begin{aligned}
\big[H_0, \boldsymbol{r}\big]\psi &= \Big[\, \frac{1}{2m}\boldsymbol{p(r)}^2 + V(\boldsymbol{r}), \boldsymbol{r}\Big]\psi \\
&= \Big(\big(\frac{1}{2m}\boldsymbol{p(r)}^2 + V(\boldsymbol{r})\big)\boldsymbol{r} - \boldsymbol{r}\big(\frac{1}{2m}\boldsymbol{p(r)}^2 + V(\boldsymbol{r})\big)\Big)\psi \\
&= -\frac{\hbar^2}{2m}(\nabla\nabla\boldsymbol{r} - \boldsymbol{r}\nabla\nabla)\psi \\
&= -\frac{\hbar^2}{2m}(\nabla(\psi + \boldsymbol{r}\nabla\psi) - \boldsymbol{r}\nabla\nabla\psi) \\
&= -\frac{\hbar^2}{2m}(\nabla\psi + \nabla\psi + \boldsymbol{r}\nabla\nabla\psi - \boldsymbol{r}\nabla\nabla\psi) \\
&= -\frac{\hbar^2}{m}\nabla\psi \\
\Rightarrow \big[H_0, \boldsymbol{r}\big] &= \frac{\hbar}{im}\boldsymbol{p(r)} \qquad\qquad \square
\end{aligned} \tag{2.11}$$

Substituting eq. (2.10) into eq. (2.9) leads to

$$\begin{aligned}
M_{if} &= -\frac{ie}{\hbar c}\boldsymbol{A}_0(\boldsymbol{r}) e^{-i\omega t} \langle\, \psi_f \mid \big[H_0, \boldsymbol{r}\big] \mid \psi_i \,\rangle \\
&= -\frac{ie}{\hbar c}\boldsymbol{A}_0(\boldsymbol{r}) e^{-i\omega t} \big(\langle\, \psi_f \mid E_f \boldsymbol{r} \mid \psi_i \,\rangle - \langle\, \psi_f \mid \boldsymbol{r} E_i \mid \psi_i \,\rangle \big) \\
&= -\frac{ie}{c}\frac{(E_f - E_i)}{\hbar}\boldsymbol{A}_0(\boldsymbol{r}) e^{-i\omega t} \langle\, \psi_f \mid \boldsymbol{r} \mid \psi_i \,\rangle\,,
\end{aligned} \tag{2.12}$$

which expresses M_{if} with the explicit dipole operator. Thus using eq. (2.12) in eq. (2.7) gives

$$W_{if} \propto A_0^2\, \omega_{if} |\langle\, \psi_f \mid \boldsymbol{\epsilon} \cdot \mathbf{r} \mid \psi_i \,\rangle|^2 \propto I\,, \tag{2.13}$$

with I being the intensity of the electromagnetic wave. To explicitly express the polarization direction that is parallel to the vector field the unity vector $\boldsymbol{\epsilon}$ is introduced: $\boldsymbol{A} = A_0\boldsymbol{\epsilon}$

Dipole selection rules A symmetry consideration reveals one aspect of the transition matrix element: Instead of using the Dirac notation, the matrix transition element can be written as

$$M_{if} \propto \int_{-\infty}^{\infty} d^3x\, \psi_i^*(\boldsymbol{r})\, \mathbf{r}\, \psi_f(\boldsymbol{r}). \tag{2.14}$$

In order to have a non zero value, the integral must have an integrand that has even inversion symmetry about the point of origin $\boldsymbol{r} = 0$. Thus with $\boldsymbol{r}$ being an antisymmetric function, the product of ψ_i and ψ_f must be antisymmetric, too [22]. Hence the parity of initial and final state must be different. The parities p of the wave functions are defined by the l-quantum number in their spherical harmonic part $Y_{l,m}$ and $p = (-1)^l$. In combination with angular momentum conservation in a photon absorption process (the quantum number of the angular momentum of linearly polarized photons is $l = \pm 1$), this leads to the following transition selection rules in the dipole approximation for electronic wave functions:

$$l_f = l_i \pm 1 \tag{2.15}$$

Also for Δm selection rules can be found. Assuming linearly polarized light in z-direction the matrix element in polar coordinates reads

$$M_{if} \propto \int_{-\infty}^{\infty} d^3r\, \psi_i^*(r,\theta,\phi)\, r\cos(\theta)\, \psi_f(r,\theta,\phi) \tag{2.16}$$

$$\propto \int_0^{2\pi} d\phi\, e^{i(m_f - m_i)\phi} \int_{-\infty}^{\infty}\int_0^{\pi} dr\, d\theta\, r^2 \sin\theta\, \psi_i^*(r,\theta)\, r\cos(\theta)\, \psi_f(r,\theta)\,. \tag{2.17}$$

$$\tag{2.18}$$

The first integral in eq. (2.18) is only non zero if

$$\Delta m_l = m_f - m_i = 0\,. \tag{2.19}$$

For circular polarized light it can be shown in a similar way that

$$\Delta m_c = \pm 1\,. \tag{2.20}$$

2.2 Photoelectron Diffraction

Photoelectron diffraction is a powerful tool to resolve the structure of surfaces with sub-Ångstrom resolution. Briefly, by absorption of photons with energies ranging from the ultraviolet (UPD) to the x-ray (XPD) regime, photoelectrons are emitted. These electrons scatter coherently at neighboring atoms and create an interference pattern with the unscattered direct electron wave [23, 24]. Thus by scanning the photoelectron intensity distribution $I(\theta,\phi)$ over the whole hemisphere above a single-crystalline sample, a diffraction pattern can be recorded that carries information

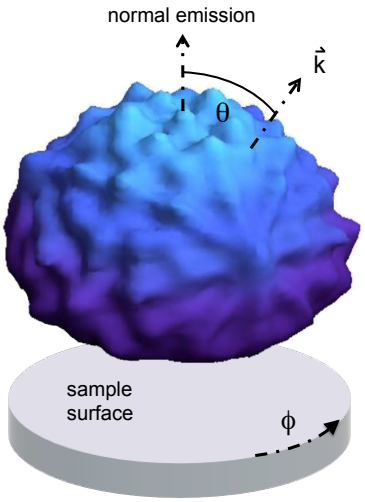

Figure 2.2: Photoelectron intensity distribution of Bi 4f emission, excited with photons of energy $h\nu = 1253.6$ eV, plotted on the surface of the hemisphere that is scanned with the detector. Large elevations from the spherical surface correspond to high intensities at the respective spherical angles. Normal emission and an exemplary emission direction $\bar{k}$ corresponding to the polar angle θ is indicated. ϕ shows the azimuthal rotation sense.

about the structure around the emitter atoms. By selecting specific electron energies corresponding to particular core levels one can choose the emitter by its chemical nature. Hence the method is particularly interesting for investigating crystal structures, bonding geometries of atoms or molecules adsorbed on surfaces and the local environment of impurity or dopant atoms inside surfaces [11, 12, 25]. On the angular map created through such a measurement various maxima and minima occur as demonstrated in the 3D representation in Fig. 2.2. An extensive introduction to the method is given in [24].

2.2.1 Single Scattering Theory

A theory to understand and quantitatively predict photoelectron diffraction patterns is the single scattering theory that will be outlined here. This formalism is used to calculate the angle dependent photoelectron intensity I. The theory was developed for emission from core levels rather than for lightly bound valence states, so first only core levels will be considered.
In principle the scattering problem is solved by calculating the intensity with Fermi's golden rule, which implies solving the transition matrix element:

$$I \propto |\langle\, \psi_f(\mathbf{r}, \mathbf{k}_f) \mid \boldsymbol{\epsilon}\, \mathbf{r} \mid \psi_{i,nlm}(\mathbf{r})\, \rangle|^2 \,, \tag{2.21}$$

with $|\psi_{i,nlm}(\mathbf{r})\rangle$ as bound initial state and $|\psi_f(\mathbf{r})\rangle$ as unbound time-reversed LEED final state

$$|\psi_f(\mathbf{r})\rangle = \phi_0(\boldsymbol{r}, \boldsymbol{k}_f) + \sum_j \phi_{l_f,j}(\boldsymbol{r}, \boldsymbol{k_f}) \,. \tag{2.22}$$

This final state consists of a plane wave and the sum over spherical waves incoming at each scatterer site j [26].

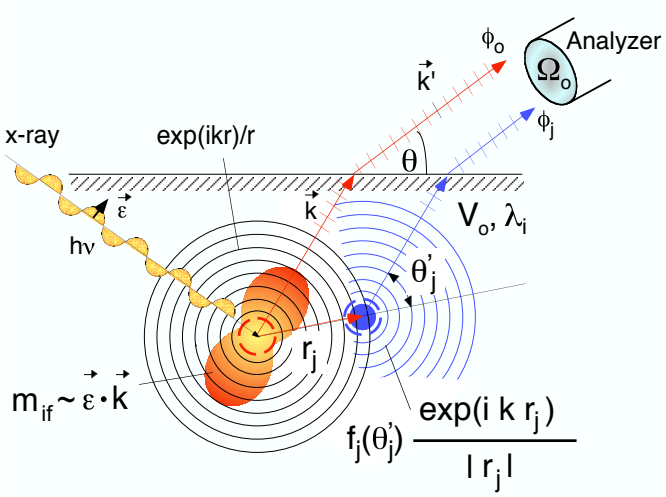

Figure 2.3: Illustration of spherical wave electron scattering. An electron is emitted by a x-ray photon and propagates through the crystal as spherical wave as indicated by the black circles. The wave being modulated by the scalar product $m_{if} \propto \boldsymbol{\epsilon} \cdot \boldsymbol{k}$ comes in at the blue scatterer, where it is transformed to the scattered wave with amplitude $f_j(\theta'_j) e^{i\, k_f r_j}/r_j$. The red and blue lines indicate the paths of the unscattered and scattered electron respectively. Both are refracted by the surface potential step V_0 and then detected in the analyzer.

Following the *three step model*, the electronic excitation is considered first: Due to the dipole transition rules, the emitted electron wave function, also called source wave, can have two different l-quantum numbers $|\, l_i \pm 1, m \,\rangle$. Since core levels are completely filled shells, they are isotropic and one can assume that the light polarization is parallel to the z-axis of the wave functions, thus the transition selection rule is $\Delta m = 0$. As all l-orbitals are fully occupied in a core state, the outgoing source waves will have quantum numbers $m = -l_f, -l_f + 1, \ldots\ , l_f - 1, l_f$.
The outgoing l-waves will have different amplitudes proportional to the radial transition matrix element $R_{l_i \pm 1}$. R is proportional to the overlap integral between the radial part of $|\, \psi_i \,\rangle$ and $|\, \psi_f \,\rangle$. Each of the l-waves also has a phase $\delta_{l_i \pm 1}$ that can be retrieved from the argument of the transition matrix element. Amplitudes and phases are tabulated for various emission energies and initial states [27].
Summarizing the matrix element of each source wave with quantum numbers l and m can be described as [24, 28]

$$m_{if}(\boldsymbol{k}_f) = C R_{l_f} e^{i\delta_{l_f}} Y_{l_f,m}(\boldsymbol{k}_f)\,, \tag{2.23}$$

where C is a Gaunt coefficient. One can see the proportionality $m_{if}(\boldsymbol{k}_f) \propto Y_{l_f,m}(\boldsymbol{k}_f)$. As a consequence scatterer atoms will experience different wave amplitudes depending to their relative position with respect to the light polarization.
The second step follows the propagation of the waves through the solid. Each wave is expressed as the coherent sum of the direct wave emitted from a localized core level and all singly scattered waves from all atoms surrounding the photoemitter. On their way to the detector the direct and scattered waves have different pathways but a fixed phase relation, since elastic scattering is a coherent process (Fig. 2.3). The single scattering expression gives the photoelectron intensity

distribution in k-space [28, 29]:

$$I(\mathbf{k}_f) \propto \sum_{m=-l_i}^{m=l_i} \Big| \sum_{l_f=l_i-1, l\neq l_i}^{l_i+1} \Big(m_{if}(\mathbf{k}_f) e^{-L_0/2\lambda_i} + \sum_j m_{if}(\boldsymbol{k_{r_j}}) e^{-L_j/2\lambda_i} \times \frac{f_j(\theta'_j)}{r_j} e^{i\, k_f r_j (1-cos\theta'_j)} \cdot W_j \Big) \Big|^2 + TDS\,. \tag{2.24}$$

The waves are exponentially damped on their specific path ways L_0 and L_j with λ_i, the inelastic mean free path, as a damping constant. $f_j(\theta'_j)$ is the complex atomic scattering factor (containing also the scattering phase shifts) depending on the scattering angle θ'_j of the j-th scatterer and $\mathbf{r}_j$ is the vector to the j-th scatterer. The index j runs over all atoms in the solid, excluding the photoemitter. $e^{i\, k_f r_j (1-\cos\theta'_j)}$ displays the geometric phase shift between direct and scattered wave. The Debye-Waller factor W_j and TDS (thermal diffuse scattering term) both describe effects due to thermal disorder [30, 31]. The summations over m and l add up the waves emitted with different quantum numbers. Equal m-quantum numbers are coherently summed.
Finally the third step treats the refraction at the surface potential step V_0 using Snell's law for surface refraction as given in eq. (2.2) and the waves are detected under the refracted emission angle outside the crystal θ.
All these steps are implemented in a single scattering cluster (SSC) program [28], that calculates the above expressions for a finite cluster size of typically a few hundred atoms. The program was used a lot during this dissertation and will play a role in many of the chapters.

2.2.2 Electron scattering at Coulomb potentials

A fundamental process in photoelectron diffraction is the electron scattering at atoms inside the solid. The potential landscape at which the electrons scatter can be approximated by the augmented plane wave method as first proposed by Slater [32]. This method assumes spherical potential wells around the atom sites in the crystal. In the interstitial space between the spheres the potential is constant with value E_0, the inner potential. If this value is referenced to the vacuum energy E_{vac}, it will be called V_0 in this work. The approximation is also often called muffin-tin approximation [33] as the 3-dimensional plot of the potential in the xy-plane looks like a muffin tin. Fig. 2.4 shows the radial dependence of the potential $V(r)$. To determine how an electron scatters at such a potential well inside the crystal the complex scattering amplitude $f(\theta)$ is calculated. This can be done by a partial wave expansion, that expands the incoming wave into waves with discrete angular momenta and each partial wave experiences a phase shift at the potential. In this work phase shifts of all l-partial waves were generated using a muffin-tin code [33, 34]. Assuming that incoming waves are plane waves (plane wave approximation) the rules to sum the contribution of all partial waves and their phase shifts up to get $f(\theta)$ are relatively simple [35]:

$$f(\theta) = \frac{1}{k} \sum_{l=0}^{\infty} (2l+1) e^{i\,\delta_l} \sin\delta_l\, P_l(\cos\theta) = |f(\theta)|\, e^{i\phi(\theta)} \tag{2.25}$$

k is the absolute value of the wave vector, $|f(\theta)|$ is the absolute value of the angle dependent scattering amplitude, $\phi(\theta)$ is the phase shift of the outgoing electron wave and $P_l(\cos\theta)$ is the angular dependent Legendre polynom. In the single scattering cluster program $f(\theta)$ is calculated in the more complicated but more precise spherical wave approximation following the Rehr-Albers

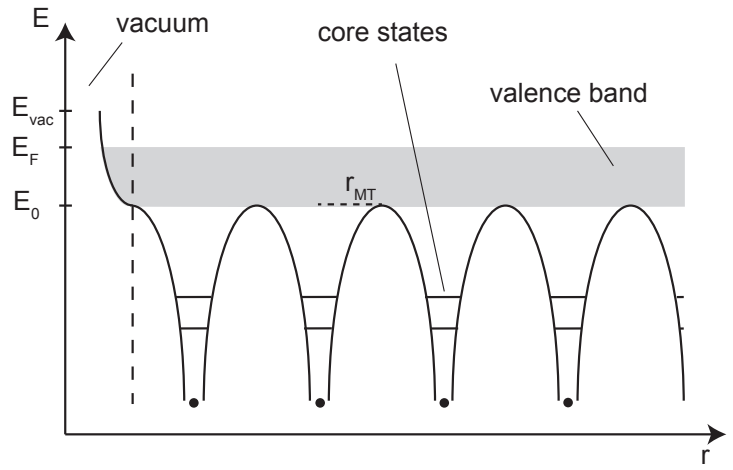

Figure 2.4: Muffin-tin potential $V(r)$. The wells are located around the atomic cores, the interstitial region has energy E_0, *i. e.* the bottom of the valence band. The muffin-tin radius r_{MT} is defined as the distance from the core to the boundary where the spheres touch. The gray shaded area shows the valence band reaching from E_0 up to E_F. The inner potential is defined as $V_0 = E_{vac} - E_0$. At the left border (dashed line) the crystal ends and the potential rises up to the vacuum level E_{vac}.

formalism [28, 29, 36–38].

2.2.3 Differences of XPD and UPD

As already mentioned the single scattering theory was developed mainly for core initial states, which are usually strongly bound so the typical wave length to access those states are in the x-ray regime. Diffraction patterns recorded with these light sources and kinetic energies above $E_{kin} = 100$ eV are called x-ray photoelectron diffraction (XPD) patterns. On the contrary lightly bound states like shallow core levels or valence states are better accessible with UV-light, due to a larger interaction cross section. Diffraction measurements with electron energies $E_{kin} < 50$ eV will be referred to as UV-light photoelectron diffraction (UPD). The physics in these two regimes also differs in several aspects [23, 28]. First, the scattering amplitudes and phase shifts of electrons that scatter off a potential in XPD and UPD are distinct as illustrated in Fig. 2.5. The curves for high electron energies show large amplitudes only in the forward scattering direction (Fig. 2.5 (a)), *i. e.* at $\theta \approx 0°$. Therefore the angular positions of the scatterers with respect to the emitter are directly imprinted in the diffraction map. Also the phase shifts (calculated in the plane wave approximation for simplicity reasons) for this region are small (Fig. 2.5 (b)) so that direct and scattered wave show constructive interference. Thus the quality of simulations and the understanding of XPD experiments is very good. It becomes more complicated in the case of electrons with lower energies. There the scattering amplitudes at larger angles are considerable, especially the amplitude for backscattered electrons. So single scatterers will contribute to intensities at various regions in the diffraction map. Additionally there will be various regions of constructive and destructive interference, due to changes in the sign of the phase. This leads to far less intuitive

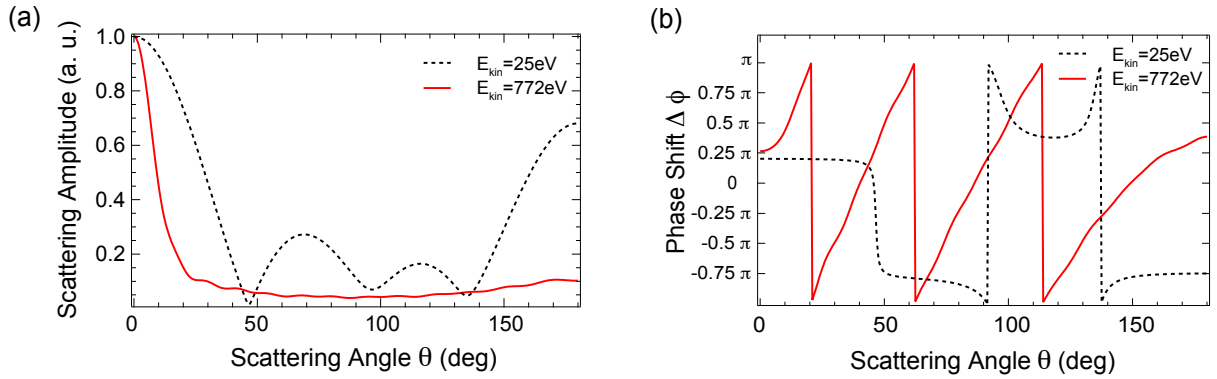

Figure 2.5: Scattering characteristics of electrons in silver calculated in the plane wave approximation. (a) shows $|f(\theta)|$ for $E_{kin} = 772$ eV (red) and $E_{kin} = 25$ eV (dashed black). In (b) phase shifts corresponding to the scattering amplitudes in (a) are presented.

diffraction maps in case of UPD. Even more important is the reliability of simulations. However with more contributions from different angles, smaller amplitudes and stronger interference effects UPD simulations suffer more from inaccuracies of input values. Additionally multiple scattering will play a more important role than in XPD.
On the other hand the sensitivity of UPD simulations to input parameters also reflects the sensitivity of UPD experiments to tiny structural parameters of the sample system for example. This renders UPD a method with great potential for resolving minute structural changes on a sub-Ångstrom scale.

2.2.4 Non isotropic initial states close to E_F

Further complications with UPD analysis occur, if initial states are molecular orbitals or valence states. In the case of core level emission where the atomic orbitals with the same l-quantum number are completely filled with electrons, the spatial distribution of the initial state is isotropic. The angular dependence of the emitted amplitude is modulated by the scalar product $\boldsymbol{\epsilon}\,\boldsymbol{r}$ and the mathematical description of photoemission is comparably uncomplicated for a system invariant to rotations. Also the description of the outgoing $l_i \pm 1$ waves is clear. Furthermore atomic core states are per definition located around the cores inside the solid and thus spatially well confined states. Therefore their emission and propagation through the solid is simple to describe.
Molecular orbitals and valence states, however are linear combinations of different l- and m-quantum states (like sp-bands or sp_2-hybridized orbitals for example). So first, the treatment of angular momenta l_f of the outgoing electrons will be more complicated. In case of sp_2-hybridization the summation for outgoing waves will cover quantum numbers $l_f = 0, 1$ and 2 and their respective m-quantum numbers. Second, these states are non isotropic, which leads to a more complicated calculation of the matrix element and third, valence states and often also molecular states are not localized at a single ion core but rather spread out in space. Hence it is impossible to define a localized position for the emitter as it is needed in SSC theory. In some cases however assumptions can be made that partly overcome the named problems, so that SSC calculations still give reasonable results.

1. If a molecular orbital has sufficiently localized character, the emission from its different contributing orbitals can be calculated taking their orientation into account. In the framework of this work such calculations were done for single p-orbitals p_x, p_y or p_z. In chapter 5 the HOMO-1 molecular orbital of tin-phthalocyanide will be approximated by a single p_z orbital. The quantum mechanical considerations are outlined here.
For the calculation of matrix elements it is most convenient to have the polarization direction parallel to the quantization axis z, because then only one component of the dipole operator has to be evaluated. Hence one defines the polarization axis of the incoming light as z-axis of the quantum coordinate system. However, in order to record a full diffraction map in the experiment, the sample is rotated at each angular step and with it the p_z-orbitals spatial orientation of the adsorbed molecules. Thus the rotating p_z-orbital has to be expressed in the quantization coordinate system at each step [39, 40]. (Note: This is not needed for isotropic core states since the z-axis of the wave function can always be assumed to be parallel to $\boldsymbol{\epsilon}$, due to rotational invariance.) The rotation of one coordinate system into another is described by Euler's rotation matrices. It can be shown that the relation

$$R(\alpha, \beta, \gamma) = R_z(\alpha) R_y(\beta) R_z(\gamma) \tag{2.26}$$

describes a rotation around all three Euler angles α, β and γ by the non-commutative application of 3 rotation matrices R_i [41]. The axes i are space-fixed axes in this case. In quantum mechanics the generators of rotations are angular momenta, so the rotation of functions in Hilbert space $\mathcal{H}$ is given by

$$\mathcal{D}(\alpha, \beta, \gamma) = e^{-\frac{i}{\hbar} J_z \alpha}\, e^{-\frac{i}{\hbar} J_y \beta}\, e^{-\frac{i}{\hbar} J_z \gamma}\,, \tag{2.27}$$

with $\phi = \alpha$, $\theta = \beta$ and $\phi' = \gamma$. Rotations of ϕ around the quantized $z-$axis are trivial and only lead to a new quantum number m'. Only the rotation around the y-axis is not trivial because there is no quantum number attributed to it and thus it mixes different m. The application of $\mathcal{D}$ on a wave function $Y_{l,m}(\theta, \phi) = |\, l, m \,\rangle$ is nothing but a change of basis system:

$$\mathcal{D}\,|l, m> = e^{-\frac{i}{\hbar} m' \phi} \sum_{m'} |l, m'>< l, m'| e^{-\frac{i}{\hbar} L_y \beta} |l, m>\,, \tag{2.28}$$

here J=L and j=l is used. So one needs to find the matrix representation of
$d^{(1)}_{m',m} =< l, m'| e^{-\frac{i}{\hbar} L_y \beta} |l, m >$. In the case of p_z-orbitals $l = 1$ and after some transformations using the definition of L_+ and L_- one finds [41]

$$d^{(1)}_{m',m}(\beta) = \left(\begin{array}{c|ccc} l = 1 & m = -1 & m = 0 & m = 1 \\ \hline m' = -1 & \frac{1}{2}(1 + cos\beta) & -\frac{1}{\sqrt{2}} sin\beta & \frac{1}{2}(1 - cos\beta) \\ m' = 0 & \frac{1}{\sqrt{2}} sin\beta & cos\beta & -\frac{1}{\sqrt{2}} sin\beta \\ m' = 1 & \frac{1}{2}(1 - cos\beta) & \frac{1}{\sqrt{2}} sin\beta & \frac{1}{2}(1 + cos\beta) \end{array} \right). \tag{2.29}$$

In other words $d^{(1)}_{m',m}(\beta)$ gives a list of coefficients that are used to represent any p-orbital from one coordinate system in another system rotated by β. Such a transformation was implemented in the existing SSC code and used in chapter 5. Further details will be mentioned there.
2. Another assumption that proved to yield good results for Cu valence states is that the emitted electrons can be assumed to come from a localized emitter, if the whole energy band is integrated [23]. In reality the states in the Cu valence band are delocalized of course. However it is argued that all eigenstates in the energy band can be expanded over localized orbitals with the same l-quantum number by the use of one energy independent radial wave function [26]. This assumption will become important in chapter 6.

2.3 Time-resolved Photoelectron Diffraction

After the strength of photoelectron diffraction was mentioned above, the idea to realize a time-resolved XPD or UPD measurement is very intriguing. Since the natural time scale of nuclear motion is the femtosecond scale, the combination of sub-Ångstrom resolved structures and femtosecond time resolution is predestined to follow nuclear motion in real time.
For time-resolved UPD in principle the same quantities as in time-resolved angle-resolved photoelectron spectroscopy (ARPES) are measured. Both experiments are conducted within a pump-probe setup. However in order to integrate whole valence bands, with typical work functions of $\phi = 4 - 5$ eV larger photon energies than the often used 6 eV for ARPES are needed. So only with pulsed XUV light from higher harmonics generation (HHG) [42] or pulsed x-rays [7, 43, 44], it is possible to conduct time-resolved XPD or UPD experiments.
Time-resolved photoelectron diffraction is complementary to time-resolved ARPES measurements, because instead of electronic states the lattice structure is probed. In the course of this work a time-resolved UPD experiment was conducted using pulsed XUV light from HHG (chapter 6). The light pulses were provided by the Attoline built by the Ultrafast Laser Physics group of U. Keller at ETH Zurich [45] (see chapter 3.2). In the experiment a Bismuth(111) crystal was excited with an intense femtosecond IR pulse and parts of the time dependent photoelectron diffraction signal from the excited crystal were recorded with pulsed photons of mainly the energies of $h\nu = 20.4$ eV and 23.5 eV.
A time-resolved XPD was simulated for the system of carbon monoxide on a Pt(111) surface. In the simulations the CO molecules were excited by pulsed THz-radiation and probed with pulsed x-rays (chapter 7).

2.3.1 Time-resolved ARPES

Time- and angle-resolved photoelectron spectroscopy are realized in a pump-probe experiment. Thereby a short laser pulse (usually IR) excites the system into a transient non-equilibrium state by "pumping" energy into the system under investigation. With a variable delay Δt a UV pulse probes the system in the non equilibrium state at chosen times.
Figure 2.6 illustrates the time evolution of a pump-probe experiment. Through the IR field at time delay $\Delta t = 0$ charge carriers are promoted to higher energies by creation of electron-hole pairs. These states relax on a femto- to pico-second time scale by inelastic scattering processes like electron-electron scattering or scattering with the lattice (electron-phonon coupling). After delay Δt the transient non equilibrium electronic states are probed via UV photoelectron spectroscopy. Through gradual changes of the delay Δt and measurement of the angular and energy distribution of the electronic states at each time step, a 4-dimensional parameter space is sampled. The measured quantity is the spectral function $A(E, k_x, k_y, \Delta t)$.
Thus with time-resolved ARPES electronic phase transitions induced by intense infrared fields can be measured. The method will be applied in chapter 6 to measure the response of Bi(111) to intense IR fields. Moreover lifetimes of transient electronic states can be probed. The right hand side of Fig. 2.6 shows how a system is thermalized first by exciting electrons to energetically higher states followed by a heating of the system, when the electrons relax.
The mentioned relaxation processes are briefly listed here:

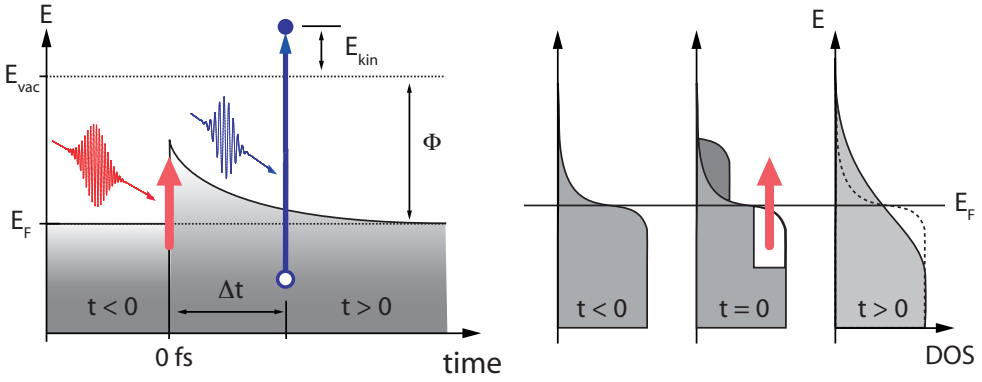

Figure 2.6: Pump-probe experiment. *Left:* At delay $\Delta t = 0$ electron-hole pairs are created promoting electrons to higher energies. These relax with a certain lifetime. After Δt the electronic structure is probed with pulsed UV photons. *Right:* Thermalization of the system. For $t < 0$ the system is at a temperature T_i. Electrons from below E_F are promoted above E_F at t=0, they relax for $t > 0$ via inelastic scattering processes and heat the system to $T_f > T_i$, as can be seen by the new shape of the Fermi edge. The figure was taken from [19]

Electron-electron scattering This is the most important process to establish an equilibrium energy distribution among the electrons around the Fermi edge in the first 100 fs after excitation with the IR pulse [46]. In the Landau theory of Fermi liquids it is described that a hot electron with wave vector $\boldsymbol{k}_1$ can inelastically scatter with a cold electron with $\boldsymbol{k}_2$, thereby exchanging energy and momentum $\boldsymbol{q} = \boldsymbol{k_1'} - \boldsymbol{k_1}$ creating two quasi particles $\mathbf{k_1'}$ and $\mathbf{k_2'}$. The scattering rate is given by [19, 47]

$$\Gamma_{ee}(k_1, \sigma_1) = 2\pi \sum_{k_2,q} \sum_{\sigma_2} W^2(\boldsymbol{q})\, n_{k_2,\sigma_2}(1 - n_{k_2',\sigma_2})(1 - n_{k_1',\sigma_1}) \cdot \delta(\boldsymbol{k}_{1,\sigma_1} - \boldsymbol{k'}_{1,\sigma_1} + \boldsymbol{k}_{2,\sigma_2} - \boldsymbol{k'}_{2,\sigma_2})\,. \tag{2.30}$$

The δ-function ensures energy conservation, n is the occupation number and $W^2(\boldsymbol{q})$ is the quadratic Coulomb interaction depending on momentum exchange. It can be found that lifetimes in the vicinity of the Fermi edge are strongly increased compared to those further away from E_F. This leads to a redistribution of energy and drives the electronic system to equilibrium [19, 47].

Electron phonon scattering Electron-phonon scattering becomes the dominant relaxation process on the order of hundreds of femtoseconds up to a few picoseconds. To express the strength of electron-phonon coupling one can introduce the mass enhancement factor λ. It adds to the effective mass of electrons $m^* = m_0(1+\lambda)$ causing a flattening of the band dispersion in the range of $E_F \pm \hbar\omega_D$. m^* and m_0 are the electron effective masses with and without electron-phonon coupling respectively. ω_D is the Debye frequency. The mass enhancement factor itself can be approximated to [48]

$$\lambda = 2 \int_0^{\omega_{\max}} d\omega\, \frac{\alpha^2 F(\omega)}{\omega} \tag{2.31}$$

$\alpha^2 F(\omega)$ is the Eliashberg function and can be interpreted as a squared matrix element α^2 multiplied with the phonon density of states (DOS) $F(\omega)$. In a quasi elastic approximation the function can

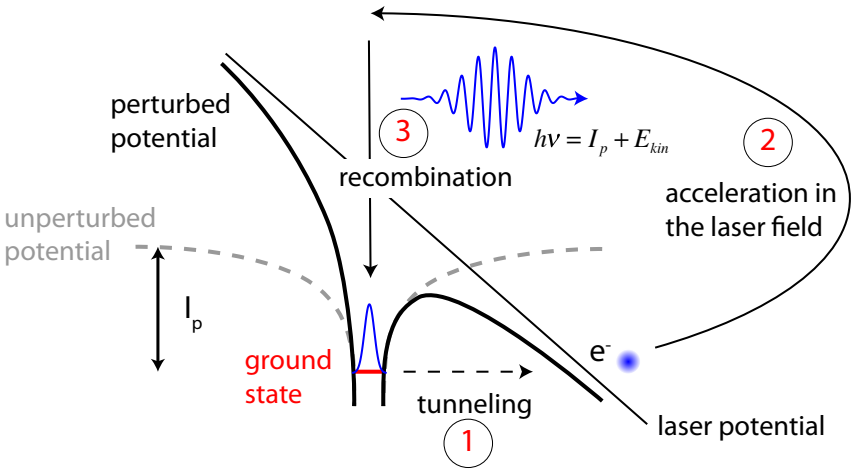

Figure 2.7: Higher harmonics generation process in a three steps model: The tunneling process through the perturbed ion potential is indicated by the number 1. The tunnelled electron is accelerated at number 2 and recombines at number three by emission of a higher harmonic photon. Figure taken from citeLocher:2013

be written as

$$\alpha^2 F(\omega) = \sum_{\boldsymbol{q},\nu,f} |g_{i,f}^{\boldsymbol{q},\nu}|^2 \, \delta(\omega - \omega_{\boldsymbol{q},\nu}) \delta(E_{k_i} - E_{k_f})) \tag{2.32}$$

This describes the sum over all probabilities to scatter electrons that transfer the energy $E_{k_f} - E_{k_i}$ and the momentum $\boldsymbol{q} = \boldsymbol{k}_f - \boldsymbol{k}_i$ to a phonon [49].

2.3.2 Electron diffraction with non monochromatic XUV pulses from HHG

Pulsed XUV photons from HHG were used as probe for time-dependent UPD measurements. To trigger a HHG process an intense laser field with pulse durations of a few femtoseconds is focussed onto a gas target [13]. In a semiclassical model the HHG process itself is described in three steps [14]:

1. The intense laser field bends the core potential of a gas atom, which enables electrons to tunnel through the potential barrier.
2. Initially, the tunneled electron is classically accelerated away from the ion due to the IR field. When the polarization of the IR vector potential changes, it is redirected to the ion. On its way the electron absorbs multiple IR photons.
3. Electron and ion recombine by emission of a photon with multiple IR energy.

The process is illustrated by Fig. 2.7. At every half cycle of the IR vector potential bursts of higher harmonics will be emitted. Thus the emission bursts happen with a frequency of twice the driving field frequency. Applying Fourier theorems and symmetry considerations one finds that only odd-order harmonics can be found [50].
In order to make the process efficient also the light polarization has to be considered: From a

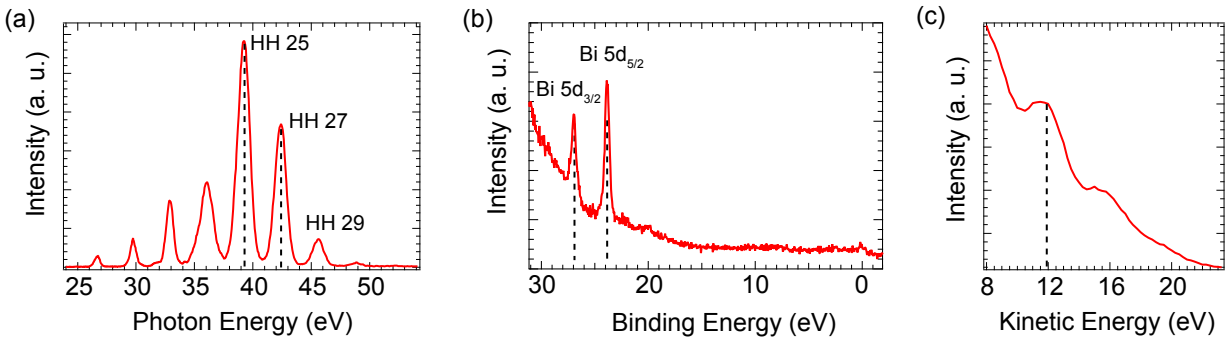

Figure 2.8: (a) Photon spectrum of higher Harmonics generated in an Ar-gas jet is shown. The fundamental IR wavelength is 793 nm. Higher harmonics 25, 27 and 29 are indicated. The pulse duration is $\Delta t \approx 8$ fs. (b) Energy spectrum of shallow core levels Bi $5d_{3/2}$ and $5d_{5/2}$ excited with He II$_\alpha$. (c) A region from a photoemission spectrum from a Bi(111) crystal generated with the photon spectrum in (a) is shown. The peak indicated by the dashed line stems from emission of both Bi $5d_{3/2}$ and $5d_{5/2}$ core levels, the first of which is emitted by harmonic 27 and the second by harmonic 25.

quantum mechanical point of view, recombination becomes most probable, if the electron returns as close as possible to its parent ion to have a large overlap integral with the remaining part of the wave packet inside the ion. Thus the highest efficiency is given by linearly polarized light, where the electron only moves along one dimension. Using circularly polarized light makes a return of the electron to its starting point impossible [14].

An exemplary energy spectrum showing harmonics of a 793 nm IR pulse generated in Ar gas at the Attoline is presented in Fig. 2.8 (a). In the course of this work The presence of multiple harmonics implies consequences on the photoemission spectrum from a crystal surface. Figure2.8 (b) shows a photoemission spectrum of the Bi(111) 5d core levels excited with the photon distribution as seen in (a). With $E_B = 23.8$ eV ($5d_{3/2}$) and $E_B = 26.9$ eV ($5d_{5/2}$) the spacing of the core levels is equal to that of two adjacent harmonics, so that electrons from both core levels will appear in one peak in the signal of Fig. 2.8. In this case harmonics 25 and 27 result in a peak at $E_{kin} = 11.8$ eV. The next pair of higher harmonics (27 and 29) should result in a peak shifted to 3.1 eV higher E_{kin}. Still it is obvious that the spacing between the two peaks in the surface spectrum is about $\Delta E = 4$ eV. This effect is due to space charge effects, *i. e.* the compressed intense IR pulse emits so many electrons in close vicinity to each other that they are repelled by their coulomb forces and thus the spectrum is spread [51]. Inserting the measured work function $\phi = 4.36$ eV, E_B of the respective electronic states and the energy position of the peak maximum $E_{kin} = 11.9$ eV in eq. (2.1) gives the values $h\nu_{25} = 40.16$ eV and $h\nu_{27} = 43.26$ eV respectively. So again due to space charge the spectrum is shifted and the values retrieved with eq. (2.1) are larger than the actual photon energies. The photons with $h\nu < 39$ eV also generate photoelectrons from the Bi crystal. This region is not shown in Fig. 2.8 (b) but from the strong increase at the left side of the curve it can be seen that these photons generate a large inelastic electron background. Additionally, compared to monochromatic light sources like the He I$_\alpha$-line from a discharge lamp or x-ray K$_\alpha$-lines, the single harmonics are broad what leads to another broadening effect of the photoemission spectrum.

Concluding the reader should bear in mind, that it is more difficult to disentangle effects induced by the light source and those from the electronic initial states of the crystal, when light sources

as shown here are used.
The laser pulses in this work have a repetition rate of 1 kHz, leading to low count rates compared to light sources with continous waveforms (cw). The recording of full photoelectron diffraction maps requires to scan the 2 π solid angle on top of the sample with sufficient point density. Therefore several thousand emission directions are scanned. With conventional channeltron analyzers this is a time consuming measurement even with cw light sources. Thus time-resolved UPD in this work is measured with a 2D wide angle lens analyzer with massive parallel detection capabilities. Even then only small parts of a full 2π electron diffraction maps can be recorded due to low count rates and time limited laser stability.

2.4 Photoemission with a 2D hemispherical electron analyzer

To measure angle-dependent photoelectron intensities, like in the above mentioned sections, either the sample or the analyzer have to be rotated, in case a conventional electron analyzer is used. One main improvement of modern commercial hemispherical analyzers is their capability to record a 2-dimensional picture of electrons with a large angular acceptance range. Usually one axis of the 2D picture is the dispersive axis, being a function of electron energy, while perpendicular to it there is an angular axis, where the emission angle is projected to. Thus a certain angular width can be detected without moving the sample (see Fig. 2.9). Obviously this class of analyzers has advantages for all kinds of angle resolved measurements. Still the features of such a detector imply physics one should be aware of.

In this context only theoretical considerations are made, exact details on the detector used in this work will be given in chapter 3.1.
The principle of a hemispherical analyzer is an energy filter realized by two hemispheres with different radii and different potentials as shown in Fig. 2.10. Assuming electrons with a continuous energy distribution enter the analyzer through the entrance slit S1 in the distance R_0 from the center of the hemispheres, the electric field between the two hemispheres will filter the electrons depending on their energy. The electric field provides a centripetal force

$$\mid \mathbf{F}_z \mid = \mid q\mathbf{E} \mid = q\frac{U}{\Delta R} = m\frac{v^2}{R_0} \tag{2.33}$$

so that only electrons with the right energy, called pass energy E_p, will follow the center trajectory. Electrons with higher energy will arrive closer to the outer hemisphere and the ones with smaller energy will be attracted to the inner hemisphere. That way a certain width of energy distribution can be measured at once.
In order to count electrons with a certain initial kinetic energy, by applying a potential ϕ to S1 with reference to the sample, their energy is adjusted to E_p when entering the hemispheres. The correct potential follows the relation:

$$\phi = \frac{1}{e}(E_{ini} - E_p), \tag{2.34}$$

with E_{ini} as the initial electron energy, E_p as the pass energy, *i. e.* the energy at which electrons follow an exact circle inside the hemispheres.
In the 3-dimensional setup of the detector the electric field has spherical symmetry. Thus a slit in the shape of an arc with radius R_0 would be projected to the exit plane S2 in arcs of concentric

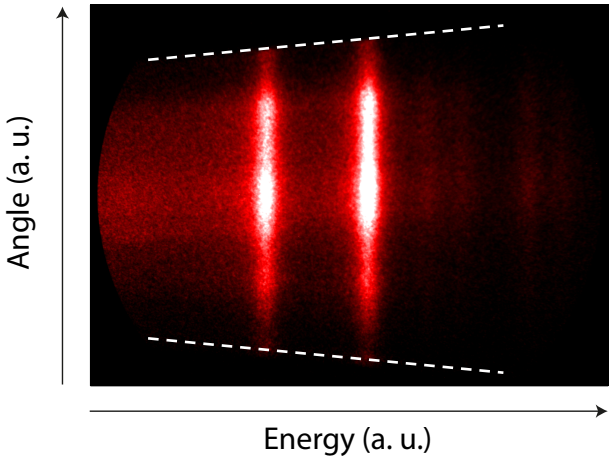

Figure 2.9: 2-dimensional picture recorded with a hemispherical detector. Bi $4f_{3/2}$ and $4f_{5/2}$ peaks were recorded. The energy distribution is displayed along the horizontal axis, the angular distribution along the vertical. The dashed white lines illustrate the trapezoidal shape of the signal.

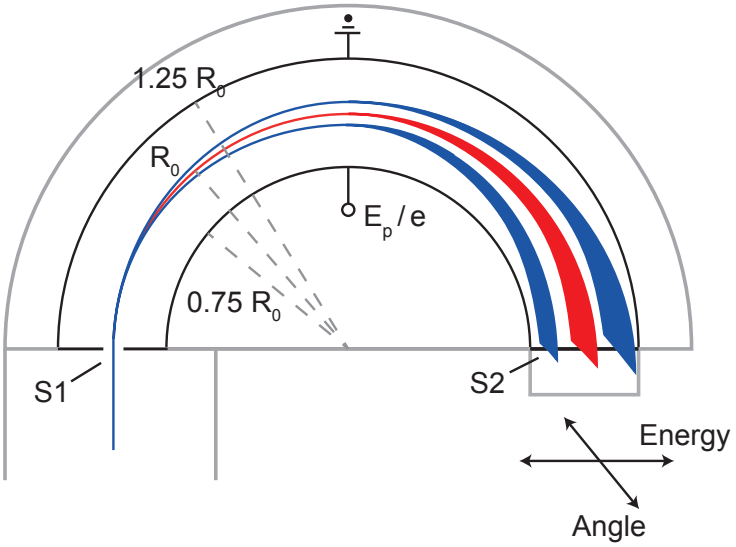

Figure 2.10: Sketch of electron trajectories inside the analyzer. S1 and S2 denote entrance slit and exit plane respectively. The red trajectory indicates electrons with E_p following an exact circle. The blue traces show slower and faster electrons that describe shorter and longer trajectories, respectively. The outer trajectories project longer lines on S2 than the inner ones. The ratio of outer and inner hemisphere radii corresponds to the geometry of the analyzer used in this work.

circles, with the radial position depending on the electron energy. In order to project a straight line on the detector along the angular axis, the radius of S1 is $\frac{R_0}{2}$. This leads to a trapezoidal picture in the exit plane S2, if the electrons have a finite energy distribution (see Fig. 2.10). If the analyzer is operated in the scanned energy mode, the trapezoidal shape of the 2D picture must be corrected for, otherwise electrons with the same emission direction and the same energy will be detected at alternating positions on the angular axis in the course of the scan. Usually the width of the slit S1 can be varied along the energy dispersive axis in order to increase the count rate. This leads to a loss in resolution as now electrons can enter the hemisphere that have a velocity vector with off-tangential direction and for them the projection shows aberrations.
Furthermore each 2D analyzer has a transmission function $T(E, \alpha)$ depending on the energy and the detector angle. α is linked to the angle of emission from the surface of course. While the energy transmission is comparably homogeneous, due to several lenses in front of the entrance slit S1, the projection efficiency is not homogenous along the angular axis and $\frac{\partial}{\partial\alpha}T(E, \alpha)$ is far from 0 in some regions. A more detailed study of $T(E, \alpha)$ and its corrections is done in chapter 4.
Another aspect of an energy scan with an electron analyzer is the intensity as a function of the different energy scanning modes. One can either choose a fixed retarding ratio $R = \frac{E_{kin}}{E_p}$ where the pass energy is changed with each energy step, or the fixed analyzer transmission, where $E_p = const.$ The overall intensity on the detector can be expressed as

$$I \propto \Delta E_A A_0 \frac{E_p}{E_{kin}} \propto \frac{E_p^2}{E_{kin}}. \tag{2.35}$$

ΔE_A is the energy width that is covered by the range of the exit plane S2 and A_0 is the acceptance area at S1. ΔE_A is proportional to to the pass energy as with higher pass energy the energy window accepted by S2 gets larger [52]. If one operates the analyzer in the "fixed retarding ratio" mode, $E_p = \frac{E_{kin}}{R}$ can be substituted in equation (2.35) and one sees that

$$I \propto E_{kin}. \tag{2.36}$$

In the case of fixed pass energy operation the following relation holds:

$$I \propto \frac{1}{E_{kin}}. \tag{2.37}$$

Thus depending on the operation mode of the analyzer the spectra can look very different.

Referencing the measured kinetic energy For solid state measurements most of the time it is relevant to know the electrons binding energy E_B with respect to the Fermi level E_F. The measured value however is the kinetic energy after the electrons entered the detector $E_{kin,A}$. So equation 2.1 must be written as follows:

$$E_{kin} = E_{kin,A} - \Phi_A = h\nu - E_B - \Phi_S. \tag{2.38}$$

It becomes obvious that the energy scale has to be calibrated with Φ_A in order to determine E_B.

3 Setup of a wide angle lens analyzer and its connection to the Attoline

3.1 Setup of WALküre chamber

One important part of this dissertation was the assembly of the WALküre apparatus as shown in Fig. 3.1 (a). It is built as a mobile unit that can be moved to different laboratories and light sources. To realize a compact setup the chambers are aligned vertically with the preparation chamber (PC) on top of the analysis chamber (AC).
The PC comprises various surface preparation and characterization units (see Figure 3.1 (b)): One is an argon sputter gun, for ion bombardment of the surface. At several flanges Knudsen-cell evaporators can be attached to cover the sample surface with adsorbates. The chamber is also linked to a gas tree via leak valves to dose different gases into the chamber. For the characterization of various vapors from the gas tree, the Knudsen-cells or from the sample itself, a quadrupole mass spectrometer (QMS) is mounted to the chamber. As means for surface characterization an OCI Low Energy Electron Diffraction (LEED) unit with possibility for auger electron spectroscopy exists. A hand valve connects a small entry lock chamber with a linear transfer to the PC in order to move new samples into the PC. The samples can then be lifted up from the linear transfer with a wobble stick.
Located on top of the PC is a modified VG Scienta Omniax manipulator. In order to move the sample along the z-axis from PC to AC the manipulator is vertically aligned. The manipulator has a transfer range of 400 mm in z-direction of 50 mm along the x- and y-axis each. Furthermore it is equipped with a home build goniometer and a gear drive so that samples can be rotated by 360° around the vertical axis, i. e. changing the polar angle of the manipulator θ_{Man}. Furthermore an arbitrary number of rotations around the sample normal, i. e. along the azimuthal angle ϕ is possible[53]. The rotations around the two axes are fully automated via two computer-controlled motors from Nanotec. The motors are equipped with an optical encoder and a feedback loop so that the reproducibility of the sample orientation is better than 0.5°. A planetary reduction gear (9:1) ensures a good force transfer from the motors to the goniometer gear. The optical encoder of the motors is able to find a zero position of the motor after each full rotation. That way it is in principle possible to give an absolute angular position of the sample. However due to the reduction drive the motor performs a full rotation, while the sample only rotates by a ninth of 360°. Thus every 40° a zero position can be found. In the present state of the apparatus a specific zero position of the θ_{Man} rotation is reached when the sample normal is parallel to the detector axis.
By means of a cryostat inside the manipulator and a cooling finger connecting the cryostat and the sample holder, the sample can be cooled down below 100 K. Via electric connections the sample can also be heated resistively. At values above 623 K the temperature can be measured with a

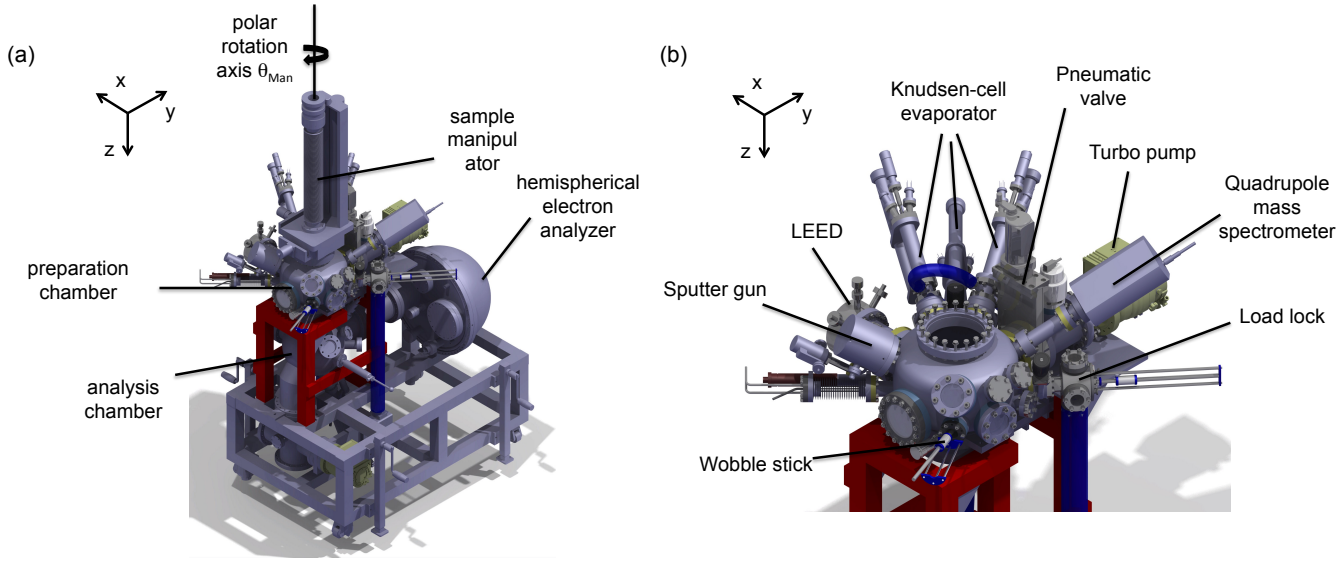

Figure 3.1: (a) The complete WALküre mobile unit. Manipulator and the two main chambers are aligned vertically. (b) Preparation chamber and the various attachments. The coordinate system in the upper left defines the translation axes of the sample.

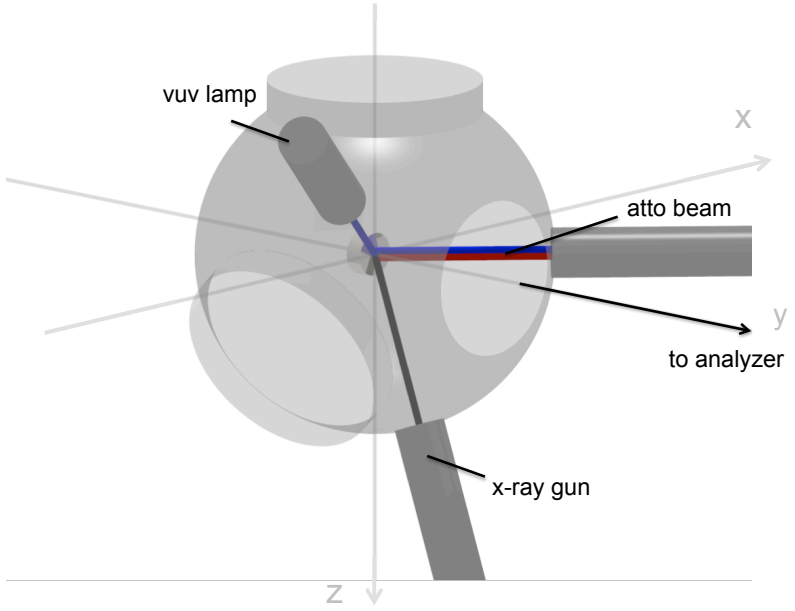

Figure 3.2: Geometry of the analysis chamber and the different light sources. The coordinates x, y and z define the translation axes of the sample

two color pyrometer (Maurer).
For photoelectron spectroscopy measurements the sample is lowered into the AC. Figure 3.2 shows the geometry of the AC and the different light sources in the present state of the WALküre at the Attoline at ETH Hönggerberg. The various sources are the following:

- Twin anode XR3E2 x-ray source from Thermo VG Scientific pointing into the y-z-plane and comprising two anodes:
  Si $K_\alpha - h\nu = 1739.4$ eV
  Mg $K_\alpha - h\nu = 1253.4$ eV
- Helium discharge lamp HIS 13 from OMICRON containing all different helium emission lines. With proper settings of pressure and discharge current the two lines can be enhanced or suppressed respectively [54]:
  He $I_\alpha - h\nu = 21.2$ eV
  He $II_\alpha - h\nu = 40.8$ eV
  (The HIS 13 can be operated with various gases and thus also emit photons of different energy.)
- Pulsed extreme ultra violet (XUV) light through higher harmonic generation (HHG) and pulsed infrared (IR) light
  XUV $- \Delta h\nu \approx 16 - 70$ eV
  IR $- h\nu \approx 1.5$ eV.

The core part of the machine is a hemispherical electron analyzer SPECS PHOIBOS 150 WAL. It is equipped with a wide-angle lens offering an acceptance angle of $\alpha = \pm 30°$. As imprinted in the model name trajectories for electrons with the pass energy are a half circle with radius $R_0 = 150$ mm. The analyzer records a 2-dimensional picture on which the photoelectron intensity is projected. While the electrons as function of emission angle from the surface are projected along the vertical axis, the horizontal axis is the energy dispersive axis, where the intensity as a function of energy is recorded. Figure 3.3 shows the scanning geometry of the analyzer and a recorded 2D picture. To record the electron intensity the detector consists of two micro channel plates (MCP) that enhance the electron signal by a factor of $10^7 - 10^8$. After the MCP the multiplied electrons are accelerated onto a phosphor screen and the picture of the screen is recorded by a CCD camera (1392 x 1024 pixels). The ultimate angle and energy resolution of the detector were measured to be 0.5° and 5 meV. The resolution depends on the entrance slit to the hemisphere and on the pass energy (see chapter 2.4). One can select entrance slits with different widths along the energy dispersive axis or apertures with different diameters [52]. The width of the energy range that is projected on the detector is 12 % of the electron pass energy. Due to the WAL and the 2D detector, many different emission angles and an extended energy range can be recorded simultaneously what leads to shorter acquisition times for diffraction or ARPES measurements compared to conventional channeltron analyzers. (see more on detector physics in theory part 2.4).
To reduce any disturbing magnetic fields the AC and the analyzer are both shielded by μ-metal plates.
In order to reach ultra high vacuum (UHV) all chambers are pumped by a combination of two pumps. In the first pumping level a membrane pump acts as roughing pump to create the pre-vacuum for all turbo molecular pumps (TMPs). These TMPs are the second pumping level and maintain the UHV. The AC and the analyzer are pumped by a PFEIFFER Hi Pace 700 TMP and the PC and manipulator are pumped by a Hi Pace 300. The entry lock and some smaller vacuum pipes, *e. g.* the connecting pipes to the Attoline, the gas tree and the He lamp capillary

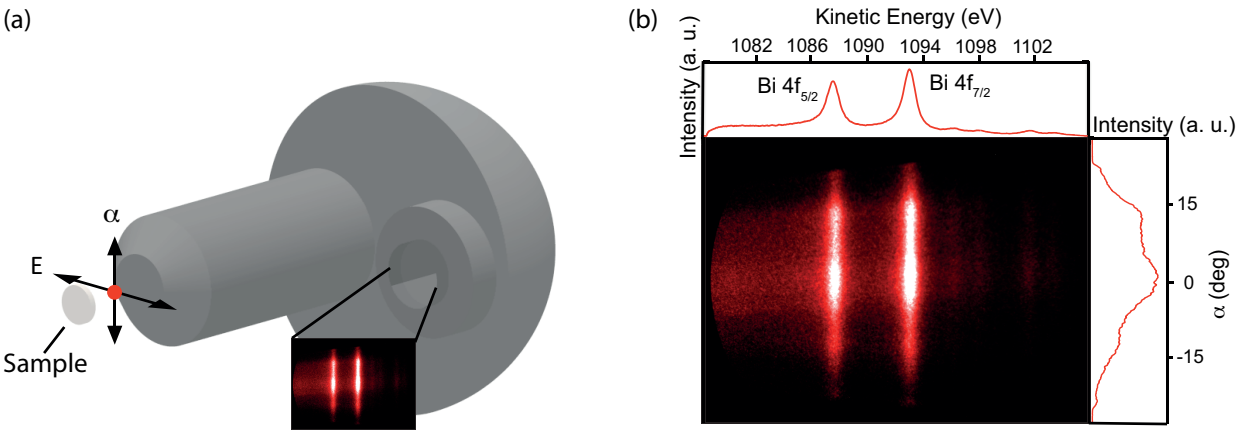

Figure 3.3: (a) Illustration of the analyzer's scanning axes: in the vertical direction the emission angle α is mapped and along the horizontal axis the energy dispersion. (b) A raw image from the CCD camera recording the angular and energy distribution of the Bismuth 4f core levels. At the outer margins an integration over the whole corresponding axis is presented.

are pumped by a Hi Pace 80. The plasma chamber of the He discharge lamp has its own pumping stage consisting of a membrane roughing pump and a drag TMP. Figure 3.4 shows a diagram of the vacuum system. After a bake out of the chambers a base pressure of $p < 1 \cdot 10^{-10}$ mbar can be reached. The pressures in AC and PC are measured by ion gauges, while the pressure close to the multi purpose pump is measured with cold cathode and pirani combination. Another cold cathode gauge detects the pressure after the drag pump that creates the vacuum for the He discharge chamber. All prevacuum pressures are measured with pirani gauges.

To prevent damage from the various devices and the turbo pumps in case of vacuum accidents or electrical power break downs, an interlock system was implemented. This system controls the two pneumatic valves between the large TMPs and the chambers, another pneumatic valve that can close the connection to the Attoline, the analyzer voltages and a valve between the roughing pump and the TMPs. Once the rotation speed of a TMP is reduced below a given set point a relay inside the electronic unit of the pump switches causing the pneumatic valve to close. The pneumatic valve to the Attoline is controlled via the pressure in the AC (p_{ac}) and a pressure gauge on the Attoline side located at the "New Cross" chamber. If any of the two pressures exceed a given value, a relay at the back of the PC pressure control unit switches and causes the valve to close. The analyzer voltages are controlled via the pressure in the PC (p_{pc}). If p_{pc} exceeds a certain set point, another relay at the back of the PC pressure control unit switches and the analyzer voltages are set to 0 V to prevent the detector from destructive sparking. Note that p_{pc} instead of p_{ac} is the relevant parameter. This leaves the possibility to switch off the ion gauge that measures p_{AC}, if measurements are sensitive electrons emitted by the ion gauge filament. In case the prevacuum pressure exceeds a certain value, yet another relay at the back of the PC pressure control unit causes the valve between roughing pump and TMPs to close. A means to hinder the pneumatic valves from reopening after an accident is not implemented, yet.

As another safety measure in the case of an electrical power break down an uninterrupted power supply was installed. It is a large battery and can deliver the power supply for the two large TMP pumps, the pressure gauges and the interlock system up to half an hour.

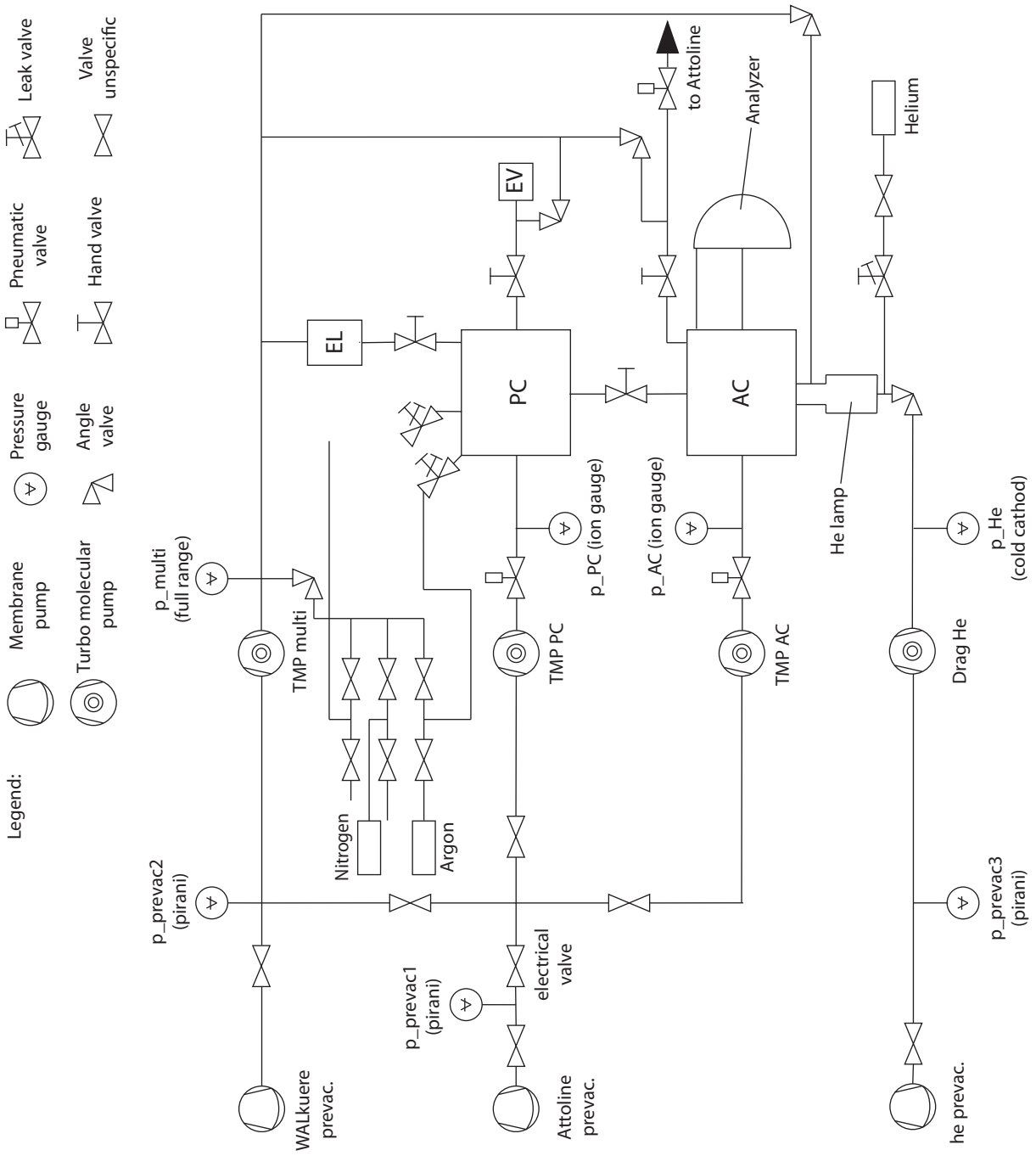

Figure 3.4: Diagram of the WALküre vacuum system, including all valves, pumps and gas lines. Abbreviations EL and EV stand for entry lock and evaporator respectively.

3.2 Survey of the Attoline

The Attoline [45] emits pulsed XUV light in the range of 20 eV - 70 eV to the sample inside the WALküre apparatus. The pulses are generated by HHG from intense infrared laser pulses with the wavelength of $\lambda \approx 800$ nm and a repetition rate of 1 kHz. The source of the 800 nm pulses is a Ti:Saphire laser. Figure 3.5 shows a schematic overview of the Attoline and the WALküre chamber.

In the topmost chamber shown in Fig. 3.5 (a) the operator can choose between two IR beams with different beam energy coming from T1 ($E_{max} = 10$ mJ) or T2 ($E_{max} = 1.3$ mJ) respectively. The chosen beam can be compressed using two different mechanisms (filament or fiber compression) to a minimum of 6 fs time duration per pulse. The maximum energy of such a compressed pulse is $\approx$ 600 μJ. In the second chamber in (a) the beam is split: While 80% of the power are transmitted by the beamsplitter (BS), 20% are reflected. The 80% are directed in the third chamber, where the beam is focussed into a gas target (GT) to create higher harmonics [55]. To influence the line shape of the HHG photon signal the iris I1 and the position of the gas target that is situated on a xyz-stage can be adjusted in order to create ideal phase matching conditions. The filter wheel (FW) in the third chamber contains different metallic filters to eliminate the residual IR signal from the beam path and to cut certain undesired harmonics depending on the experimental needs. In order to recombine the beam reflected by the beam splitter with the transmitted one, a drilled mirror (DM) is used, where the XUV can pass through the hole and the IR is reflected. A convex mirror (FM) adjusts the divergence of the IR and XUV beams. The two beams are now aligned for pump-probe experiments. The delay of the two beams can be adjusted with a stack of 2 translation stages (TS1) comprising a coarse drive and a piezo crystal for fine delays adjustments. While the coarse drive covers a time delay of 167 ps with an accuracy of 2 fs, the fine piezo stage makes time increments of 21 as possible.

In Fig. 3.5 (b) a gold coated toroidal mirror (TORO1) focusses the two collinear beams to the same spot with an arm length of 1187 mm [45]. Another translation stage (TS2) can move either a beam profiler or a photodiode into the beam path. The beam profiler consists of an MCP photo screen assembly to visualize the spatial distribution of the XUV beam. Via a Keithley electrometer the photocurrent from the diode can be measured. Outside of this chamber a silver mirror can be inserted into the beam path to couple the beams out of the beamline and to adjust the temporal and spatial overlap. Note that for this adjustment the residual IR that co-propagates with the XUV as well as the IR used for HHG generation are used instead of the XUV pulse.

Figure 3.5 (c) shows a chamber comprising two gas targets to measure either transient absorption or photoelectrons and photoions, respectively. For photoelectron spectroscopy a time of flight (TOF) spectrometer is attached to this chamber. The gas phase measurements that are used for normalization of the XUV intensity are preformed with this TOF. The target for photoelectron spectroscopy is a gas jet that is inserted through a stainless steel needle. For transient absorption measurements the gas is injected through a pulsed piezo valve that works with 1 kHz frequency and is synchronized with the laser. Efficient differential pumping maintains a pressure of $5 \cdot 10^{-8}$ mbar in the spectrometry chamber while the pressure in the generation chamber is $3 \cdot 10^{-3}$ mbar.

The topmost chamber in (d) contains a mobile spherical mirror that projects the two co-propagating beams into the XUV spectrometer which can measure photons up to 124 eV. Additional metal filters block the IR beam to prevent damage from the spectrometer. With the spherical mirror retracted, the beams are refocused by the second toroidal mirror (TORO2) with an arm length of 1000 mm onto the sample in the AC of the WALküre apparatus. In that way pump-probe experiments with pulsed IR and pulsed XUV can be conducted on a surface.

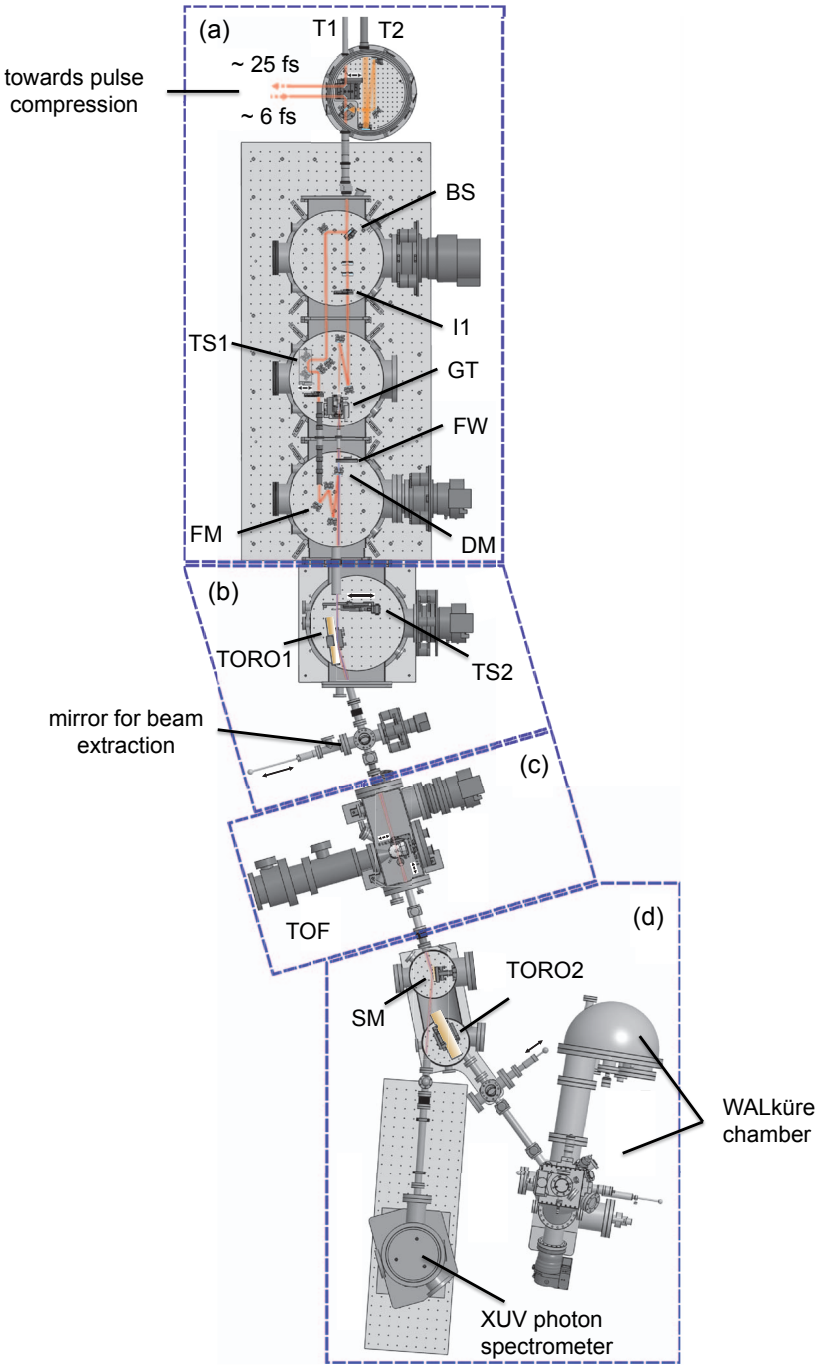

Figure 3.5: Top view on the Attoline and the WALküre apparatus. (a) beam coupling and XUV generation chamber, (b) chamber for beam analysis and beam focussing, (c) chamber for gas phase measurements with a time of flight (TOF) spectrometer, (d) refocussing chamber for surface experiments at the WALküre with the hemispherical analyzer and XUV photon spectrometer. Picture taken from [45]

4 Diffraction measurements with a wide angle lens 2D analyzer

In the following chapter large parts of the text and the figures are taken from the author's work published in [56]

After the assembly of the WALküre, in a next step routines for diffraction measurements with the WAL analyzer had to be developed. These routines where implemented in the measurement software, which controls not only the scanning parameters of the detector but also the motion of the motors rotating the sample. Therefore in this chapter an efficient and fast way to measure photoelectron diffraction data over the full 2π angular range with high data point density is presented, taking advantage of the massive parallel detection capabilities of modern two-dimensional electron detectors. Generic routines for data binning and for the mapping of the detector signal onto emission angles are introduced. X-ray photoelectron diffraction patterns taken from Bi(111) with the new detection scheme are compared to data sets taken with a conventional hemispherical analyzer equipped with a channeltron detector. As a result, the data acquisition time can be reduced by roughly a factor of ten while obtaining comparable if not superior data quality. The sampling technique is extended to uv-excited angle-resolved photoelectron spectroscopy as illustrated by a mapping of the Fermi surface of Cu(111).

4.1 Introduction

The quality of the structural information from XPD or UPD measurements depends on the angular resolution and sampling density, as well as the angular range covered by the measurement. A conventional hemispherical analyzer using a channeltron detector typically needs to sample several thousand points on the hemisphere, which translates into several thousand angle settings of the sample manipulator [53]. As an alternative route, parallel detection techniques were developed in the past. One approach leads to so-called display analyzers [57, 58]: in such detection schemes, the photoemission intensity distribution at a chosen electron kinetic energy is imaged onto a two-dimensional (2D) detector. This way, the diffraction pattern inside a large solid angle is measured in a parallel fashion. Despite recent improvements of the energy resolution (below 1% of the bandpass energy) [59] and of the acceptance angle (up to 1 sr solid angle) [60, 61] the energy scanning capabilities of such analyzers are limited. Another approach to parallel detection was the development of toroidal angle-resolving electron spectrometers with an acceptance angle of $\pm 90°$ in one direction [62]. In a modern generation a range of 8% of the electron pass energy can be simultaneously recorded [63]. The mentioned analyzers are quite complex and not commercially available.

Here it is shown how the PHOIBOS 150 WAL from the WALküre apparatus is efficiently used to record diffraction patterns. In the experiments presented here, a 40° long line on the hemisphere above the sample is recorded for each angle setting rather than a single point, reducing the necessary number of settings by more than a factor of ten compared to conventional channeltron detectors (see below). Measurement times, typically of the order of a few hours for a full diffraction pattern with conventional instruments, can be reduced accordingly while maintaining similar angular resolution and statistical accuracy. Shorter measurement times are important for several reasons: on the one hand many samples are sensitive to contamination by the residual gas even under ultra-high vacuum (UHV) conditions and their surfaces degrade on the time scale of hours. On the other hand surfaces with molecular adsorbates, for instance, often suffer from radiation damage from the light sources. The damage is caused by photochemistry or inelastic scattering of secondary electrons. Thus a faster measurement means less damage to the sample.
Also in a possible time resolved diffraction measurement with pulsed XUV light by HHG as probe beam short measurement times are of importance, as HHG light sources are often only stable over a limited time span of a few hours. Finally, the parallel data acquisition over a line of angles makes it possible to do pump-probe experiments on specific diffraction features -identified via first taking a full diffraction pattern- without moving the sample orientation.

4.2 Reconstruction of complete diffraction patterns from single detector images

Recording full 2π photoelectron angular distributions with an energy dispersive analyzer equipped with a 2D detector is different from using a conventional detector based on channeltrons. While a channeltron detector in fixed energy mode measures the intensity at one single emission angle at a time, the WAL analyzer captures a defined energy and angular range with a single snapshot of the 2D multichannel plate (MCP) detector as shown in Fig. 4.1. The same figure illustrates how the photoelectron signal is obtained by integration over the energy range of the peak. The inelastic electron background can be interpolated using the flat areas in the spectrum (*cf.* left and right marked areas in Fig. 4.1) and then be subtracted from the integral across the peak. This procedure yields the intensity distribution as a function of the detector angle $I(\alpha)$ (Fig. 4.2). Instead of single point measurements as in the case of a channeltron detector, the 2D detector samples data simultaneously from emission angles corresponding to a line along a great circle on the hemisphere as shown in Fig. 4.2. Such lines are recorded at different angular settings of the sample goniometer.
Figure 4.3 illustrates the angle convention used for the mapping of detector angle α and goniometer angles θ_{Man} and ϕ_{Man} onto the sample polar coordinates θ_{Sph} and ϕ_{Sph} describing the emission direction. The relation is not trivial. At $\theta_{Man} = 0°$ the line scan along the angle α coincides with a scan along the polar angle θ_{Sph} at fixed azimuthal angle ϕ_{Sph}. The other extreme is reached for $\theta_{Man} = 90°$, where the line along α becomes an azimuthal scan at constant $\theta_{Sph} = 90°$. For all other lines the relation $\theta_{Man} = \theta_{Sph}$ only holds at the detector center ($\alpha = 0°$). At detector angles $\alpha \neq 0°$ the angle set (θ_{Sph},ϕ_{Sph}) changes continuously. The transformation from the sample manipulator settings θ_{Man}, ϕ_{Man} and detector angle α to the spherical emission angles θ_{Sph} and

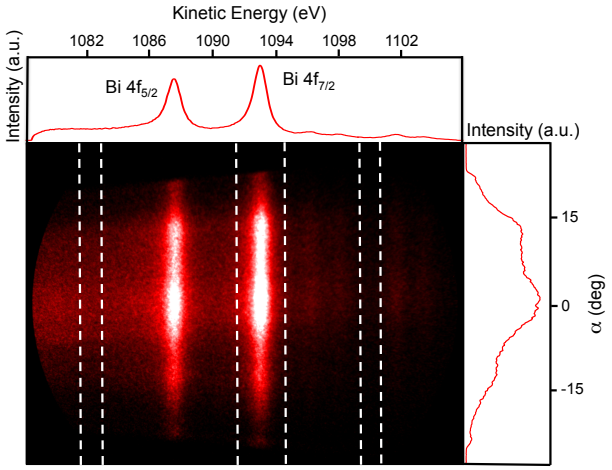

Figure 4.1: Snapshot of the 2D detector with the energy dispersive axis lying in the horizontal and the angular axis in vertical direction. The upper graph shows the angle-integrated energy spectrum of the two Bi 4f peaks. In the right panel the angular distribution of the Bi $4f_{7/2}$ peak integral is plotted. The integration borders are the two central dashed lines. The two lines on the low energy side and the two on the high energy side mark the areas that can be used to fit a linear or Shirley-type background [64] under the peak.

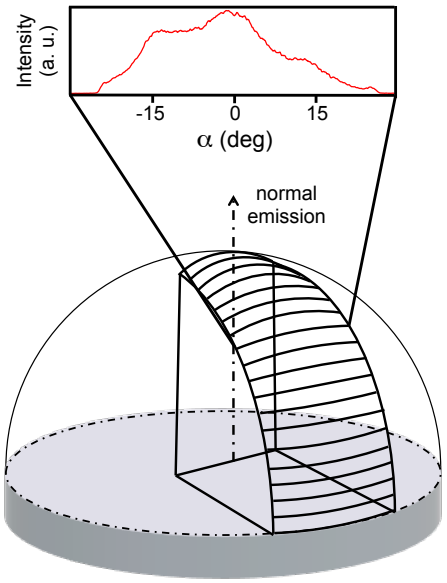

Figure 4.2: The Bi 4f peak on the MCP detector image is integrated and the resulting lines of intensities $I(\alpha)$, measured at different polar angles θ_{Man}, are assembled to form a broad slice out of the full 2π intensity distribution.

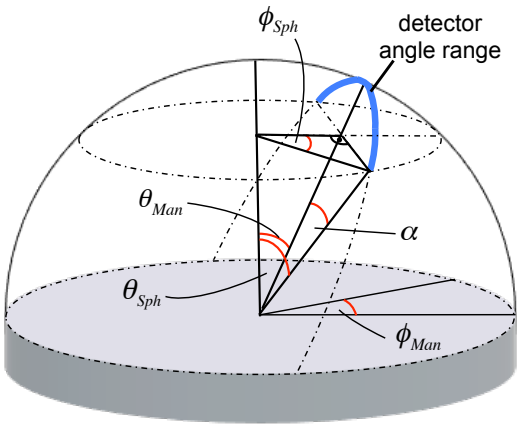

Figure 4.3: Overview of the characteristic angles describing the photoelectron distribution in our experimental geometry. The goniometer angles of the manipulator θ_{Man}, ϕ_{Man} and the detector angle α are converted to the spherical angles θ_{Sph} and ϕ_{Sph}. The thick blue arc indicates a single line recorded in one shot by the detector, which corresponds to a part of a great circle on the hemisphere above the sample.

ϕ_{Sph} is given in the following two equations:

$$\theta_{Sph} = \arccos(\cos\ \alpha \cdot \cos\ \theta_{Man}\ ) \tag{4.1}$$

$$\phi_{Sph} = \arccos\left(\frac{\tan\ \theta_{Man}}{\tan\ \theta_{Sph}}\right) \mathrm{Sign}(\alpha) + \phi_{Man} \tag{4.2}$$

To sample the angular distribution over the full 2π hemisphere, the following procedure is applied: first the polar manipulator angle θ_{Man} is rotated in small steps (typically 1° or 2°) from large manipulator angles ($\theta_{Man} \leq 90°$) to normal emission ($\theta_{Man} = 0°$) in order to record a slice of intensities on the hemisphere (Fig. 4.2). Due to low analyzer transmission at large detector angles α, signals for $|\alpha| > 20°$ are discarded. When the first intensity slice is completed, the sample is rotated around its azimuthal angle ϕ_{Man} by 40° before taking a second slice. Repeating this procedure nine times covers the whole range of 360° of azimuthal angles and thus the whole hemisphere. For a step size of $\theta_{man} = 2°$ this yields a total of 405 angle settings of the goniometer. The minimum acquisition time for a complete angular distribution is given by the time that the instrument needs to move the manipulator to the correct positions and to communicate with the detector. By performing a 2 π scan with 405 angle settings with the dwell time of the data acquisition set to $t = 1$ ms, the total time lag of a full scan is determined to be 13 minutes. This is the fastest possible full 2π scan with the current setup.
For the reconstruction of the diffraction pattern it must be considered that for every energy analyzer the recorded photoelectron intensity is proportional to a device specific transmission function that will also depend on the particular mode of operation [65]. Due to the two dispersive axes (angle and energy) the transmission function of the WAL detector depends on energy and detector angle, and therefore $I(E, \alpha) \propto T(E, \alpha)$. As the diffractogram is recorded at a fixed energy, the dependence on α is of concern here. The energy dependence must be taken into account for cases in which signals at different energies are compared, like in background measurements. However, the energy dependence of T is weak in this region and energy dependent changes negligible in most cases. Since the transmission function does not depend on the orientation of the sample, a

convenient way to find an approximate function for $T(\alpha)$ is to take the mean angular distribution on the detector averaged over all different sample orientations. This averaging leads to a smearing out of the diffraction pattern and reduces to the device specific transmission function $T(\alpha)$. This function is then used to normalize the measured signal $I(\alpha)$.
For graphical representation the photoelectron intensity distribution is finally projected onto a plane as shown in Fig. 4.4. To maintain an azimuthal conformal mapping the stereographic projection is used for the conversion of spherical angles to polar angles on a plane where $r(\theta_{Sph})$ is the radial coordinate, ϕ_{pol} is the angle coordinate of the plane and r_0 a scaling factor:

$$\begin{pmatrix} r(\theta_{Sph}) \\ \phi_{pol} \end{pmatrix} = \begin{pmatrix} r_0 \cdot \tan \frac{\theta_{Sph}}{2} \\ \phi_{Sph} \end{pmatrix} \tag{4.3}$$

In Fig. 4.4 the stereographic projection of a slice and the combination of slices to a full pattern is illustrated. While the left part of Fig. 4.4 shows only the positions of the measurement points, the right part displays the points with a color code corresponding to the intensities of a measured photoelectron diffraction pattern from a Bi(111) surface. The electrons were emitted from the Bi 4f core levels after excitation with Mg K_α photons of energy $h\nu = 1253.6$ eV. An angular step size of $\Delta\theta_{Man} = 2°$ was chosen, as this is sufficient to resolve the typical electron diffraction patterns. Along the detector angle α the minimum step size depends on the pixel density of the CCD camera. In order to reduce storage space, right at the data acquisition the pixels of the CCD raw images are binned so that $\alpha = 40°$ correspond to 64 angle channels, which results in an angular sampling density of 0.63° per angle channel. These angular scanning parameters lead to the grid of measurement points shown in Figs. 4.4 (a) and (b).
In Fig. 4.4 (b) it can be seen that for angular settings close to normal emission, i. e. close to the center of the diffraction pattern, individual slices overlap strongly. In order to have a uniform solid angle sampling density across the entire hemisphere, a data binning routine is applied where the overall point density is reduced and overlapping data points are averaged into a single data point. The optimized grid with the positions of the binned data points is presented in Fig. 4.4 (c). Matching the step size of the polar manipulator angle θ_{Man}, the grid points are spaced by $\Delta\theta_{Sph} = 2°$ and the step size in azimuthal angle at $\theta_{Sph} = 90°$ is $\Delta\phi_{Sph} = 2°$ and increasing for lower polar angles. The grid in Fig. 4.4 (c) has a constant sampling density, i. e. each point covers the same solid angle. The right panel of figure 4.4 (c) shows the binned data set of the Bi 4f XPD pattern from a Bi(111) surface. A three-fold symmetric diffraction pattern with distinct maxima is clearly visible.

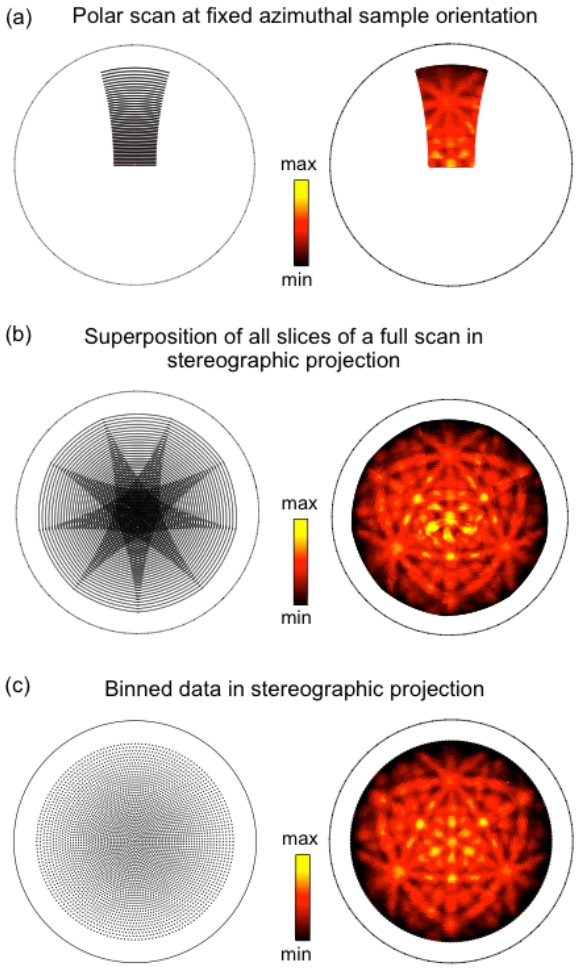

Figure 4.4: Reconstruction of an XPD pattern (Bi $4f_{7/2}$, $h\nu = 1253.6$ eV) in stereographic projection. The polar angle covers a range of $\Delta\theta_{Sph} = 0° - 80°$. The left panels show the grid points and the right panels the data points plotted in the corresponding color scale. (a) A single slice recorded with the WAL detector, scanning the goniometer angle θ_{Man} at fixed ϕ_{Man}. (b) Full XPD scan covering an azimuthal range of 360°, composed of 9 slices spaced at $\Delta\phi_{Man} = 40°$. (c) Same data but with intensities binned to a grid of constant solid-angle density.

4.3 Results

First XPD data collected with the WAL analyzer, using two different data acquisition speeds, are compared with corresponding data acquired with a conventional channeltron-based instrument [53]. In order to compensate for the weak signal at large polar angles, the XPD patterns are normalized with a fitted Gaussian function along the polar direction. As the sample has a three-fold rotational symmetry a three-fold rotational averaging is also applied. The results are shown in Figs. 4.5 (a) - (c), together with a corresponding simulation using multiple scattering and single scattering cluster theory (Fig. 4.5 (d)). All experimental patterns show the same diffraction features, which are furthermore well reproduced in the MSC simulation. While SSC calculations reproduce the main forward scattering peaks, the MSC has sharper features and a much richer fine structure becomes visible [66]. In the case of SSC calculations the code after Friedman was used. [28] and for MSC calculations the EDAC code was employed [67].
Although the main features of the diffractogram are already visible after a total measurement time of only 15 min (a) and with a wide entrance slit (3.0 mm along the energy dispersive axis) of the analyzer, the signal is clearer after 105 min (b) where a narrow entrance slit (0.5 mm along the energy dispersive axis) of the analyzer was used. This becomes more obvious in the lower part of Fig. 4.5 where the anisotropies in the corresponding diffraction maps are shown for an azimuthal cut at a fixed polar angle. The anisotropy is a measure for the angular modulation depth of the signal and is defined as

$$A(\phi) = \frac{I(\phi) - I_{\min}}{I_{\max}} \tag{4.4}$$

where $I(\phi)$ is the azimuthal angle dependent intensity, $I_{\min}$ the minimum and $I_{\max}$ the maximum intensity along the azimuthal cut. The noise is markedly reduced when the measuring time with the WAL analyzer is increased, i.e. in going from Fig. 4.5 (a) to (b), and the anisotropy amplitude for a circular scan at $\theta_{Sph} = 54°$ becomes larger. For comparison Fig. 4.5 (c) shows the same measurement with a conventional energy analyzer with a channeltron detector [53], where the overall measurement time exceeded 300 minutes. The maps in (b) and (c) look similar but the features in (b) are slightly more distinct than in (c). This is corroborated by the anisotropy curves. They show larger anisotropies and sharper features in (b) compared to the channeltron measurement in (c). This also indicates that, for the chosen analyzer settings, the angular resolution of the WAL analyzer is superior.
While for the measurements performed with the channeltron detector the x-ray gun can be moved very close to the sample [53], this is not the case in the vacuum chamber with the WAL analyzer, which results in a lower photon flux. This can be quantified by measuring the photocurrent of the sample, which is proportional to the photon flux. The photocurrent during the WAL measurements ($I_{Wal} = 21$ nA) shown in Figs. 4.5 (a) and (b) was smaller than during those of Fig. 4.5 (c) ($I_{Chan} = 67$ nA) by a factor of 3.2. Hence with comparable photon flux, data of the quality shown in Fig. 4.5 (b) could be measured in half an hour.
The described mapping technique works well also for lower-energy electrons emitted by uv light, in particular in angle-resolved photoelectron spectroscopy (ARPES) experiments. Fig. 4.6 shows a Fermi surface map of Cu(111) recorded with He I_α photons ($h\nu = 21.2$ eV) [68]. The sp-band crossing the Fermi level and the Shockley surface state are well visible. The mirror symmetry with respect to the $\bar{M}\bar{\Gamma}\bar{M}'$ plane is lifted due to photoemission matrix element effects. The asymmetry occurs because the plane of incidence of the light does not coincide with the mirror plane of the crystal in these measurements. As a consequence, the light polarization is different for measurements on the two sides of the mirror plane.

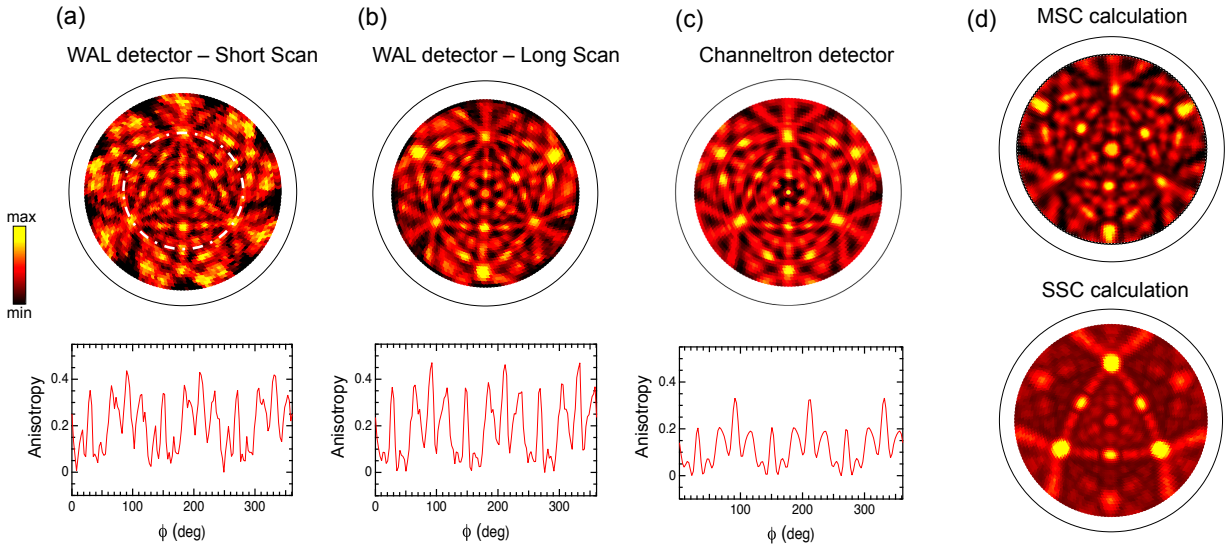

Figure 4.5: Comparison of different XPD measurements from Bi(111) (all data shown are taken on Bi $4f_{7/2}$ with $h\nu = 1253.6$ eV) (a) Fast XPD scan recorded with the WAL analyzer with a total measurement duration of 15 minutes. A wide entrance slit was used. (b) XPD pattern recorded with the WAL detector with narrow entrance slit and a measurement duration of 105 min. (c) XPD pattern recorded with a channeltron detector and a measurement duration of 300 min. All diffraction patterns were taken for polar angles $\theta = 0° - 80°$. Rotational averaging owing to the three-fold symmetry was applied and the data were normalized with a polar Gaussian function in order to reduce purely instrumental effects on the anisotropies. Below the three experimental patterns (a) through (c) the quantitative anisotropies of the corresponding data are shown *vs.* azimuthal angles ϕ_{Sph} for a circular scan at a polar angle $\theta_{Sph} = 54°$ as indicated by the dashed circle in (a). (d) Multiple scattering (MSC) and single scattering cluster (SSC) calculation of the Bi 4f XPD pattern.

The fact that the matrix elements are sensitive to the angle $\alpha_{\epsilon k}$ between the light polarization and the electron emission direction, and that even for unpolarized light the polarization is confined within the transversal plane perpendicular to the propagation direction, raises an issue for the data acquisition mode described in this work. In a channeltron-based instrument where one emission angle at a time is measured, $\alpha_{\epsilon k}$ is fixed for all data points. In the WAL analyzer, the detector spans a range of emission angles for a fixed goniometer position, which means that each detector angle α corresponds to a different angle $\alpha_{\epsilon k}$. For a quantitative theoretical description this variation of $\alpha_{\epsilon k}$ along the detector has to be taken into account.
The data in Fig. 4.6 are projected on the parallel momentum plane ($k_{||}$-plane) of the photoelectrons for a conformal representation of $k_{||}$. The relation between spherical and planar polar angles in this case is:

$$\begin{pmatrix} r(\theta_{Sph}) \\ \phi_{pol} \end{pmatrix} = \begin{pmatrix} r_0 \cdot \sin\ \theta_{Sph} \\ \phi_{Sph} \end{pmatrix} \tag{4.5}$$

where $r(\theta_{Sph})$ is the radial coordinate, ϕ_{pol} is the angle coordinate on the plane and r_0 is a scaling factor.

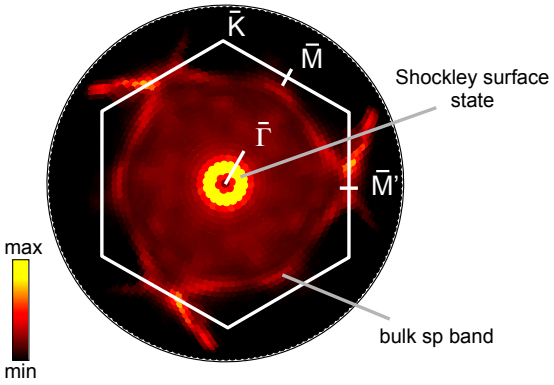

Figure 4.6: Fermi surface map of Cu(111) recorded with He I_α ($h\nu = 21.2$ eV). The white hexagon indicates the borders of the first surface Brillouin zone (SBZ) with the high symmetry points $\bar{K}$, $\bar{M}$ and $\bar{M}$' indicated. The contours crossing the SBZ boundaries correspond to sections through the bulk Fermi surface while the bright circular contour near the center shows the Shockley surface state [68].

4.4 Summary

Using a 2D detector in combination with a wide-angle lens for photoelectron diffraction measurements enables us to reduce the measurement time of diffraction maps by nearly a factor of ten in comparison with conventional instruments, while improving the data quality. The fact that for one sample orientation a wide range in angle can be covered, demands a new way to map the photoelectron intensity distribution over the 2π hemisphere above the sample. This mapping procedure is described and it is shown that the procedure works for both, high-energy (XPD) and low-energy electrons (UPD or ARPES).
The significant reduction of measurement times makes the mapping of diffraction patterns or ARPES data possible even if sample surfaces are sensitive to contamination by residual gas or to radiation damage, which both limit the sample life time. The time factor is also important when light sources, such as complex laser systems like the Attoline [45], have a limited stability over time.

5 XPD and UPD of SnPc adsorbed on Ag(111) - A sensitivity study

In the following chapter large parts of the text and the figures are taken from the publication "M. Greif et al., Physical Review B 87 (2013) 085429" [11]

On the route towards time-dependent diffraction measurements the following chapter acts as sensitivity study. The information gained by XPD and UPD, if applied to molecular monolayers on surfaces, are compared. Especially the sensitivity of UPD to molecular adlayers is tested: The bonding geometry of tin-phthalocyanine (SnPc) on Ag(111) has been studied using XPD and UPD, respectively. Experimental diffraction patterns were compared to single-scattering-cluster calculations. XPD data could be well reproduced by the simulations and allowed for the determination of several structural parameters. At a coverage of 0.9 ML all molecules are in a "tin-down" configuration and the non-planar shuttlecock-shaped SnPc molecule undergoes flattening upon absorption on Ag(111). UPD data from the second highest occupied molecular orbital (HOMO-1) turn out to be highly sensitive to minor structural changes, including also the vertical distance between tin atoms of the SnPc and the surface layer of the substrate, which is found to be 2.3 Å. Thus it is demonstrated how UPD can complement the well-established XPD method and remaining challenges in the theoretical description of photoelectron diffraction from molecular orbitals at low energies are discussed. The UPD method is particularly attractive in view of pump-probe experiments using XUV pulses from HHG as probe. This sort of experiment would combine high structural sensitivity with ultra short time resolution.

5.1 Introduction

While the mechanisms of core-level photoemission and final state scattering and diffraction exploited in XPD are largely understood [69], the means to analyze diffraction patterns of photoelectrons with much lower kinetic energies, such as UPD, are much less explored. Enhanced backscattering in UPD leads to stronger contributions of additional scattering pathways, thereby promising to deliver even more information than XPD. This comes at the cost of more complex diffraction patterns which are further complicated by dominating interference effects, while in XPD the presence of strong forward scattering enhancements often provides a direct fingerprint of the arrangement of atoms in the near-neighbor shells of a photoemitter [70]. The currently largest obstacle to overcome, however, comes from the fact that UV-excited photoelectron spectra are typically restricted to emission from valence states and molecular orbitals, where an accurate theoretical description of the photoemission process and the final state scattering is only just emerging [71]. A combination of photoelectron diffraction with newly available pulsed light sources

in the UV-XUV regime, *e. g.* via high harmonics generation (HHG) [55], could lead to a powerful method to study structural dynamics at the atomic scale with femtosecond temporal resolution. In this chapter it is demonstrated that UPD can indeed be used to retrieve structural parameters of a complex molecular adsorbate system and that the interference patterns are sensitive to even very small structural changes.
The interpretation XPD and UPD patterns is based on scattering-cluster calculations [30]. Such calculations proved their value in modeling XPD patterns of core level emission of adsorbates [10] and of pristine metal surfaces [70], even at the single-scattering level. The SSC formalism was also successfully applied to the modeling of d-band integrated UPD measurements of Cu valence states [23], where the scattering approach was further validated by multiple scattering methods [26].
Instead of interpreting a UPD map as a diffraction pattern, recently the same mapping technique was used to perform orbital tomography of organic molecules on surfaces [72–74]. In these studies the spatial distribution of the electronic wave function is calculated via a 3-D Fourier transformation of the measured photoelectron intensity distribution.
Tin-phthalocyanine (SnPc) adsorbed on Ag(111) was chosen as a model system to demonstrate the sensitivity of a combined XPD/UPD study to structural parameters and potentially to structural dynamics. It represents a sufficiently complex system that has been studied extensively by other methods in the last few years. Comprehensive work by Stadler *et al.* [75, 76] using photoelectron spectroscopy, x-ray standing wave (XSW) measurements as well as LEED studies shows that SnPc adsorbs in the monolayer with the molecules lying flat on the Ag(111) surface. At sub-monolayer coverage the ad-layer has different structural phases, which are associated with a conformational change of the SnPc molecule. Conformations with the Sn atom on top of the molecular plane ("tin-up") or with the Sn atom beneath the molecular plane ("tin-down") were identified. The different geometrical phases can be tuned via temperature and coverage. The mechanisms driving those phase transitions are intermolecular attraction and repulsion due to charge transfer between the chemisorbed molecular monolayer and the silver substrate [75]. While DFT calculations for the molecule in the gas phase predict a non-planar, shuttlecock-shaped structure, XSW measurements as well as density functional theory (DFT) calculations [77] show that the molecules undergo a flattening upon adsorption. Additional photoelectron spectroscopy studies yielded insights into the electronic structure of the system [78]. Other experiments employing scanning tunneling microscopy (STM)[79, 80] added further geometrical information about this system, such as the rotational orientation of the molecules with respect to the substrate surface. A recent DFT study investigated how the highest occupied molecular orbitals (HOMO) are involved in the bonding mechanism of the SnPc to the metal substrate [77]. It was found that the second highest occupied molecular orbital (HOMO-1) plays an important role in the chemical bonding of molecules and substrate.
In the first part of this chapter XPD measurements of core levels of the molecular tin atom are presented. Geometrical parameters obtained from these measurements and further parameters drawn from literature serve as a reference to analyze and interpret the more complex UPD patterns in the second part of this chapter. In the UPD measurements emission from the HOMO-1 orbital of SnPc was recorded. This study shall demonstrate the high sensitivity of UPD to electronic and structural parameters.

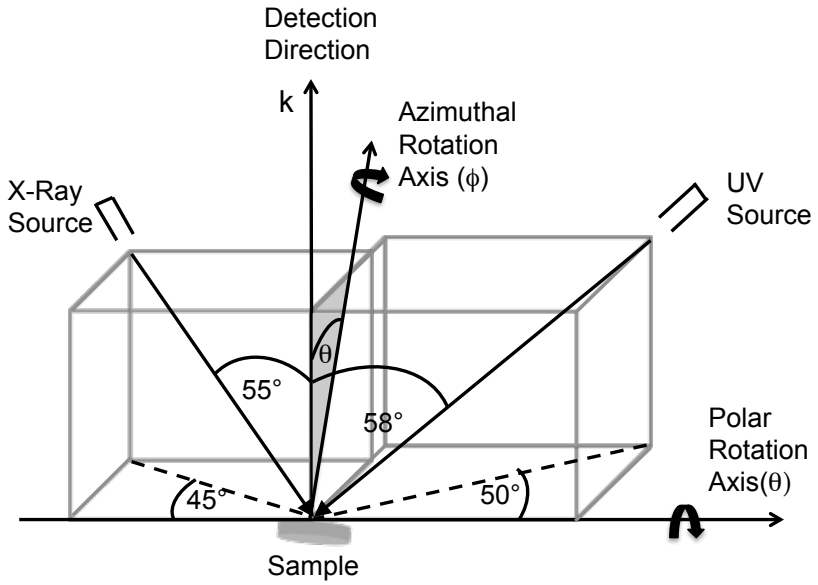

Figure 5.1: Sketch of the measurement geometry in the experimental XPD/UPD setup. The incident light has a fixed direction with respect to the detection direction. The sample can be rotated about the polar rotation axis and the azimuthal rotation axis, as indicated by the curved arrows.

5.2 Experimental

All experiments in this chapter were carried out in the modified VG ESCAlab 220 photoemission spectrometer and not at the WALküre as it was not ready for these kind of measurements at this time. In the ESCAlab was a base pressure of $p = 1 \cdot 10^{-10}$ mbar [53]. As light sources the He I_α (photon energy $h\nu = 21.21$ eV) and the Mg K_α ($h\nu = 1253.6$ eV) lines were used. All measurements were performed at room temperature. Fig. 5.1 illustrates the geometry of the experimental setup.
The Ag(111) substrate was cleaned with several sputtering and annealing cycles to prepare a clean and well ordered surface. The surface quality was then checked by XPS, UPS, and LEED. SnPc films were prepared at room temperature from resublimed SnPc powder evaporated from a self-made Knudsen cell. The pressure during the preparation was below $1 \cdot 10^{-8}$ mbar. After evaporation the sample was annealed for five minutes at a temperature of 150°C. As indication for sufficient annealing one needed to make sure that the adsorbate superstructure was homogeneous over the sample by taking LEED pictures from different sample spots. As the superstructure homogeneity was also a crucial criterion in the annealing recipe in Stadler's work, [75] the disappearance of multiple superstructures through annealing was taken as a sign that the molecules had gained enough thermal energy to move over terrace steps of the sample and that the sample was sufficiently annealed.
The evaporation rate was calibrated via the phase transition of SnPc at 0.9 ML from the diffuse to the incommensurate superstructure at room temperature, which can be verified by LEED measurements [75]. Additional XPS measurements confirmed the found evaporation rate. This resulted in an accuracy in the SnPc coverage of ±0.05 ML.

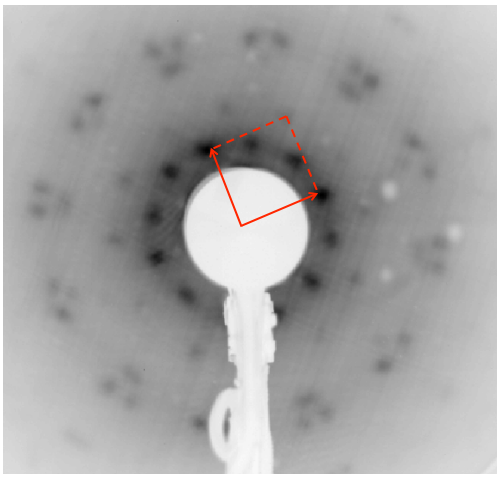

Figure 5.2: LEED pattern of 0.9 ML SnPc on Ag(111) recorded at an electron kinetic energy of $E_{kin} = 23$ eV. An incommensurate superstructure of the SnPc molecules with six domains is visible. Note that the substrate 1x1 spots are far outside the presented image frame.

As known from the LEED analysis by Stadler *et al.* [75], SnPc on Ag(111) has three phases with different superstructures in the single-layer regime. In this chapter the focus is on the incommensurate phase found at 0.9 ML coverage at room temperature, where all molecules are adsorbed in the "tin-down" conformation. Figure 5.2 presents the LEED data from a representative sample at this particular coverage. The spot pattern consists of six domains: three rotational domains multiplied by two because of an additional mirror symmetry. The superstructure matrix [81] of the individual domains is

$$\begin{pmatrix} 5.64 & 2.66 \\ -0.07 & 4.86 \end{pmatrix}.$$

5.3 Structural parameters from XPD

In this section the results of XPD measurements are presented and it is demonstrated how they provide information about the structure of SnPc adsorbed on Ag(111). All XPD measurements were performed with Mg K_α light. The Sn $3d_{5/2}$ core level of the central Sn atom in the SnPc molecule was chosen as emitter, *i. e.* the inelastic background subtracted Sn $3d_{5/2}$ photoemission intensity distribution is measured as a function of emission angles at constant kinetic energy of the electrons [24]. To account for the mostly instrumental polar intensity background, a Gaussian shaped polar background profile was subtracted from every pattern. In Fig. 5.3 (f) the XPD pattern of 0.9 ML SnPc on Ag(111) is shown: 12 equidistant maxima centered at a polar angle of $\theta = 74°$ are visible (label α). The four-fold symmetry of the individual molecules is not directly reflected in these data. Due to the three-fold rotational symmetry of the substrate the molecules adsorb in three equivalent orientations, leading to this 12-fold arrangement of maxima (see discussion below). Hence the data can be three-fold averaged in order to increase the statistical accuracy of the data. No further symmetrizing was applied. The averaged pattern is shown in Fig. 5.3 (g). Small variations in the intensities of the 12 maxima remain after the averaging process, hinting at the possibility that the three orientational domains might not be equally populated. This may

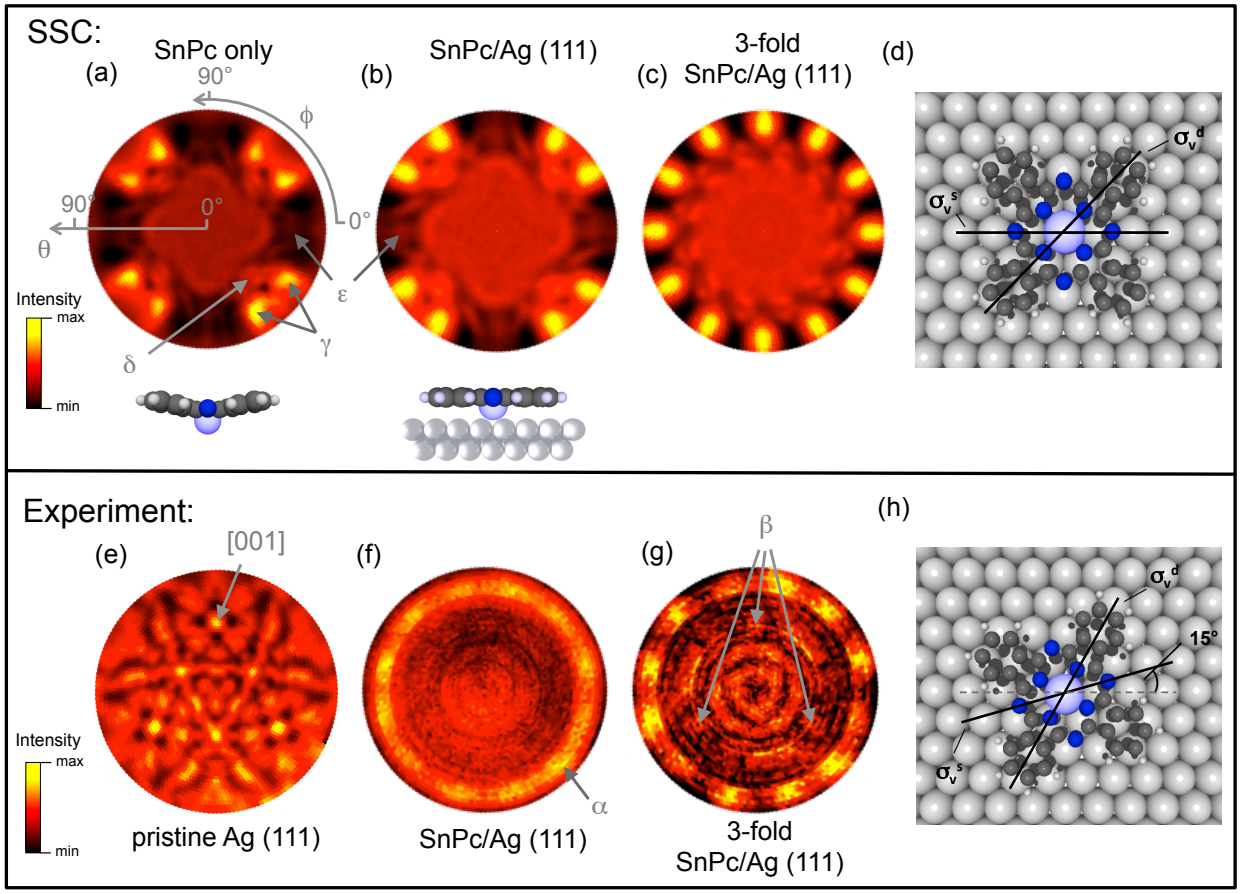

Figure 5.3: XPD measurements and corresponding SSC calculations from SnPc/Ag(111). (a) SSC of a non planar free SnPc molecule (molecule shown in the inset below). (b) SSC pattern of an adsorbed molecule in a flattened geometry as taken from Stadler *et al.*[75] (c) three-fold averaged SSC pattern of (b). The experimental pictures show in (e) an XPD pattern of the Ag $3d_{5/2}$ state of the clean Ag(111) substrate, in (f) the inelastic background-subtracted pattern of a 0.9 ML thick film of SnPc on Ag(111) and in (g) the three-fold averaged pattern of (f). All diffraction patterns show a polar range reaching from normal emission in the center of each picture to $\theta_{\max} = 82°$ at the outer border. All patterns were Gaussian background subtracted. With the excepion of (e), the emitter is always the Sn $3d_{5/2}$ core state. Labels α through ε mark selected spots that are referred to in the text. (d) SnPc molecule and its orientation with respect to the Ag-substrate, as it was used in the SSC simulation in (b) and (c). (h) Experimental rotational orientation of the SnPc molecules with respect to the Ag(111) substrate. The diagonal vertical mirror plane σ_v^d of SnPc aligns with the direction of the rows of Ag atoms, and the orientation is thus rotated by 15° with respect to the molecule in (d).

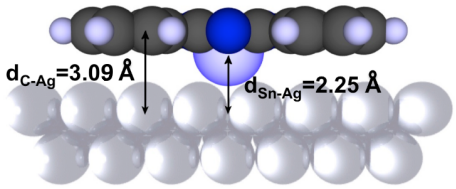

Figure 5.4: Illustration of the adsorption geometry of the flattened SnPc on Ag(111) in an arbitrary adsorption site.

occur due to a slight miscut of the crystal surface, leading to steps running along preferential directions. More to the center of the three-fold averaged XPD pattern [Fig. 5.3(g)] weaker features are visible that show a clear three-fold symmetry. The three weak spots at $\theta = 55°$ that are labeled with β are exactly at the positions where the substrate XPD pattern of Ag $3d_{5/2}$ (Fig. 5.3(e)) shows pronounced maxima along the next-nearest-neighbor directions [001], [100], and [010]. They might not be intrinsic to the Sn $3d_{5/2}$ XPD pattern but result from the incomplete subtraction of the spectral background which has imprinted a three-fold diffraction pattern from inelastically scattered photoelectrons from the substrate. The broader signals at similar polar angles are not completely understood and will not be discussed further.
To show how the experimental result can be interpreted a series of SSC simulations is presented in Figs. 5.3 (a) to (c) that demonstrate the evolution of the pattern as the cluster is more and more adjusted to match the actual bonding geometry of the SnPc molecules. Figure 5.3(a) shows the SSC result for a cluster with the atoms of a single free-standing SnPc molecule in the "tin down" conformation, *i.e.* the solid angle covers the hemisphere for positive values of the z coordinate and the Sn-atom is located below the molecular plane in the negative z-direction. The coordinates of the atoms in the cluster are taken from a DFT calculation for a free SnPc molecule. The calculations were performed with TURBOMOLE [82] using the basis set def2-TZVPP and an effective core potential for Sn. The exchange correlation functional was PBE0 [83]. In the figure one can see a four-fold symmetric pattern where each of the four pairs of bright maxima at a polar angle of $\theta = 68°$ (label γ) is the result of forward scattering at the two nearest carbon atoms in the pyrrol-like ring (see model of molecular structure in Fig. 5.3 (d)) . Next to each pair, at a slightly lower polar angle, one can see a local intensity maximum resulting from a nearest-neighbor nitrogen atom (label δ). Rotated by an angle of 45° in azimuth are weak structures labeled with ε, each caused by one of the four other nitrogen atoms.
The next step in the series is the simulation with a cluster where the molecule is adsorbed on the Ag(111) substrate [Fig. 5.3 (b)]. The cluster includes the first two atomic layers of Ag atoms underneath the molecule. XSW data [75] showed that the molecules undergo a conformational change upon adsorption on Ag(111): The slightly shuttlecock-shaped phthalocyanine backbone is flattened and the Sn atom in the center moves closer to the molecular plane. As result an Ag-Sn distance along the z-axis of $d_{Sn-Ag} = 2.25$ Å and a Ag-C distance along the z-axis of $d_{C-Ag} = 3.05$ Å was measured. An illustration of the adsorption geometry is shown in Fig. 5.4.
In the second simulation [Fig. 5.3 (b)] the molecular geometry is adjusted to these parameters. As expected, by flattening the molecule the brightest features move towards higher polar angles ($\theta = 76°$), which is close to those found in the experimental data ($\theta = 74°$). This is seen more clearly in Fig. 5.5, where polar intensity distributions averaged over all azimuthal angles are presented. The measured data are compared to the simulations of the flattened molecule and of the

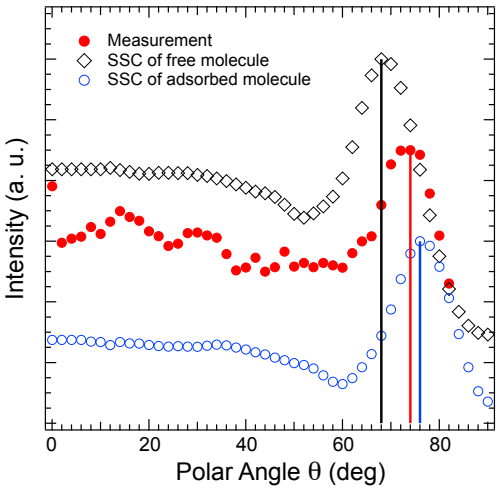

Figure 5.5: ϕ-averaged polar intensity distribution of the results from Fig. 5.3. The measured XPD pattern (red filled circles), the SSC patterns from a molecule in the adsorbed (flat) geometry (blue open circles) and in the free (shuttlecock) geometry (black open diamonds) are shown. For the sake of clarity a vertical offset was added to each spectrum.

free molecule. The polar position of the experimental maxima is much closer to the simulation performed with the flattened molecule, thus confirming the XSW result.
Since the superstructure of the adsorbate is incommensurate with the substrate periodicity, there is not only a single well-defined adsorption site on the Ag(111) unit cell. The molecules occupy a continuous range of adsorption sites on the surface. To account for this in the calculations, the substrate unit cell was discretized into a grid with 20 equidistant adsorption sites and the calculation was repeated as many times, each time with a single molecule adsorbed on a different site. Afterwards the outcome of all 20 SSC calculations was averaged. The azimuthal orientation of the SnPc molecules with respect to the Ag-substrate in the cluster was chosen as shown in Fig. 5.3 (d): the vertical molecular mirror plane σ_v^s is aligned with the unit cell vector of the Ag(111) substrate, *i.e.* along rows of Ag atoms in the surface. As already mentioned in the theory part, for electrons from the Sn $3d$ core levels with kinetic energies of 772 eV, there are nearly no contributions to the pattern from electrons backscattered off Ag atoms. This can also be seen in Fig. 5.3 (b): The Sn emitter located below the molecular plane but on top of the substrate gives no signal that can be attributed to the substrate structure. Calculating a scattering pattern for a cluster with the molecule in the flattened adsorption geometry but without the Ag substrate confirms this finding (not shown).
The three-fold symmetry of the substrate surface leads to the coexistence of three different azimuthal orientations of the adsorbed molecules, rotated by $\Delta\phi = 120°$ with respect to each other. Accordingly, to obtain the pattern shown in Fig. 5.3 (c), the result from Fig. 5.3 (b) was rotated twice by $\Delta\phi = 120°$ and the average of all three orientations was plotted. This reproduces the 12 main maxima found in the XPD measurements. Comparison of the experimental patterns in Figs. 5.3 (f) and (g) with the SSC simulation in Fig. 5.3 (c) reveals an azimuthal offset of $\phi = 15°$ for the 12 outer maxima between experiment and simulation. A rotation of the molecule in the cluster of $\Delta\phi = 15°$ relative to the Ag(111) surface, as illustrated in Fig. 5.3 (g), reveals that the molecules preferentially align the diagonal vertical molecular mirror plane σ_v^d (see Fig. 5.3 (g)) along the dense rows of Ag atoms. Taking this rotation into account, the 12 main maxima appear

at the same azimuthal and polar region as in the measurement. A similar rotational orientation was proposed by Stadler [84] and was also found in STM experiments [79].
Additional information about the degree of order within the molecular layer can be gained by comparing the anisotropy

$$A = \frac{I(\phi) - I_{\min}}{I_{\max}}$$

between the experimental and the simulated data, as a measure for the diffraction contrast. Here, $I_{\max}$ is the intensity on a diffraction peak and $I_{\min}$ the minimum along the azimuthal cut at a fixed polar angle. $I(\phi)$ is the intensity of the investigated angle. For the peak labelled α at $\theta = 74°$ in Fig. 5.3 (f) $A = 0.17$ was calculated. For each of the maxima in Fig. 5.3 (c) the anisotropy is A=0.47. The reasons for the smaller value in the experiment are as follows: (i) incomplete subtraction of the inelastic electron background from the experimental data can easily reduce the anisotropy; (ii) due to uncertainties in the treatment of thermal vibrations of the scatterers relative to the emitter, the SSC calculations tend to show larger anisotropies [25]; (iii) in the experiment some molecules might not be perfectly aligned in the geometry as shown in Fig. 5.3 (h), which also reduces the experimental anisotropy.
Summarizing, in this section it is shown that with XPD the geometry of the system SnPc/Ag(111) can be characterized, leading to structural conclusions that are consistent with the existing literature. The polar position of the dominant scattering features in the intensity distribution shows that the molecular backbone of SnPc is flattened upon adsorption and that the Sn atom moves closer to the molecular plane. The distance between Sn-atom and molecular plane was determined to be 0.84 Å. The distance between the Sn atom and the Ag surface could not be found with XPD due to the lack of backscattering features. From the azimuthal position of the intensity maxima the azimuthal orientation of the molecules with respect to the Ag surface could be found: The diagonal vertical mirror plane σ_v^d of SnPc, is aligned with the direction of dense atomic rows of Ag atoms.

5.4 Structural parameters from UPD

For the same system of 0.9 ML SnPc on Ag(111) also UPD measurements were performed. The goal was to demonstrate the sensitivity of low kinetic energy photoelectron diffraction patterns to molecular adsorbate structures, and the potential power of such measurements with respect to structural changes. Due to a much higher probability for backscattering, not only azimuthal orientation and conformational structure of the molecule, but also the molecule-substrate distance and bond lengths can potentially be extracted. However, the interpretation of UPD patterns is much less straightforward than in the case of XPD. The higher complexity of the initial states and of the scattering processes producing the UPD patterns demand a more elaborate theoretical treatment. Molecular orbital initial states in the valence region are more complex than spherically symmetric core states. Moreover, the muffin tin approximation becomes less accurate for slow electrons, and the surrounding potential in which the photoelectrons move is more difficult to compute compared to the XPD case.
To excite the HOMO-1 molecular orbital in the UPD measurement, He I_α radiation ($h\nu = 21.2$ eV) was used. In Fig. 5.6 the valence region of the system SnPc/Ag(111) as well as of the clean Ag(111) substrate is shown. The spectrum of SnPc/Ag(111) shows three peaks that correspond to molecular orbitals. The extra intensity observed right at the Fermi edge indicates emission from the LUMO. Due to charge transfer from the surface to the molecule this state is partially occupied

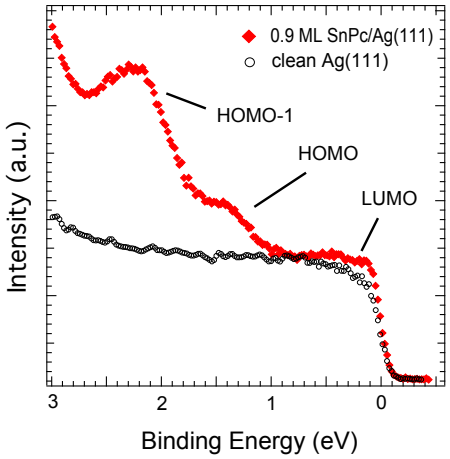

Figure 5.6: UPS spectra near E_F excited with He I radiation ($h\nu = 21.2$ eV) of pristine Ag(111) (black open circles) and of 0.9 ML SnPc/Ag(111) (red diamonds) showing the highest occupied molecular states (see text for labeling of states). The latter spectrum was recorded at normal emission, while the clean surface spectrum was measured $\Delta\theta = 5°$ away from normal in order to avoid the surface state appearing close to E_F. [85]

when the molecule is adsorbed on an Ag(111) surface [78]. There appears to be another weak feature at $E_B = 0.41$ eV, slightly down-shifted from the LUMO, which might be attributed to an interface state created by the adsorption of the SnPc molecules on Ag(111). Such interface states have been reported for other systems with organic molecules adsorbed on metal surfaces [86, 87]. However it was not seen in earlier works [88] and therefore could also be noise in the data. The two peaks at binding energies of 1.35 eV and 2.2 eV correspond to emission from the HOMO and HOMO-1, respectively. A DFT calculation with TURBOMOLE (*cf.* section 5.3) of the spatial distribution of these two orbitals in a free molecule is shown in Fig. 5.7 . The HOMO-1 has a pronounced *s*- and p_z-like character and is mainly localized around the Sn-atom of the molecule. In order to have a relatively simple molecular initial state that could be reasonably approximated by a single atomic orbital (a p_z orbital localized on the Sn atom), the HOMO-1 state was chosen as emitter. It provides also the strongest signal-to-background ratio in the spectrum.
Figure 5.8 (b) shows the experimental UPD pattern of the HOMO-1 of SnPc/Ag(111) after subtraction of the substrate-related background, which has been measured at the same binding energy on pristine Ag(111) (see Fig. 5.8(a)). The sharp contours in this background arise due to the strongly dispersing *sp* band of Ag moving through the binding energy window. They represent a section through a constant energy surface in the band structure of silver [89]. Due to their sharpness, and due to the dependence of the precise momentum mapping on the work function of the surface, some features persist in the background subtracted HOMO-1 UPD pattern, where they can be easily recognized. Due to the sensitivity of the molecules to radiation damage, UPD patterns were recorded only up to polar angles of $\theta = 60°$. This region includes the features with the highest anisotropy and thus the main information can be gained from this limited solid angle. As in the XPD measurement a ring of 12 intensity maxima is observed, which are significantly broader and appear at a smaller polar angle of $\theta = 50°$ (see label α in Fig. 5.8(b)). Again, the 12 maxima can be rationalized in terms of the four-fold rotational symmetry of SnPc placed on a three-fold symmetric substrate. But in contrast to the XPD data, a distinct three-fold symmetric

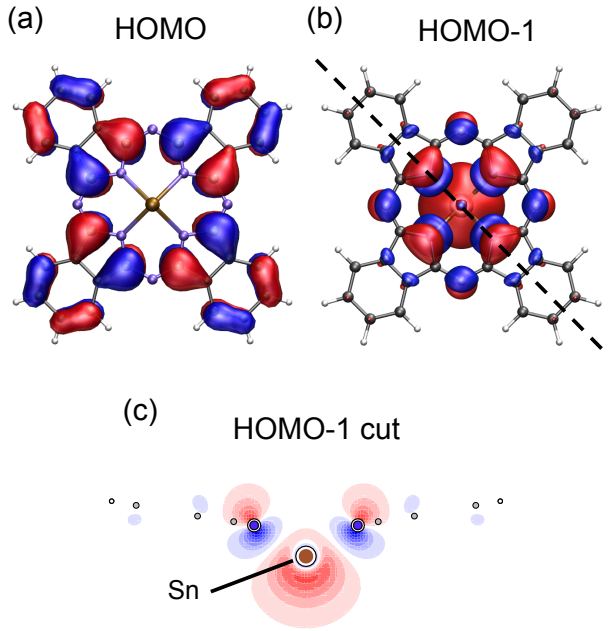

Figure 5.7: The upper two pictures show a top view of the "tin-down" conformation of SnPc for the HOMO in (a) and the HOMO-1 in (b). (c) shows a cut through the HOMO-1 ("tin-down") in the vertical plane indicated by the dashed line in (b). The prominent Sn p_z-contribution to the HOMO-1 can be seen. The negative part of the p_z-orbital above the Sn-atom is missing due to the hybridization with the s-orbital localized on the same atom.

modulation is superimposed on the 12 maxima. At lower polar angles ($\theta = 25°$) (label β) three bright maxima appear, partly intersected by a sharp ring-like artifact from the incomplete background subtraction. At normal emission a pronounced peak appears.
Figure 5.8(c) shows the best fit that could be achieved with SSC simulations for emission from the HOMO-1, excited with He I_α radiation. Due to the large Sn p_z contribution to the HOMO-1, the emitter is approximated by a p_z-orbital centered at the Sn atom. Later this fact will be discussed in more detail (see chapter 5.6). In the resulting SSC pattern the maximum in normal emission as well as the three bright maxima at $\theta = 25°$ (label δ) are well reproduced. Moreover, the figure shows that the three-fold symmetry of the substrate clearly dominates over the 12-fold symmetry expected from intramolecular scattering from a four-fold symmetric molecule adsorbed in three coexisting orientations. This is in clear contrast to the XPD case. An SSC simulation of a SnPc molecule without substrate is shown in Fig. 5.8(d), yielding 12 equally intense maxima after three-fold averaging. The superimposed three-fold symmetry in Fig. 5.8 (c) can thus be attributed to backscattering of photoelectrons from substrate atoms in the vicinity of the molecule, which is more pronounced for low-kinetic energy electrons. (*cf.* Fig. 2.5). It is remarkable that this three-fold symmetry persists even after averaging over 20 inequivalent adsorbate positions within the Ag(111) surface unit cell.
Comparing the experimental UPD pattern and the SSC simulation in Figs. 5.8 (b) and (c), respectively, reveals that the simulations slightly overestimate the amount of backscattering as the relative intensity of the bright inner features vs. the 12 outer maxima is higher in the simulated pattern. This is also confirmed by a comparison of the anisotropy for the outer (label α) and

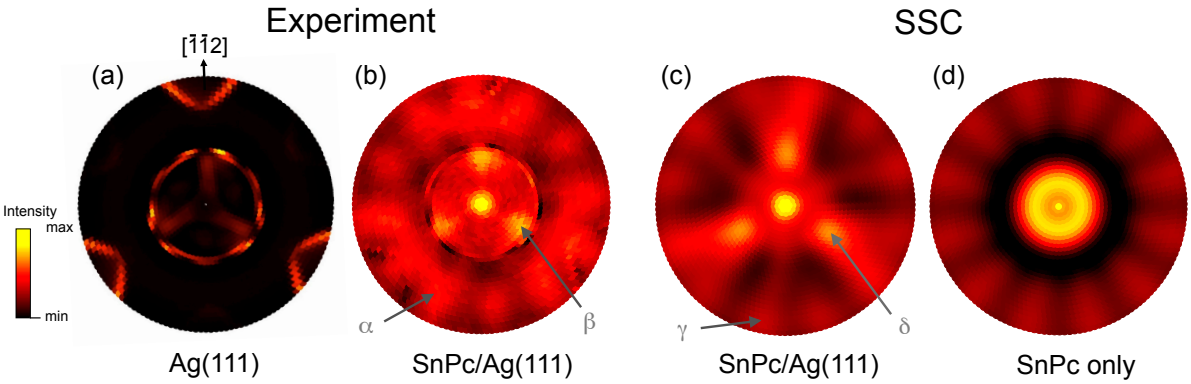

Figure 5.8: UPD measurements and corresponding SSC calculations. (a) Experimental angular intensity map for the energy region $E_B = 2.3$ eV from a clean Ag(111) substrate, serving as a reference for the anisotropies in the spectral background; (b) UPD measurement of the HOMO-1 of a 0.9 ML film of SnPc on Ag(111), with the background anisotropy removed as much as possible. Additionally a Gaussian shaped background was subtracted. (c) Average pattern of 20 three-fold symmetrized SSC simulations of a cluster containing the atoms of the SnPc molecule and 2 layers of Ag(111). Each of the 20 simulations result from a cluster where the molecule is adsorbed on a different lateral adsorption site (see text). (d) SSC simulation of a SnPc molecule in the adsorbed geometry without the Ag substrate. All plots cover a polar angle range going from normal emission ($\theta = 0°$, center of the plot) to $\theta_{\max} = 60°$ (outer rim).

inner (label β) maxima in the measured UPD pattern and in the simulated UPD (label γ *vs.* δ), respectively. Table 5.1 shows that the ratio between the anisotropies of the outer and inner maxima is smaller for the calculated than for the measured data.

	Experimental	Calculated
Outer max.	A(α)=0.13	A(γ)=0.07
Inner max.	A(β)=0.15	A(δ)=0.13

Table 5.1: Anisotropies for selected outer and inner maxima (*cf.* labels in Fig. 5.8) in the experimental and in the calculated UPD pattern, respectively.

The 12 outer maxima, which are due to intramolecular scattering in the SnPc backbone, appear at similar polar angles in both simulation ($\theta = 54°$, labeled δ) and experiment ($\theta = 50°$, labeled β). This slight inward shift of the experimental pattern with respect to the SSC simulation for the flat SnPc backbone is consistent with the result from the XPD analysis and might indicate that a slight bending of the molecule into a shuttlecock conformation persists in the adsorbed state.
Having clearly established the contribution of backscattering to the formation of the UPD pattern, one would like to explore its sensitivity to the bond distance of the molecule from the substrate. This was realized by including the first two layers of Ag atoms in the cluster and varying the vertical distance between molecule and top Ag layer. The best fit [Fig. 5.8 (c)] was achieved

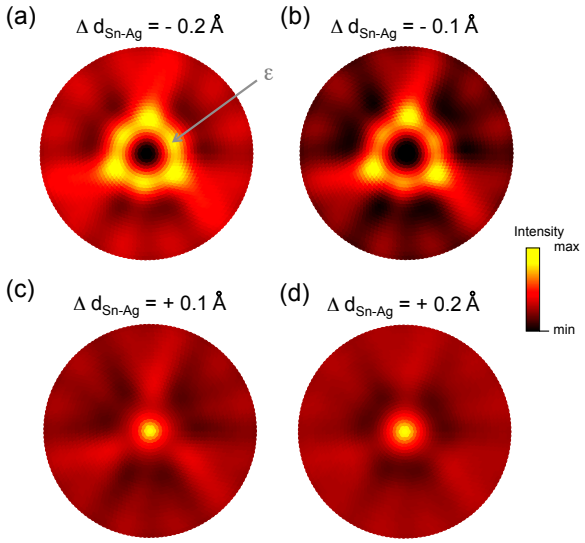

Figure 5.9: SSC simulations of the HOMO-1 UPD pattern using a p_z-type emitter for different molecule-substrate distances with distance offsets $\Delta d_{\text{Sn-Ag}}$ referenced to the best fit distance $d_{\text{Sn-Ag}} = 2.30$ Å. The polar angle range goes from $\theta = 0°$(center of plots) to $\theta_{\text{max}} = 60°$ (outer border of plots).

with very similar structural parameters ($d_{\text{Sn-Ag}} = 2.30$ Å, $d_{\text{C-Ag}} = 3.09$ Å) as used in the XPD simulations.

To account for the incommensurate superstructure, the same grid with 20 different adsorption sites of the SnPc molecules on the Ag unit cell was used as already mentioned in section 5.3. A three-fold average was carried out to account for the three rotational Ag(111) domains.

Figure 5.9 shows a series of SSC patterns for the HOMO-1 emission in which the distance between molecules and substrate $d_{\text{Sn-Ag}}$ was varied. In Fig. 5.9 (a) the distance between SnPc and substrate is the smallest, three additional spots appear in-between the three inner maxima (label ε). These spots gradually vanish as the molecule is moved further away from the Ag surface (see Figs. 5.9 (b) through (d)). In the case of the best fit with $d_{\text{Sn-Ag}} = 2.30$ Å (see Fig. 5.8 (c)) both, the three maxima at $\theta = 25°$ and the additionally appearing maximum at normal emission are strong. Upon further increasing the molecule-substrate distance the three-fold symmetric fingerprint of the substrate declines while the emission normal to the surface becomes stronger. On a scale of sub-angstrom distance variations the UPD pattern changes significantly, which makes such measurements a very sensitive probe for structural changes. The molecule-substrate distance determined from the best fit is in good agreement with the XSW measurements by Stadler *et al.*[75]

Simulating UPD patterns is generally more challenging than the XPD case for mainly three reasons: (i) the non-spherical and hybridized character of the initial state wave functions, (ii) the non-local character of molecular orbital states leading to coherent photoemission from multiple atoms within the same molecule, and (iii) the lack of an accurate description of the scattering potentials as well as the inner potential V_0 within molecular layers. These issues complicate the calculation of photoemission matrix elements and scattering phase shifts for the photoelectrons. Only just recently have these issues been addressed in the literature [71]. In this chapter issues (i) and (iii) were tackled partly.

It is obvious that the approximation of the HOMO-1 as a p_z orbital localized on the Sn atom is a crude one. A next better approximation would be an *sp*-hybridized orbital, and then the full molecular orbital as depicted in Fig. 5.7. Moreover, the HOMO-1 likely plays an important role in the chemisorption process between the first monolayer of molecules and the silver substrate [75, 77]. Charge donation and back-donation can lead to a change in the spatial distribution of the HOMO-1, as it was recently suggested based on DFT calculations with a semi-empirical dispersion correction [77]. The good agreement of the single scattering calculations assuming a p_z-emission with the experimental data (Figs. 5.8 (b) and (c)) suggests that the p_z-orbital character of the HOMO-1 remains dominant and largely unchanged upon adsorption. This statement is also supported by performed DFT calculations using the TORBOMOLE code [82].
With a work function of $\phi = 4.4$ eV [88], the kinetic energy of photoelectrons from the HOMO-1 in vacuum is $E_{kin} = 14.6$ eV when excited with He I_α radiation. Due to calculations with the self-consistent LMTO approach the inner potential, which is required for the calculation of phase shifts for scattering inside the solid, was assumed to be $V_0 = 8.7$ eV for SnPc/Ag(111) [90]. In the present case V_0^{eff} is introduced instead of V_0. It is used as a fitting parameter as electrons from the top-most molecular layer do not experience the same inner potential as those inside the solid. The best fit of the SSC results to the experimental UPD pattern was achieved with $V_0^{\text{eff}} = 6.0$ eV. This procedure even enlarged the parameter space that had to be converged, which was already spanned by the geometrical degrees of freedom such as substrate-molecule distance and the molecule geometry itself. The analyzed XPD measurements and XSW data from the literature, however, provided a good starting point for the structural parameters.
In consideration of the discussed difficulties the presented SSC result in Fig. 5.8 (c) shows a remarkably good agreement with the measured pattern.

5.5 Summary

The system SnPc/Ag(111) with a coverage of 0.9 ML of SnPc was examined with XPD and UPD measurements. From the XPD analysis, supported by SSC calculations, the conformation of the SnPc molecules on Ag(111) could be determined. The slightly shuttlecock shaped molecule experiences a flattening, while the Sn atom sticking out beneath the molecular plane moves a little closer. Furthermore, comparing SSC calculations and experimental data for both, Sn $3d_{5/2}$ and Ag $3d_{5/2}$, it is found that the diagonal vertical mirror plane σ_v^d of SnPc aligns with the Ag(111) unit cell vector, *i.e.* with dense rows of Ag atoms. These results confirm earlier findings [79, 84]. This knowledge was taken into account for the analysis of the UPD data from the same system. To simulate emission from a molecular state, *i. e.* the HOMO-1, the SSC code was adapted so that it can calculate photoelectron diffraction patterns also from non-spherically symmetric states, such as a p_z-state. Although the processes involved in forming a UPD pattern are far more complex than in the XPD case, a good agreement between SSC simulations and the recorded UPD data could be obtained for a molecule-substrate distance of $d_{Sn-Ag} = 2.30$ Å and $d_{C-Ag} = 3.09$ Å, again in good agreement with XSW data [75]. With a series of SSC calculations where the molecule-substrate distance was varied, it could be shown that UPD is a powerful method to detect structural changes of surfaces on a sub-Ångstrom scale. The sensitivity of the analysis to the parameter d_{Sn-Ag} results from strong backscattering contributions from Ag atoms which are essentially absent in the XPD case.
As photoelectrons emitted from a molecular monolayer experience another inner potential compared to those propagating in the bulk, also the inner potential was adjusted. A best fit was found

at a value of $V_0^{\text{eff}} = 6.0$ eV. The uncertainties of the inner potential, as well as the sensitivity of the calculated UPD patterns to even small changes in scattering phase shifts and photoemission matrix elements, demand an increased theoretical effort in the future, also including a multiple scattering treatment [26, 71].
The findings of this work are particularly encouraging in view of the increasing availability of ultrashort XUV laser pulses from HHG sources [55]. A pump-probe scheme becomes feasible where a molecular layer is excited by a strong infrared pump pulse and a subsequent XUV pulse is used for recording a UPD pattern to follow the structural evolution of the system as a function of the pump-probe delay, *i.e.* in the femtosecond regime. Processes involved in reversible molecular switches or in molecular desorption may become directly accessible to stroboscopic measurements.

5.6 SSC calculations for non isotropic initial states

The simulation of UPD patterns required a modification of the already existing SSC code to account at least partly for the molecular orbital character of the initial states. The code was extended so that it can calculate not only diffraction patterns for emission from completely filled core states with spherical symmetry, but also from anisotropic states with defined angular momentum and magnetic quantum numbers, *e. g.*, a p_z-orbital. As previously mentioned, the latter was used as emitter for the simulation of the UPD pattern in Fig. 5.8 (c). Calculations with emission from an s-state were also performed, but could not reproduce the features observed in the experimental data.
To show the validity of the extended code for scattering from non-isotropic emitters, a case with a simple emitter-scatterer configuration is presented in Fig. 5.10. The cluster consists of a Sn photoemitter and three carbon scatterers, one along each of the three Cartesian axes, as sketched in Fig. 5.10 (c). Diffraction patterns for emission from three orthogonal p-states (p_x, p_y and p_z) were then calculated. In Fig. 5.10 (a) the kinetic energy of the electrons was chosen as in the XPD experiment. In Fig. 5.10 (b) E_{kin} is assumed to be the same as in the UPD experiment. The experimental geometry, *i.e.* the direction of incident light and detection axis, were assumed to be the same as in the real UPD experiment for both examples in (a) and (b). The incident light is partially polarized and has contributions from s and p polarization.
In Fig. 5.10 (a) the higher kinetic electron energy facilitates the direct interpretation of the diffraction pattern. As expected the symmetry of the initial state greatly determines the outcome of the scattering: emission from a p_z-initial state shows a pronounced emission and forward scattering along the z-axis, *i. e.* in the normal emission direction (the center of the picture). Likewise emission from a p_x initial state shows a pronounced emission and forward scattering in the x-axis direction. It is thus demonstrated that the modified SSC code also accounts for non-spherically-symmetric emitters. Figure 5.10 (b) illustrates that an intuitive interpretation of UPD patterns is not possible. Due to large phase shifts and a complicated scattering character of the low-energy electrons the diffraction pattern depicts the scatterer and the initial state geometry only very vaguely.

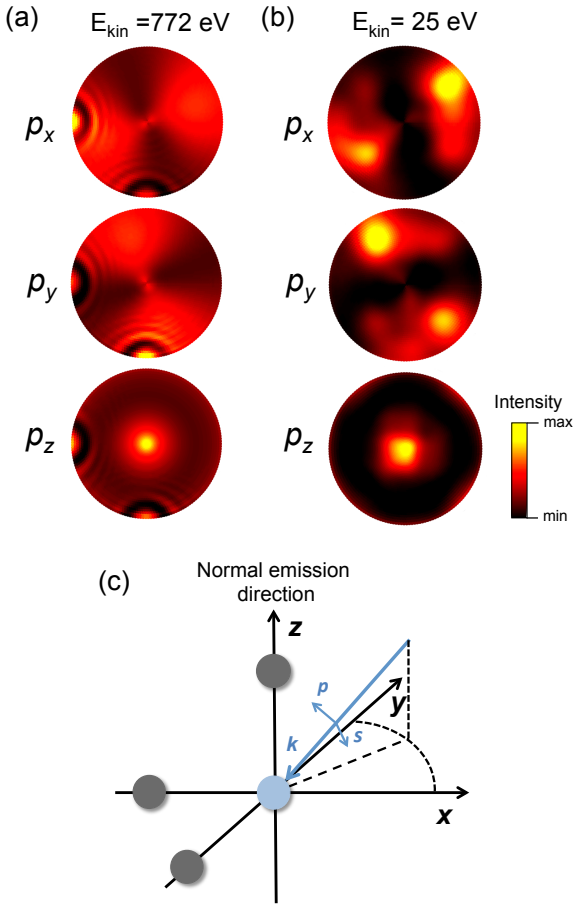

Figure 5.10: (a) SSC simulation of intensity patterns for emission from three orthogonal p-orbitals (E_{kin} = 772 eV in the solid). From top to bottom: p_x, p_y and p_z for the simple three-scatterer geometry depicted in (c). (b) SSC simulation as in (a) but with E_{kin} = 25 eV in the solid. The polar angle ranges from $\theta = 0°$ (center of the plots) to $\theta_{\max} = 86°$ (outer border of plots). (c) The corresponding three carbon scatterer geometry shown in a cartesian coordinate system. Situated in the coordinate origin is a Sn-emitter. The blue arrow indicates the direction of light incidence with s- and p-polarizations.

6 Time-resolved UPD on Bi(111) - A proof of principle study

In the previous chapter was shown, that UPD is a suitable method to resolve minute changes of the surface geometry. In the following we will present a proof of principle experiment for time-resolved UPD. In a pump-probe experiment coherent phonons were displacively excited in a Bi(111) crystal using intense IR pulses. With pulsed XUV photons oscillations in the electronic structure and oscillations in parts of a full UPD map were probed. Delay-dependent changes in the UPD signal could be assigned to a measurement of structural dynamics, which was underlined by SSC calculations. Changes of the electronic structure alone, as calculated with the tight binding model, could not explain the observed oscillation amplitudes. It is observed that the slower responding nuclear oscillation has a phase shift of π compared to the fast electronic response to IR excitation.

6.1 The system Bi(111)

The system of choice for such an experiment was a bismuth (111) crystal, the crystal structure of which has rhombohedral symmetry [91]. This symmetry is caused by a Peierls distortion along the [111] direction of a formerly cubic crystal lattice in order to minimize its energy [92]. The rhombohedral unit cell has a two-atomic basis as shown in Fig. 6.1. Its body diagonal is identical with the trigonal axis of the hexagonal unit cell with $c = 11.7967$Å. Due to the distortion the distances d_1 and d_2 are not equal but $d_1 = 0.467\,c$ and $d_2 = 0.533\,c$. This leads to a bilayer system in the [111] direction of the crystal (Fig. 6.1 (b)).
However the Peierls phase can easily be destabilized by photo-induced excitation of valence electrons into the conduction band, thereby creating a displacive excitation of coherent phonons (A_{1g} mode) along the [111] direction [93] (see Fig. 6.2 (a)). In that model hot electrons are created by absorption of IR photons and due to an anharmonic crystal potential, the altered charge distribution makes the rhombohedral crystal phase less favorable. As a consequence the lattice starts to oscillate around a new quasi equilibrium closer to the cubic lattice phase (Fig. 6.2 (b)). During the first few picoseconds after excitation the energy is largely stored in the electronic excitation and the A_{1g} mode [94, 95].
By x-ray diffraction measurements combined with DFT calculations, it was quantitatively demonstrated, how lattice spacing and frequency of the phonons depend on the fluence of the IR pulse [94]. The authors of that work define a normalized equilibrium coordinate $x = 0.5 + \delta$ around which the phonon amplitude oscillates. In the non excited state $x = 0.467$ (Fig. 6.1), for $x = 0.5$ the equilibrium of the oscillation would be the cubic phase. The value of x increases with higher

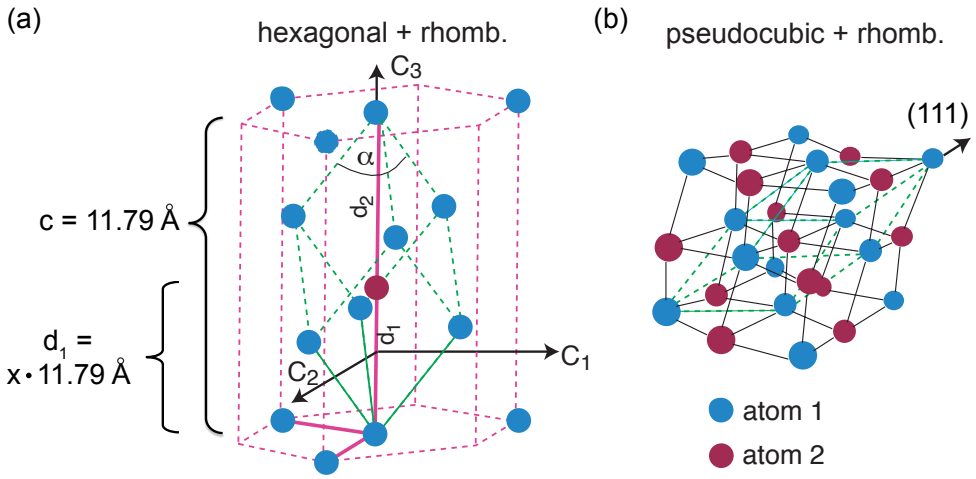

Figure 6.1: Bulk structure of Bi. (a) rhombohedral unit cell (dashed green lines) together with the hexagonal unit cell (dashed pink lines). Not all the atoms are shown. Blue and red colors mark the two atoms in the rhombohedral unit cell. The solid green and pink lines are the vectors spanning the rhombohedral and hexagonal lattice, respectively. The three orthogonal axes are: bisectrix (C1, y), binary (C2, x) and trigonal axis (C3, z). The distance d_1 can be expressed by the equilibrium coordinate x (non excited: $x = 0.467$). (b) Illustration of the pseudocubic character of the structure together with the rhombohedral unit cell. The [111] direction is indicated. A bilayer system becomes visible. Each bilayer consists of one layer with red and one with blue atoms. Figure after [91].

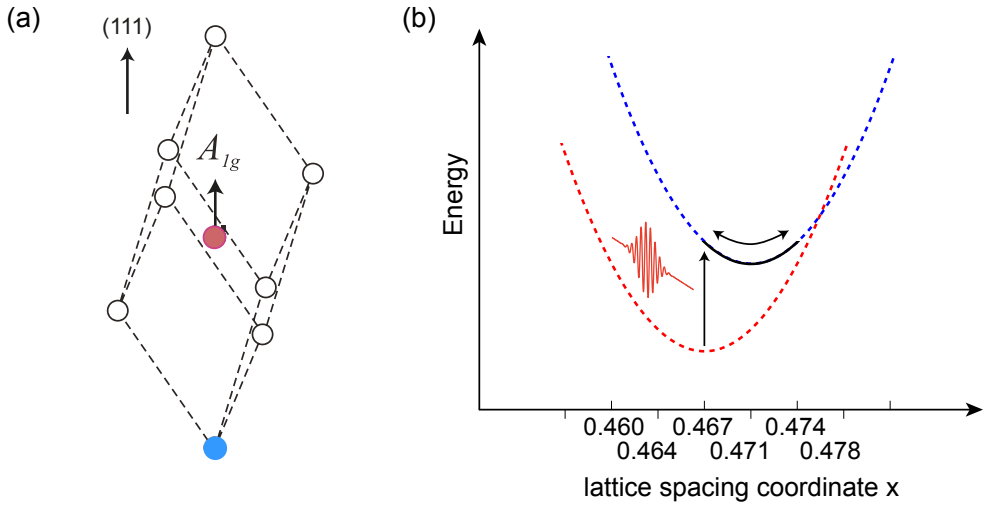

Figure 6.2: (a) Direction of the A_{1g} amplitude. (b) Cut through the potential surface of Bi(111): Before excitation the potential surface is described by the dashed red curve. After excitation the potential is shifted to a new quasi-equilibrium (dashed blue curve). The solid black curve indicates the estimated amplitude of the lattice oscillation. The x values of the excited state give an upper limit estimated after [94] assuming a fluence of $F = 1.4\ \frac{\mathrm{mJ}}{\mathrm{cm}^2}$.

fluence and a phonon softening occurs, *i. e.* the A_{1g} frequency is reduced. Additionally both effects can be derived by a comprehensive model applying the Landau expansion of the free energy of the lattice. Solving the equation of motion and deriving the corresponding frequency shows that the displacement as well as the phonon softening depend linearly on the amount of electrons promoted to the conduction band, in case of low excitation densities [95]. The linear frequency dependence was also found in reflectivity experiments [96]. At strong IR fields ($F = 6.7\,\frac{\mathrm{mJ}}{\mathrm{cm}^2}$) a low frequency of $\nu = 2.12$ THz can be reached, while the unperturbed crystal oscillates at $\nu = 2.92$ THz [9].
Reflectivity measurements furthermore show cosine-like oscillations due to phonon excitation, *i. e.* the oscillations start close to the maximum reflectivity at delay $\Delta t = 0$ ps [97]. The change in reflectivity is mainly caused by an electronic response, therefore it was suggested that the electronic displacement is sudden. It was also found that the phonon frequency is chirped and goes to larger values as the excitation relaxes and the oscillation amplitude becomes smaller [98].
With intense enough exciting fields ($F = 20\,\frac{mJ}{cm^2}$) displacements of more then 10% of the ground state lattice spacing could be reached [9]. This is just where the crystal is fully driven into the cubic phase. In this regime the Lindeman criterion is reached, which postulates a solid-to-liquid phase transition at so strong displacements. Indeed indications for lattice melting could be observed.
A detailed view on the consequences of the phonon oscillation for the valence band structure, was obtained in two color pump-probe experiments [99, 100]: After an initial shift to larger binding energies of both the bulk and the surface states, only the energy position of the bulk states as well as their intensity oscillate cosine-like, while the surface states do not oscillate.
At the Attoline beamline at ETH Zurich, it was also possible to do a pump-probe experiment using intense IR pulses as pump and pulsed XUV light as probe pulses. As the energy of the XUV pulses can be tuned up to 70 eV it is not only possible to probe the valence states of bismuth, but also its shallow 5d core levels that are located at $E_B = 23.8$ eV and 26.9 eV, respectively. In that way it becomes feasible to excite the coherent phonons with the IR light and, changing the delay between the two pulses, to record time-resolved diffraction patterns either from the valence band or from the 5d core levels.

6.2 Experimental preparations

The preparation procedure for the Bi(111) crystal was repeated on a daily routine. Two cycles of sputtering with Ar ions of $E_{kin} = 550$ eV for 30 min were each followed by annealing for 5 min at $T = 150°$ C. To check the cleanliness of the crystal, XPS survey spectra as well as Bi Fermi surface maps were recorded.
On the laser side the photon spectrum had to be tailored every day. First the energy spectrum was adjusted by the means explained in chapter 3.2: Pressure inside the gas target, position of the gas target and iris settings were optimized to always reproduce the same spectrum. Once the XUV spectrum recorded with the XUV spectrometer showed the right characteristics, the light was sent to the surface. As it was possible that the beam path of the laser pulses slightly changed from day to day, the proper sample position of the crystal had to be found by recording a series of energy dispersion curves.
Prior to starting the experiment, spectra with excitation from both IR and XUV pulses combined were recorded. In that way too strong space charge effects or above threshold photoemission could be avoided.

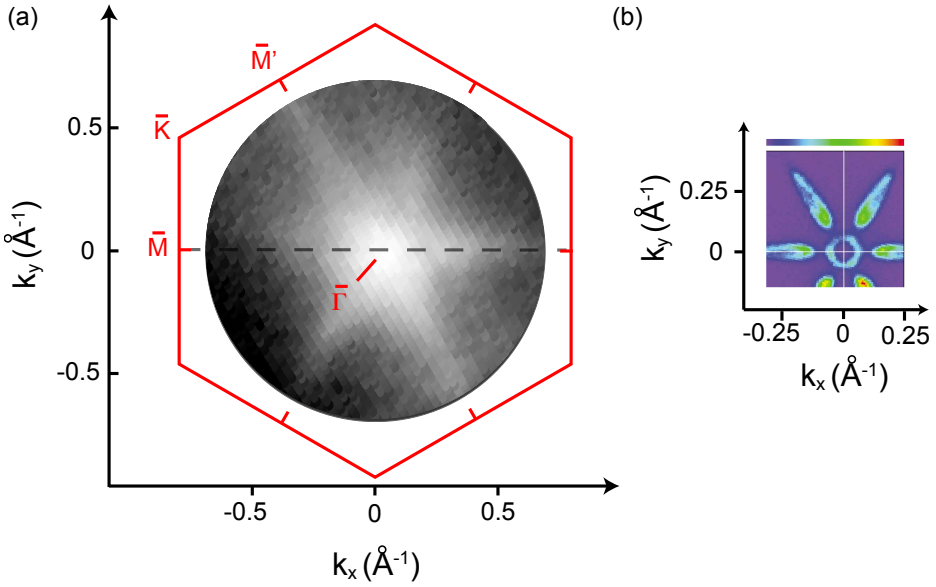

Figure 6.3: (a) Fermi surface map of Bi(111) recorded with He I_α at $T = 300$ K. The first Brillouin zone and its high symmetry points are marked in red, with a distance of 0.80 $Å^{-1}$ between $\bar{\Gamma}$ and $\bar{M}$. By the dashed line the $\bar{\Gamma}\bar{M}$ direction of the reciprocal lattice is shown, which was parallel to the angular axis of the detector. (b) Fermi surface map from literature, recorded with $h\nu = 18$ eV at $T = 50K$ [101].

6.3 Coherent phonons with pulsed XUV light

Since the oscillations of electronic structure caused by the phonon oscillations were not yet observed with HHG light, a pump-probe measurement at normal emission was conducted, recording the time evolution of the valence band as a first step. With the WAL detector energy, polar angle and time delay were scanned. In order to align the crystal properly the bismuth Fermi surface map was recorded using the He I_α line as shown in Fig. 6.3 (a). The crystal was azimuthally oriented so that the angular axis of the detector was parallel to the $\bar{\Gamma}\bar{M}$ direction of the Brillouin zone. The observed features of the Fermi surface map are relatively broad compared to measurements known from literature (Fig. 6.3 (b)). With a very low surface Debye temperature of $\theta_D = 48$ K, a significant broadening of the features is expected, if the measurement is conducted at room temperature as it was the case here. Furthermore the line width of the light source and the angular resolution in the present measurement lead to broader features compared to the work in [101]. Still the six lobes spaced by $\phi = 60°$ are visible, which is sufficient to properly align the sample.

For the delay scan the XUV photon signal shown in Fig. 6.4 (a) was used. While it would have been desirable to generate a monochromatic spectrum, it was only possible to reduce the spectrum to the minimum of two dominant harmonics in the Attoline setup. The duration of the XUV pulse trains was $\Delta t \approx 11$ fs, while the IR pulse was $\Delta t \approx 22$ fs.

Note that there is a filter in the beam path before the XUV pulses are detected in the photon spectrometer. This filter has a transmission function $T(E)$, that is not exactly known but it changes the ratio between higher harmonics 13 and 15 at $E = 20.4$ eV and $E = 23.5$ eV such that the one with lower photon energy appears less intense than it is in reality. This is also evident in

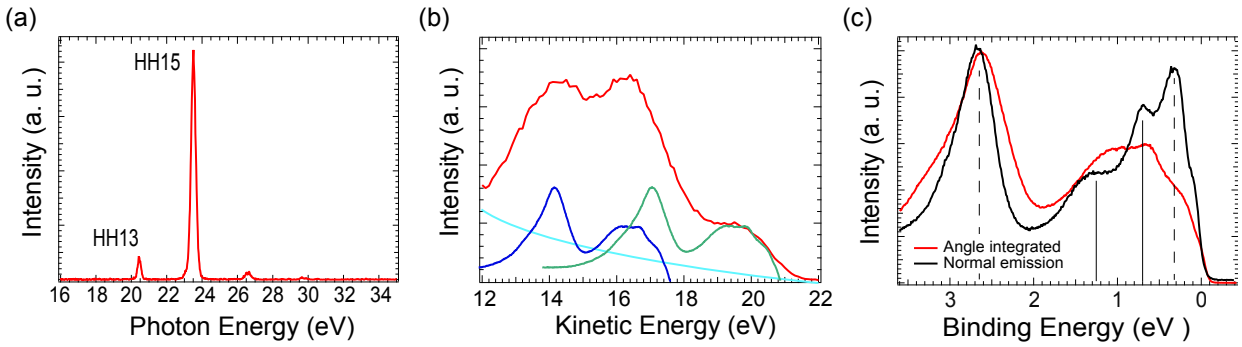

Figure 6.4: (a) Photon spectrum of the XUV pulse from the Attoline. The spectrum is not corrected for the unknown transmission function of the filter in front of the spectrometer. Higher harmonic (HH) 13 at $h\nu = 20.4$ eV is therefore underestimated compared to HH 15 at $h\nu = 23.5$ eV. The peaks on the right corresponding to HH 17 and 19 are weak and have nearly no influence on the spectra from the surface. The pulse duration of the XUV pulse is $\Delta t \approx 11$ fs. (b) Valence band from Bi(111) recorded with the XUV spectrum from the Attoline (red curve). A polar angle range of $\pm 27°$ was integrated. The three peaks mainly stem from a superposition of two replica from the valence band due to the two harmonics, as indicated by the blue and green curves as guides to the eye. The bright blue curve shows an estimated exponential background. (c) Valence band recorded with He I_α at normal emission (black) and $\pm 27°$ angle integrated (red). The solid lines denote bulk states and the dashed lines surface derived states.

the valence band spectrum of Bi(111) in Fig. 6.4 (b). which shows the spectrum recorded with XUV pulses. Space charge effects lead to a broadening of the spectrum and to higher energies of the fastest electrons, so that the Fermi edge corresponding to electrons excited by harmonic 15 appears at $E_{kin} = 20.6$ eV. Figure 6.4 (c) shows the angle integrated valence band spectrum and the one at normal emission resulting from excitation with He I_α emission. In the angle integrated spectrum the bulk states (solid lines) are more prominent compared to the spectrum at normal emission, where the surface state (dashed line) at 0.3 eV is dominant. The state at 2.5 eV has contributions from both bulk and surface resonance states [102, 103].
In the delay scan the valence band was then recorded in the range of $E_{kin} = 18$ eV - 24.5 eV. With the wide angle lens an angular range of $\theta = \pm 27°$ was recorded but to show the behavior at normal emission, only polar angles of $\Delta\theta = \pm 5°$ around normal emission were integrated for better signal statistics. (The full angular range will be considered later in chapter 6.7.)
Figures 6.5 (a) and (b) show the result of the delay scan: At negative delays, where the XUV pulses arrive prior to the IR, there is no oscillation visible. At delay $\Delta t = 0$ fs, when the pulses overlap, a strong increase in intensity is visible. This increase can be attributed to the excitation of hot electrons. For positive delays the intensity oscillates with a cosine-like character, as known from literature [48]. The oscillations becomes better visible in Fig. 6.5 (b) that shows the energy integrated signal of (a) inside the red bars. The curve is normalized by the Ar-gas phase signal shown in Fig. 6.5 (d). The gas phase signal was simultaneously recorded using the same XUV pulse as for the emission from the Bi crystal. That way laser fluctuations are partially compensated for.
To determine the frequency of the phonon oscillation the signal of Fig. 6.5 (b) was fitted with an exponentially damped harmonic oscillation. The resulting frequency from the fit is $\nu = (2.71 \pm$

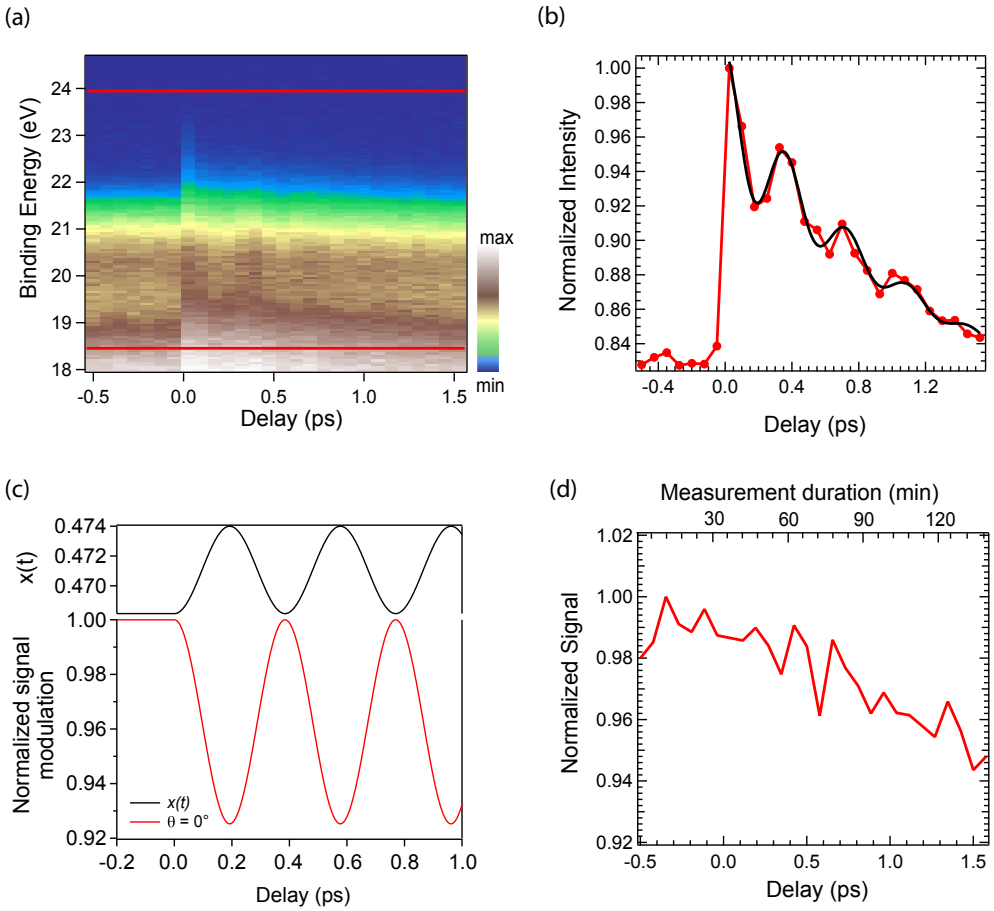

Figure 6.5: (a) Delay scan of the Bi(111) valence band. A polar range of ±5° around normal emission was integrated. The photon signal from Fig. 6.4 (a) was used. For positive delays the intensity oscillations are visible. (b) The energy integrated delay scan (red) normalized by the Ar-gas scan in (d). The integration range is indicated by the red bars in (a) from 18.5 eV to 24 eV. An exponentially damped cosine function is fitted to the data (black curve) with frequency $\nu = (2.71 \pm 0.06)$ THz. (c) shows the calculated change of the signal that is probed at normal emission depending on the lattice distortion as expressed by the coordinate $x(t)$. The curves were generated using tight binding calculations. (d) Energy integrated photoemission yield from an argon gas-jet recorded at the corresponding delay. This scan was simultaneously recorded with the same XUV spectrum and was used to normalize the data in (b) in order to correct for the XUV fluctuations.

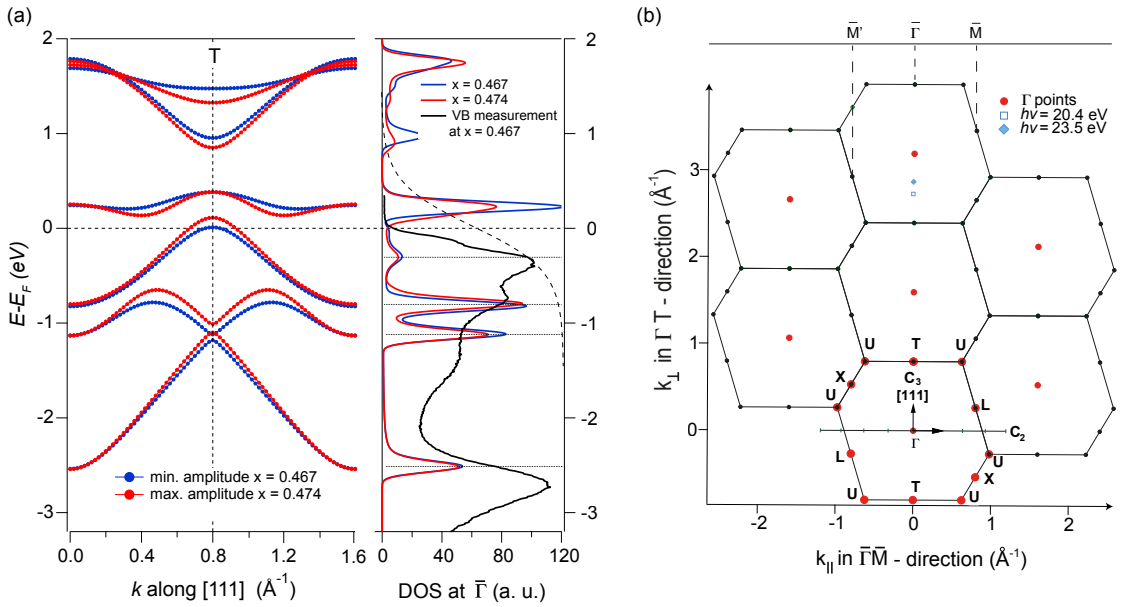

Figure 6.6: (a) Band structure calculation and DOS around E_F. *Left:* Within the tight binding model the various energy bands $E(\boldsymbol{k})$ of Bi(111) were calculated from the Γ point along the [111] direction in the valence regime. Blue indicates the dispersion for minimum amplitude of the oscillation which is equivalent to the unexcited lattice structure. Red indicates the dispersion of the maximum amplitude. *Right:* The energy dependent partial DOS in the valence regime is plotted for the maximum and the minimum amplitude. Additionally the measured valence band structure with He I_α excitation at normal emission (solid black) and a Fermi-Dirac distribution function at $T = 2000$ K (dashed black) are plotted in the graph. (b) View on the Brillouin zones in the reciprocal space. A cut along the ΓT - $\bar{\Gamma}\bar{\mathrm{M}}$ plane is presented. The blue diamond and square indicate the k-vector of the final state electrons emitted by the respective light source with $h\nu = 23.5$ eV or $h\nu = 20.4$ eV.

0.06) THz corresponding to a time period of $T = (369 \pm 8)$ fs. The IR fluence during the delay scan was $F = (1.26 \pm 0.25)\,\frac{\mathrm{mJ}}{\mathrm{cm}^2}$. The error of the fluence results mainly from the uncertainty of the beam area on the sample. The phonon frequency from fluence-dependent studies in [94] ($\nu \approx 2.74$ THz) is within the range of the error bar of the determined frequency from the cosine-fit. The life time of the excited electrons determined by the decay of an exponential function fitted to the oscillation in Fig. 6.5 (b) gives $\tau = (1.03 \pm 0.44)$ ps, which is short compared to values in [99]. Reasons might on the one hand be the use of lower fluences in [99] compared to the present work and on the other hand the normalization of the measured signal with the Ar-gas phase, that is done here, cannot correct for fluctuations from both light sources IR and XUV. This can lead to faster decays of the signal. It is important to note that measured fluctuations in the XUV spectrum imply fluctuations in the IR pulses, too, since the XUV is generated from the IR. The HHG-process is not a linear process and the IR pulses could not be measured with the TOF signal but they contribute to the strength of the background signal from the surface. Furthermore it is not clear whether the detector linearity with respect to the electron intensity is of the same quality for TOF and WAL analyzer. Thus not all artifacts due to intensity fluctuations of the light source could be corrected for by normalization with the gas phase signal.
The cosine-like shape of the oscillation is explained as follows: The electronic states respond very

fast to the excitation by the IR and hot electrons are almost immediately excited. The altered charge distribution kick starts coherent phonon oscillations. In turn the electronic structure, represented by the density of states (DOS) depends on the electric field generated by the atomic cores inside the crystal. Hence the DOS changes with the positions of the atoms. Thus an interplay between atomic positions and electron density is established. When the lattice symmetry approaches the cubic phase, the DOS around E_F is reduced in the region close to normal emission. Therefore largest intensities occur at smallest distortion amplitudes, when the lattice is closest to the unexcited state [96, 98, 99].
As shown in Fig. 6.5 (c), these findings are underlined by simulating the distortion dependent intensity of the electronic states around E_F with band structure calculations (for details see below). No damping or relaxation was included in the delay dependent calculation. It can be observed that the oscillation amplitude of experiment and calculation are 8% and 7.5%, respectively, with respect to the total signal and therefore agree well. This agreement poses a good validity check regarding the quality of the used parameters for the calculation. The model was a tight binding approach after Liu and Allen [104].
In a first step the band structure of the Bi(111) crystal was calculated over the full height of the Brillouin zone along the ΓT direction. Second, a partial DOS $D(\boldsymbol{k})$ was generated from the band dispersion using the relation

$$D(\boldsymbol{k}) \propto (\nabla_{\boldsymbol{k}} E(\boldsymbol{k}))^{-1}. \tag{6.1}$$

The results for the two extremes of minimum and maximum phonon amplitude are shown in Fig. 6.6 (a). The left graph shows the band dispersion and the right shows the dispersion derived partial DOS around E_F. Since the measurement probed states at normal emission, $(\nabla_{\boldsymbol{k}} E(\boldsymbol{k}))^{-1}$ was only evaluated at each calculated point along the ΓT direction of the Brillouin zone. The contributions over the full height of the Brillouin zone were summed up to generate the partial DOS at $\bar{\Gamma}$.
For simplicity reasons the term "partial" will be dropped from here on. The reader should bear in mind that the DOS is always only evaluated along the [111] direction, *i. e.* the direction along which $\boldsymbol{k}$ is integrated, due to energy integration. Fig. 6.6 (b) presents an overview on the bulk Brillouin zones of the Bi crystal lattice.
One can see that the lattice at minimal phonon amplitude, which is equivalent to the non excited Bi crystal, has a larger DOS around E_F than in case of maximum amplitude. To generate an estimate of the electron intensity as used in Fig. 6.5 (c) the DOS is summed up over the same range around E_F as the measured signal and then multiplied with a Fermi-Dirac distribution assuming an electronic temperature of $T = 2000$ K as was found in a work under similar conditions [19]. The integration range for the measured data was $E_{kin} = 18.5$ eV to $E_{kin} = 24$ eV, which corresponds to a range of $E - E_F = -2.5$ eV to 3 eV.
For comparison the experimental data of the Bi(111) valence band at normal emission from Fig. 6.4 (c) that were recorded with He I_α are also plotted in the right part of Fig. 6.6 (a). It shows that the calculation reproduces the energy positions of the bulk states with good accuracy. For the states measured at $E - E_F = -2.7$ eV, a hybridization of bulk states and surface resonance obscures the exact position of the bulk states. The main contributions to the calculated DOS originate from near the Γ point. Since the measured states have similar energy position mainly electrons near Γ are probed in the experiment.
Summarizing the delay scan measurement at normal emission demonstrated that the IR power was sufficient to excite the coherent phonon oscillations and that they could be resolved with the HHG pulses. Their origin can be understood by applying the model of displacive excitation of coherent phonons and density of states calculations.

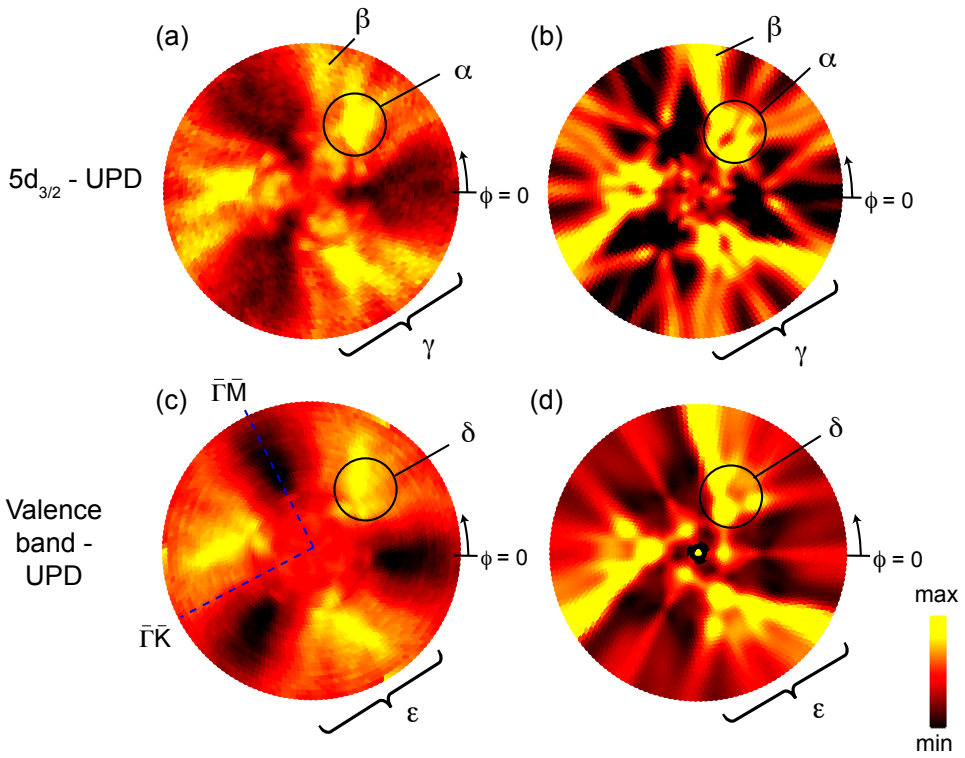

Figure 6.7: Comparison between measured UPD maps and maps calculated with SSC. In (a) a map of electrons from the $5d_{3/2}$ core level excited with He II_α radiation is shown. (b) shows the simulation of (a) with SSC. Specific features like the highest intensity (α) or the strong intensity at large polar angles (β) are marked. The UPD map for valence band emission integrated over the whole energy region of the band is presented in (c) Also the two high symmetry directions of the surface Brillouin zone $\bar{\Gamma}\bar{K}$ and $\bar{\Gamma}\bar{M}$ are indicated. The used light source was He I_α. Again the measurement is compared to SSC simulations (d). Also here the region with highest intensity (δ) and the "finger-like" features (ε) are marked.

6.4 UPD from Bi(111) in equilibrium

Prior to a time-resolved UPD experiment, diffraction maps of the crystal lattice in equilibrium were recorded with the He discharge lamp in the ESCA laboratory at University of Zurich (see chapter 5.2). These measurements serve as a reference to check the quality of the SSC simulations. The simulations can then be extended to calculate UPD patterns in the WALküre geometry. The photon energies at the Attoline, as they are used for a time-resolved experiment, are slightly different compared to the He emission lines. Also the line widths of the respective harmonics are broader than the He lines. But as well for valence band as for 5d core level emission, harmonics can be found with an energy close to that of the He I_α or the He II_α line respectively. So the final states and the scattering behavior should be comparable for both light sources. Another difference between UPD measurements at the ESCA laboratory and at the Attoline is the incidence angle of the beam, which leads to different intensity distributions due to matrix element effects. This can be accounted for in the scattering simulations, however. The UPD map of the bismuth $5d_{3/2}$ core level recorded with He II_α ($h\nu = 40.8$ eV) is presented in Fig. 6.7 (a) and the corresponding

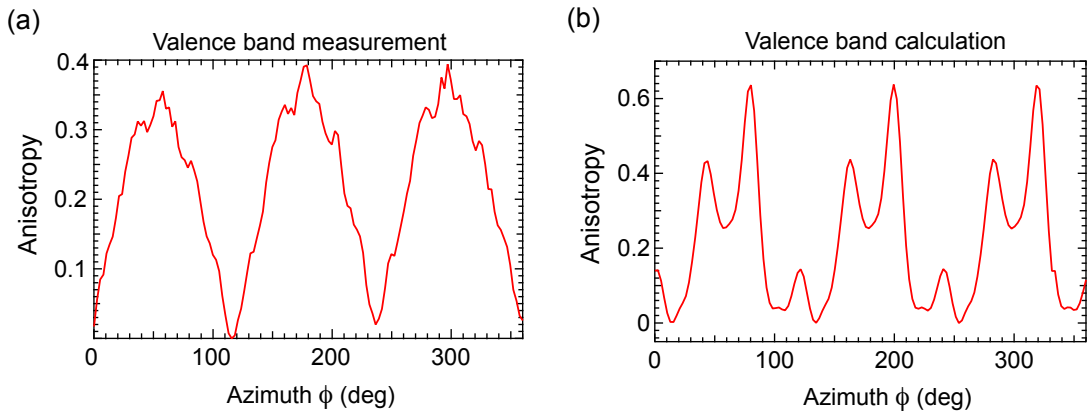

Figure 6.8: Azimuthal cut of the valence band UPD at $\theta = 50°$. The anisotropy (for definition see chapter 5) of the cut through the measured diffractogram (a) and through the simulated one (b) are shown.

SSC simulation is shown in (b).
In the case of electrons with low kinetic energies $E_{kin} < 50$ eV high accuracy of scattering phase shifts and amplitudes is required, due to the complex scattering behavior. Thus SSC calculations in that energy regime are less precise as those for faster electrons. In that light the similarity between experiment and SSC calculation in (a) and (b) is acceptable. Moreover many main features of the maps are qualitatively reproduced, such as the strongest intensities at about $\theta = 50°$ that appear every 120° (annotated as α). Also the "finger-like" features γ that run out from the high intensity areas to larger polar angles, the outer left of which is strongest in intensity (β), appear in both experiment and simulation. Alas the shape of the main maximum in α is not well reproduced. The simulations clearly show a local minimum that does not appear in the experiment.
In Fig. 6.7 (c), the complete valence band was probed and was integrated from $E_B = 5$ eV to E_F at each point on the hemisphere, using He I_α ($h\nu = 21.2$ eV) photons. When simulating UPD maps of valence states there is one additional difficulty at hand: Since valence states are not localized the emitter can not be described easily (see chapter 2.2.4). However in the case of copper valence states it was shown that for a full integration of the valence band the assumption of emitters localized at atomic sites can result in a very precise reproduction of the measured UPD pattern [23, 26]. The same approach is also used here for the SSC simulation of the Bi(111) UPD map from valence states (Fig. 6.7 (d)). SSC calculations for four equally spaced different binding energies in the valence band were added up. Indeed the quality of the simulation compared to the measurement is about the same as in the shallow core case. Also here the features (ε) at large polar angles are well reproduced. Compared to the core level UPD, the maxima in the valence band measurement coincide less well with the simulations, that show an even more pronounced local minimum (δ).
It is notable that the measurements from the 5d level and from the p-dominated valence band show a strong similarity. The kinetic energy of electrons excited with $h\nu = 40.8$ eV (He II_α) from the $5d_{3/2}$ states is approximately $E_{kin,s} = 25$ eV inside the solid. $E_{kin,s}$ of electrons from the valence band with a mean $E_B = 2.5$ eV are 1.7 eV faster, if probed with 21.2 eV (He I_α). Assuming final state scattering effects are dominant, the close values of the final state kinetic energy in the two experiments might be the reason for the similar UPD results.
In Fig. 6.8 azimuthal cuts at $\theta = 50°$ extracted from measurement and simulation are compared.

It can be seen that there are substantial differences in the both curves. Especially the three main maxima in Fig. 6.8 (a) appear as double peaks in (b). Furthermore the measurements in (a) do not show the small local maxima at $\phi = 0°, 120°, 240°$ that appear in the simulations (b).
MSC calculations using the EDAC code [67] were also tested. The results did not give results with better similarity to the experiments than those obtained with the SSC approach. Diffraction maps of electrons emitted from the 6p valence band of Bi could not be calculated using the EDAC code at all.

6.5 Time-resolved UPD

For the time-dependent measurements the focus was on the valence band, first as the overall anisotropy is larger and second no time dependent changes could be seen in the core state measurements. All time-resolved figures shown here were taken with the WAL in the Attoline-setup. In order to maximize the coherent phonon oscillation the IR fluence was increased to $F = (1.4 \pm 0.2)\frac{\text{mJ}}{\text{cm}^2}$ and the corresponding frequency was evaluated to be $\nu_{Ph} = (2.66 \pm 0.13)$ THz. A stronger increase leading to larger amplitudes was not possible due to space charge effects. From the work by Fritz *et al.* [94] the quasi-equilibrium coordinate at these values is estimated to be $x = 0.4705$ and the maximum amplitude of the lattice oscillation to be $\Delta x = 0.0035$. Expressed in absolute distances the maximum amplitude is $\Delta d_{\text{max}} = \pm 0.04$ Å, corresponding to 2.5 % of the nearest neighbor distance along the [111] direction. Using the different estimated lattice distortions as input to SSC calculations, the magnitude of the expected changes in the time-dependent diffraction signal could be simulated. For this purpose the geometric parameters of the WALküre chamber, the light polarization (p-polarization) and the different final state energy due to different photon energies were adjusted in the SSC calculation. For valence band emission the same photon spectrum as already used for the normal emission experiment in section 6.3 was applied.
Figure 6.9 (a) shows the SSC calculated UPD pattern for the quasi equilibrium state of the lattice. A measured XPD pattern in order to determine the crystal orientation is given in Fig. 6.9 (b). For maximum and minimum phonon amplitudes the full maps are not presented, as the differences compared to the map shown here are very small and can hardly be seen by eye. More instructive are the azimuthal cuts at $\theta = 50°$ in Fig. 6.10 (b). The cuts were taken from UPD simulations for 3 different lattice spacings: The quasi-equilibrium (intra-bilayer distance $d_{Bi} = 1.62$ Å), the minimum ($d_{Bi} = 1.58$ Å) and the maximum ($d_{Bi} = 1.66$ Å) spacing of the bilayer of a Bi(111) crystal. For the maximum amplitude, *i. e.* the largest intra-bilayer spacing, when the crystal is closest to the cubic phase, the intensities have a maximum nearly every where, while they have the minimum for the smallest intra-bilayer distance.
In chapter 4 it was demonstrated that recording diffraction maps with the WAL is about 10 times faster than with a conventional channeltron detector. However with the repetition rate of the Attoline of 1 kHz the photon flux compared to a constant light source like an x-ray gun or a He lamp is dramatically lower, which makes integration times much longer. This can only partially be compensated for by increasing the power of the laser up to the space charge limit. Another issue complicating the data acquisition were the fluctuations of the laser power. The day-to-day differences of the laser performance were large. Also during a single measurement, the fluctuations of the laser were significant and limited the duration of delay scans, again. Figure 6.11 (a) shows an energy integrated argon gas phase spectrum recorded with the TOF. It was used to normalize the time dependent angle scan and in that way minimize the effect of the fluctuating laser. Besides a drift to lower intensities the fluctuations on that day were relatively small. As mentioned in section 6.3 due to IR fluctuations and uncertainties of detector linearities not all fluctuations can

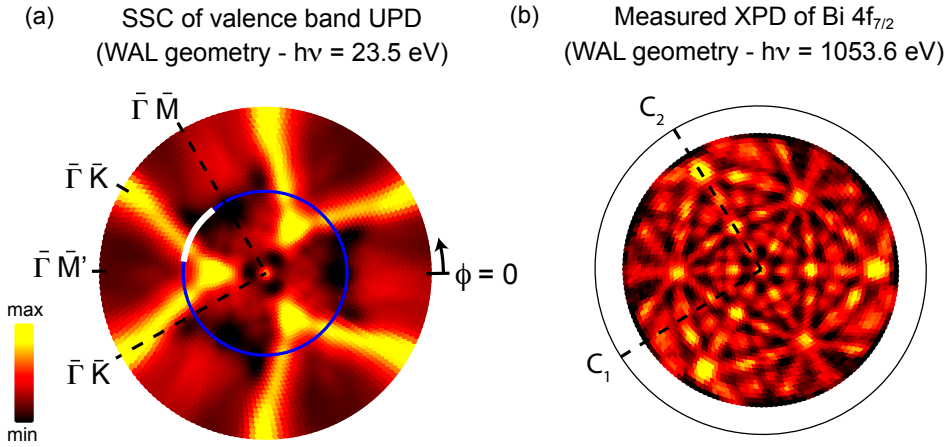

Figure 6.9: (a) SSC simulation of a UPD pattern from valence band electrons emitted with $h\nu = 23.5$ eV. The pattern is calculated for an excited lattice with a spacing given by the quasi-equilibrium coordinate $x = 0.4705$. The blue circle marks the azimuthal ring at a polar angle of $\theta = 50°$ and the white arc shows the azimuthal range which was recorded in the time-resolved scan. It crosses the $\bar{\Gamma}\bar{K}$ direction of the reciprocal lattice. Additionally $\bar{\Gamma}\bar{M}$ and $\bar{\Gamma}\bar{M}$' directions are indicated. (b) Measured XPD map of the Bi $4f_{5/2}$ peak excited with 1253.6 eV. The hexagonal axes C_1 and C_2 denote the crystal orientation. C_2 is directed along the mirror plane of the crystal. From the XPD map the orientation in reciprocal space can be deduced.

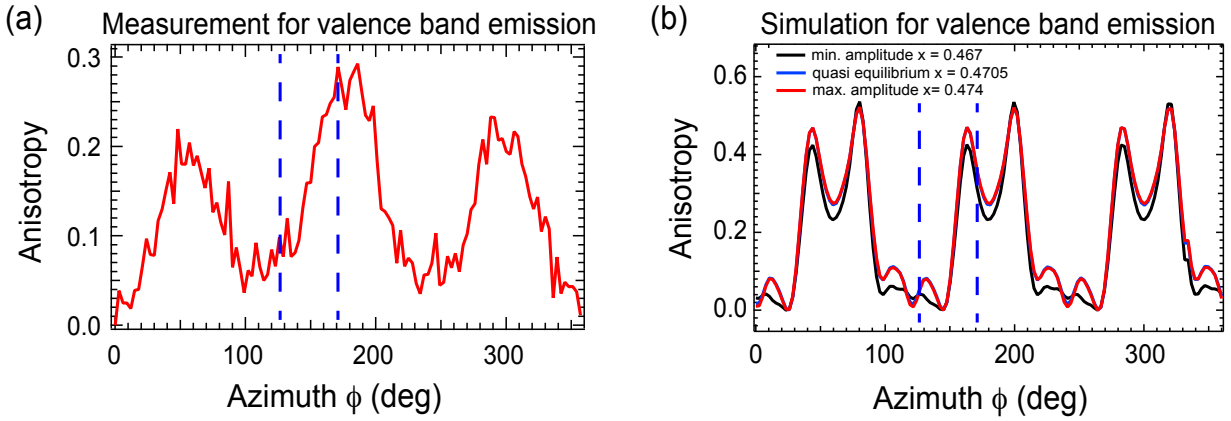

Figure 6.10: Azimuthal cut of valence band UPD in the WAL geometry with a photon energy $h\nu = 23.5$ eV. The measured azimuthal cut with HHG photons (a) and the corresponding SSC simulations (b) are shown. In (b) the azimuthal cuts of 3 different lattice spacings are simulated. Blue and red curve are very similar, so that the red curve mostly hides the blue curve. The dashed lines in both (a) and (b) indicate the azimuthal range that was recorded in the time resolved measurement.

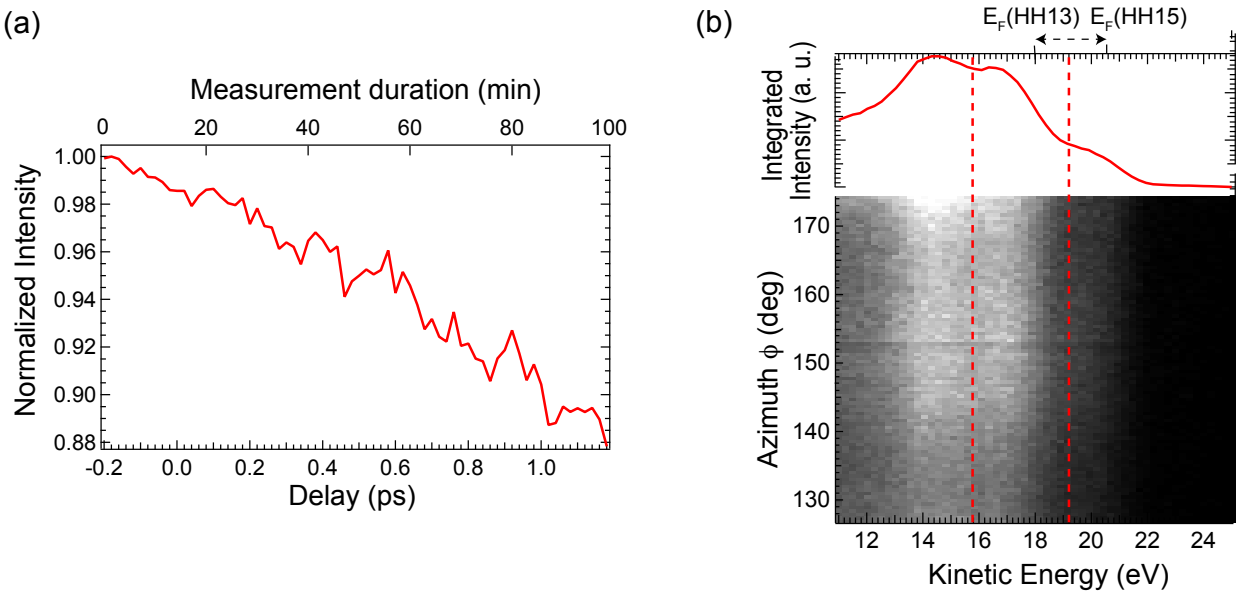

Figure 6.11: (a) Energy integrated photoemission yield from an argon gas-jet recorded at the corresponding delay. The photon signal shown in Fig. 6.4 (a) was used. (b) Angle-integrated (*upper*) and -angle-resolved (*lower*) energy spectrum at polar angle $\theta = 50°$. The red curve on top shows the angle integrated energy spectrum, the bottom 2D graph the angle resolved spectrum. The area between the red dashed lines is the energy integrated range used in the delay scan. The two Fermi edges belonging to the two higher harmonics HH 13 and HH 15 are indicated. Due to space charge effects they appear at larger E_{kin} than expected.

be compensated for.
Taking the small expected changes in signal, the low photon flux and the time limited laser stability into account, it was necessary to limit the scanned angular range to a minimum. The azimuthal range of interest for the time-resolved measurements is indicated by the white arc in the simulated UPD map for the WAlküre geometry (Fig. 6.9 (a)) and by the dashed blue lines in Fig. 6.10. The center of the angular axis of the detector crosses the $\bar{\Gamma}\bar{K}$ direction of the reciprocal lattice. The polar angle of this region is $\theta = 50°$ and the full angular range of the detector was used in the $\pm 18°$-mode. Hence the indicated azimuthal range could be recorded without moving the sample. According to the projection rules of the detector angle onto spherical coordinates given in chapter 4, at each detector angle $\alpha \neq 0°$ both spherical angles θ and ϕ change. At $\alpha = \pm 18°$ the probed polar angle is $\theta = 52.3°$ while $\theta = 50°$ for $\alpha = 0°$. The azimuthal range is $\Delta\phi = 127° - 174°$.
To record the time-resolved UPD, a full energy spectrum was recorded at each delay step in the experiment. The angle resolved energy spectrum is shown in the lower part of Fig. 6.11 (b). The upper part shows the angle integrated spectrum. For the delay scan experiment only the middle peak, as indicated by the dashed lines from 15.8 eV to 19.2 eV, was integrated and plotted in the delay scan. In this peak electrons from the whole valence band are present as it consists of the contributions from two harmonics (see Fig. 6.4). Thus at the lower integration border electrons with binding energies $E_B = -4.7$ eV are recorded, since E_F corresponding to HH 15 is located at $E_{kin} = 20.5$ eV. The upper integration border is 1.2 eV above E_F corresponding to HH13, which is just above the fastest electrons emitted through HH 13. This way an averaging over the full valence band was performed. Note that space charge effects broaden the spectrum thus the Fermi

edges appear at larger energies than expected.
Figure 6.12 (a) shows the experimental result of the angle-resolved delay scan in the described area of the UPD pattern. The scan was normalized by the gas phase spectrum from Fig. 6.11. Although the changes in signal are small, an oscillation is visible for positive delays. Due to the low photon flux and the fluctuating light source, the data quality is limited. Still it can be seen that the amplitude has the largest magnitude in the area between $\phi = 136°$ and 146°, in the outer azimuthal regions the oscillation is weakest. The scan is divided in equally broad slices, each of which is angle integrated and plotted in Fig. 6.12 (b). The single spectra are fitted with an exponentially damped harmonic oscillation function. From the fitting function a phonon frequency of $\nu = (2.66 \pm 0.13)$ THz is retrieved. In Fig. 6.12 (b) it becomes more obvious that the range between $\phi = 136°$ and 146° exhibits strongest oscillations and that the oscillations in the outer parts are strongly damped.
A comparison between the phase of the oscillation in measurement (Fig. 6.12) and simulated azimuthal cuts (Fig. 6.10) corroborates the finding that changes of the UPD signal, *i.e.* structural changes are observed, since both predict the same phase of the oscillation: Applying the model of displacive phonons, after excitation the lattice starts from the unexcited lattice configuration to move towards the cubic crystal phase, *i. e.* towards larger values of the lattice coordinate x. The simulations show an intensity increase for larger values of the coordinate x in the probed area. So the increasing intensity in the measurement right after excitation, when the lattice moves towards the cubic phase, goes in line with SSC calculations. Judging from the low similarity of the calculated azimuthal cuts with the measured one, besides the general trend of increasing intensity with increasing x, it would be highly speculative to draw any further conclusions based on the SSC results.

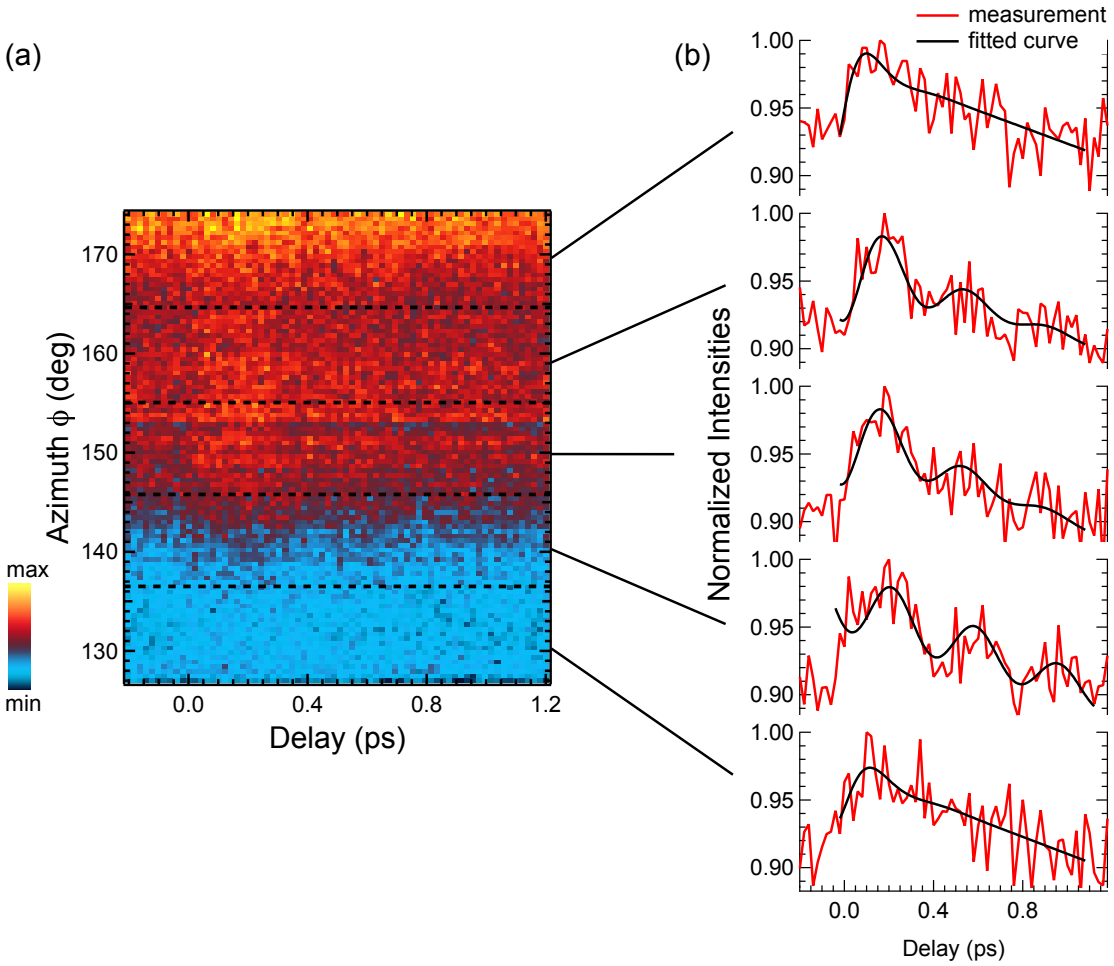

Figure 6.12: Time-resolved UPD: A delay scan at sample position $(\theta_{Man}, \phi_{Man}) = (50°, 150°)$ is shown in (a). The spectrum is normalized by the Ar gas phase scan that was simultaneously recorded to compensate for laser fluctuations. Electrons from the valence band as initial state are excited with two photon energies ($h\nu = 23.5$ and 20.4 eV) and are probed and projected on the spherical emission angle ϕ_{Sph}. The red curves in (b) show the angle integrated delay scans of the various areas in (a) marked with dashed lines. The different curves are fitted with exponentially damped harmonic oscillations (black curves), which are plotted in addition.

6.6 Discussion of structural changes

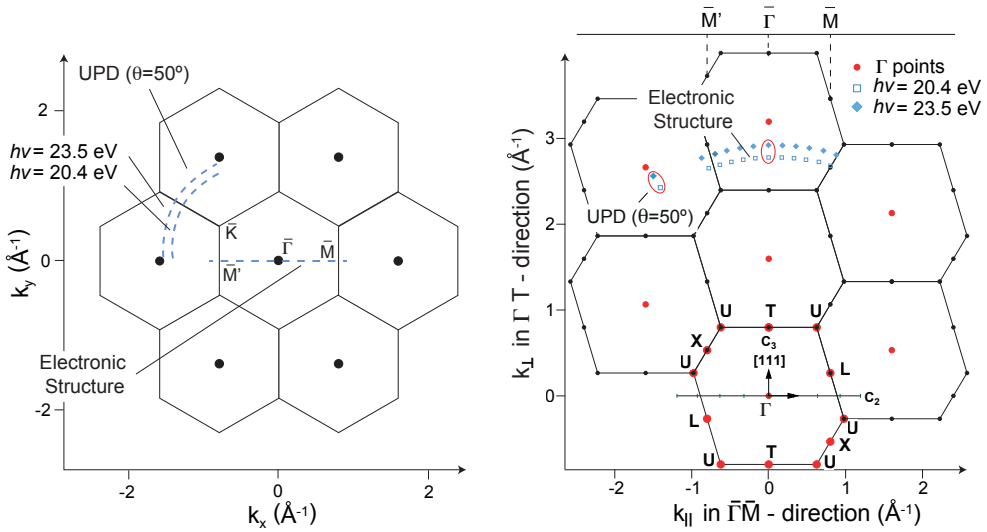

Figure 6.13: Position of measurements in Brillouin zones. (a) Top view on the (111) plane with the surface Brillouin zones. The distance $\bar{\Gamma}\bar{M} = 0.80$ Å^{-1} and $\bar{\Gamma}\bar{K} = 0.92$ Å^{-1}. The dashed curves show the projection of the final state k-vector to $k_{\|}$ in the measurement of the electronic structure and in the UPD measurement. The measurement at $\theta = 50°$ corresponds to a mean $k_{\|} = 1.58$Å^{-1} The high symmetry points $\bar{\Gamma}$, $\bar{K}$, $\bar{M}$, $\bar{M}$' are indicated. (b) Side view on the bulk Brillouin zones. The curves of full and empty diamonds indicate the value of the final state k-vector in the electronic structure measurement. Full diamonds correspond to excitation by $h\nu = 23.5$ eV and empty diamonds to excitation by 20.4 eV. E_0 is assumed to be 13.5 eV and a prominent peak is at $E_B = 3$ eV. The red ellipses denote the regions of interest.

In the following, it has to be carefully checked that the intensity oscillations at $\theta = 50°$ can really be attributed to changes in the UPD signal. Figure 6.13 illustrates again, where the two measurements, the one probing the electronic structure and the one probing UPD, were taken in reciprocal space. Again only normal emission of the electronic structure measurement is considered in this chapter.

In Fig. 6.14 an interesting observation is made by comparing the phase of the oscillation recorded in the delay scan at $\theta = 50°$ and that of the oscillation recorded at normal emission, where the electronic structure was probed. First of all the very fast response that is commonly attributed to the creation of hot electrons, is only visible in the normal emission scan. Furthermore a phase shift of π between the two oscillations is observed, so that the signal recorded at $\theta = 50°$ exhibits a maximum at delays where the DOS at normal emission has its minimum and vice versa. This goes in line with the findings from the previous sections: At normal emission maxima in electronic structure occur when the crystal lattice is closest to the unexcited phase. The modulation depth of the measured oscillation at $\theta = 50°$ is smaller than that of the normal emission experiment. It is about 5%.

Note that the two functions in Fig. 6.14 have slightly different frequencies, as the experiment at $\theta = 50°$ was conducted with a higher fluence, in order to increase the oscillation amplitude. Hence the phase difference between the two curves is slowly increasing.

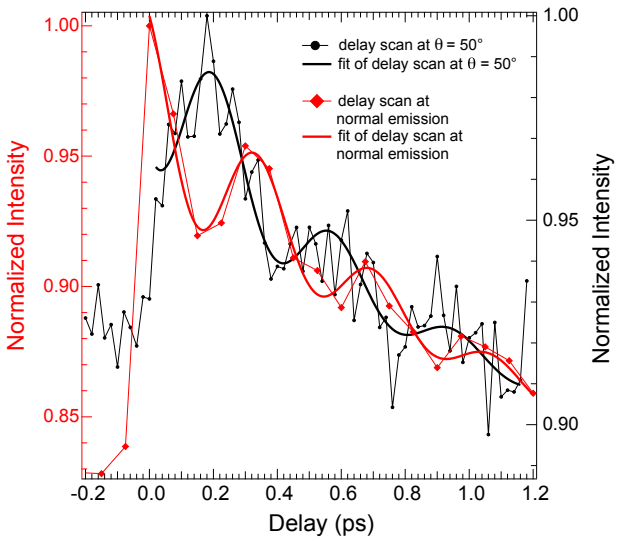

Figure 6.14: Comparison of two delay scans: The left axis refers to the delay scan at normal emission (red), the right axis to the azimuthally integrated delay scan at $\theta = 50°$ (black). The scan at normal emission oscillates with a phonon frequency $\nu = (2.71 \pm 0.06)$ THz, the UPD scan at $\theta = 50°$ has an initial phase shift of π and shows a frequency of $\nu = (2.66 \pm 0.13)$ THz. Both oscillations are fitted with a damped harmonic oscillation function.

To rule out that the oscillatory behavior of the measurement at $\theta = 50°$ stems only from changes in the electronic structure, band structure calculations for different lattice distortions were also conducted for the $\bar{\Gamma}\bar{\mathrm{K}}$ direction at $\theta = 50°$ and $h\nu = 23.5$ eV. As in section 6.3 the band structure was generated over the full height of the Brillouin zone along $k_\perp$. In this case however $E(\boldsymbol{k})$ was generated perpendicular to $k_\parallel = 1.58\text{Å}^{-1}$ along the $\bar{\Gamma}\bar{\mathrm{K}}$ direction, corresponding to experimental values of $k_\parallel$. The calculations were repeated for several azimuthal angles around the $\bar{\Gamma}\bar{\mathrm{K}}$ direction, covering the angular range of the experiment. Furthermore for all angles the DOS was calculated by integration over the full Brillouin zone height, giving an estimate for the expected magnitude of changes in intensity. The results of the calculations for the $\bar{\Gamma}\bar{\mathrm{K}}$ direction are given in Fig. 6.15 (a). First it becomes clear that only few states are available in the considered energy range and none of them are close to E_F, which explains why no fast cosine-like electronic response in the first few femtoseconds after excitation is seen. Consequently also the calculated DOS at the respective $k_\parallel$ is small (compare to numbers of the DOS at $\bar{\Gamma}$). For comparison the valence band excited with He I_α and measured at the emission angle $\theta = 50°$ along $\bar{\Gamma}\bar{\mathrm{K}}$ is plotted in Fig. 6.15 (a). Except for the prominent calculated peak at $E - E_F = -4$ eV , that is not present in the valence band measurement, the spectra agree well.
Also the distortion dependent changes of the DOS presented in Fig. 6.15 (b) are small except of the one at $(\theta, \phi) = (50°, 170°)$. The transient signal calculated by integration of the DOS multiplied with the Fermi-Dirac distribution for $T = 2000$ K (*cf.* section 6.3) is shown in dependence of the distortion $x(t)$. The integration range was again adapted to the one in the experiment (Fig. 6.4), which corresponds to $E - E_F = -4.7$ eV up to 1.2 eV. Taking the states at -4 eV that do not appear in the measurement into account or not does not change the curves qualitatively. It becomes clear that the distortion dependent changes have opposite phase at different azimuthal angles, which is not observed in the experiment. A contradiction between tight binding derived

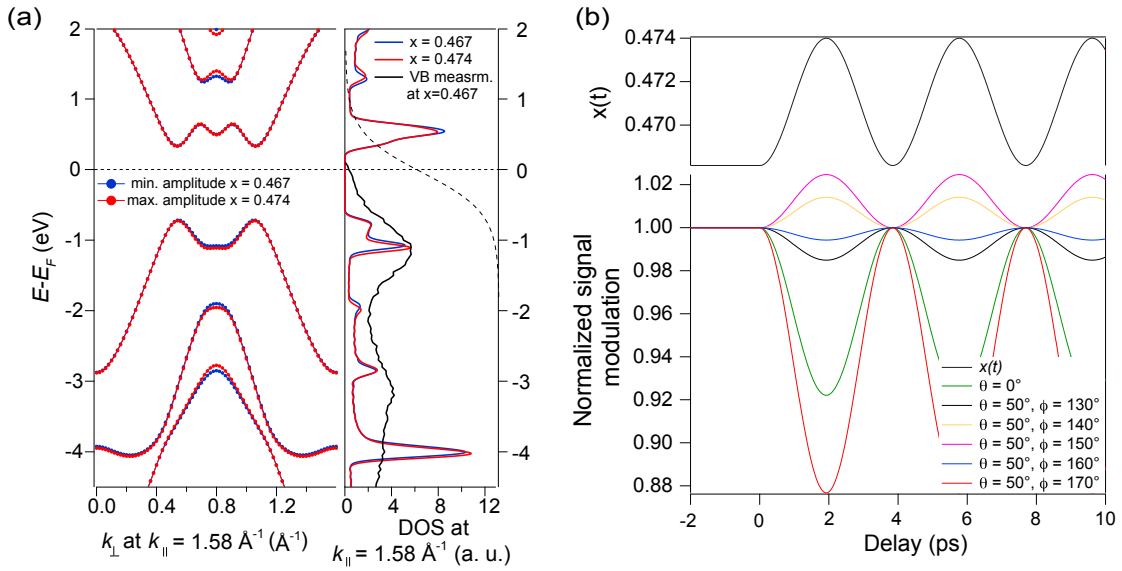

Figure 6.15: (a) *left*: Band structure along $k_\perp$ at $k_\parallel = 1.58\text{Å}^{-1}$ with tight binding calculations. *right*: DOS at $k_\parallel = 1.58\text{Å}^{-1}$ in the direction $\bar{\Gamma}\bar{\text{K}}$ corresponding to $(\theta, \phi) = (50°, 150°)$. For comparison the valence band measurement with He I_α excitation at the same position in reciprocal space is plotted and the Fermi-Dirac distribution function at $T = 2000$ K. Band structure and DOS are both plotted for maximum (red) and minimum (blue) lattice distortions. (b) *Upper part*: Lattice oscillation given by the coordinate x(t). *Lower part*: Calculated intensity oscillation depending on the lattice distortion at $\theta = 50°$ and at several azimuthal angles around $\bar{\Gamma}\bar{\text{K}}$ corresponding to the region of the experiment. For comparison the calculated intensity oscillation at normal emission (green curve) is included. No damping of the signal is considered.

phase and measured phase exists in the region $(\theta, \phi) = (50°, 160°)$.
Nevertheless, even where the simulated oscillation of the electronic structure shows the same phase as the measurement, Fig. 6.15 (b) shows that the simulated changes in amplitude at $\theta = 50°$ are very small (around 2%) compared to those calculated for normal emission (7.5%). In the normal emission case the calculation proved to be precise, thus for $\theta = 50°$ no larger modulation than 2% of the maximum intensity should be expected according to the tight binding results. Still a modulation of 5% is observed, hence the major contribution to the observed signal oscillation can be attributed to a time-dependent oscillation of the UPD signal.
Summarizing for photoemission at $\theta = 50°$ around the $\bar{\Gamma}\bar{K}$ direction, UPD effects are observed, which are underlined by SSC calculations, since they predict the observed oscillatory behavior at this angular region. Tight binding calculations alone cannot explain the observed oscillation as they could for normal emission. With the slow response time and the first maximum at $\Delta t = 185$ fs the oscillation of the UPD signal directly records nuclear motion in the Bi(111) crystal and hence structural dynamics.

6.7 Time-resolved ARPES

In this section the delay scan with the sample at normal emission is discussed under another aspect as compared to chapter 6.3. As mentioned earlier an angular width of $\theta = \pm 27°$ was recorded. So far only the small part around $\theta = 0°$ was considered. In Fig. 6.16 (a) cuts at 3 different angles $\theta = 0°, -24°$ and $24°$ are extracted and energy integrated over the full range $E_{kin} = 18$ eV - 24.5 eV. The position of these points in reciprocal space can be found in Fig. 6.16 (b). One can identify the well known fast response around normal emission and at $\theta = -24°$ close the $\bar{\text{M}}$' point. But at $\theta = 24°$, close to the $\bar{\text{M}}$ point, a phase shift compared to the other two curves becomes visible again.

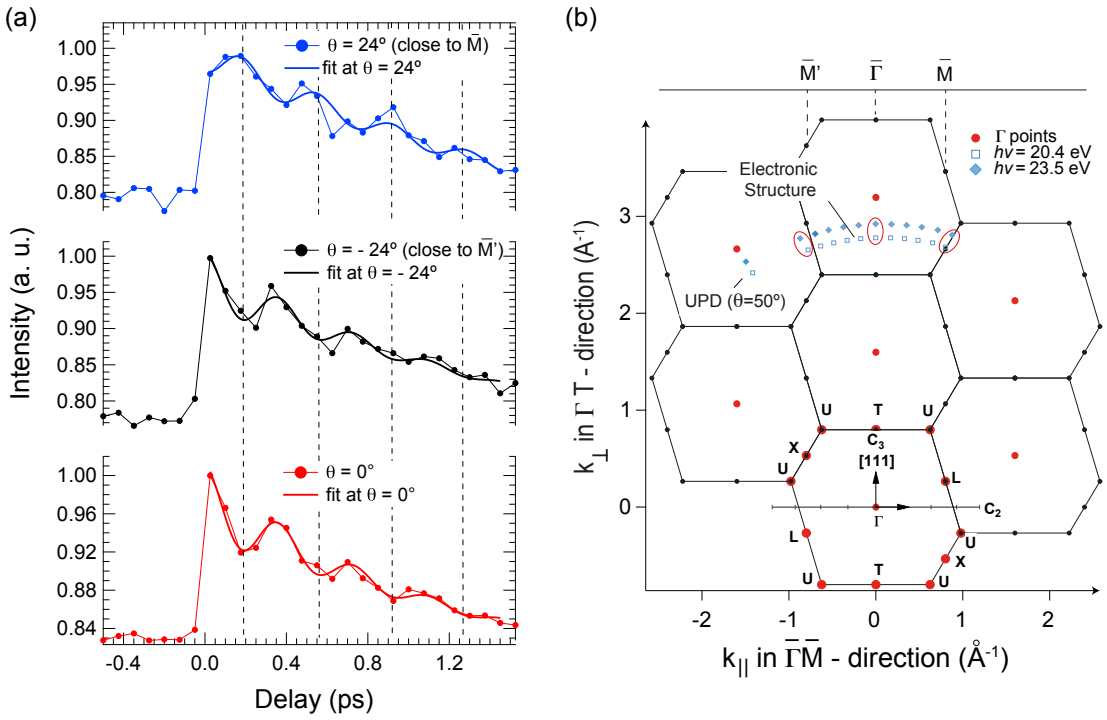

Figure 6.16: (a) Delay scan with sample in normal emission. Three different emission angles are extracted. $\theta = 24$ and $\theta = -24$ are close to the $\bar{M}$ and the $\bar{\text{M}}$' point respectively. All scans are fitted with a exponentially damped harmonic oscillation function. The frequency of the oscillation is $\nu = (2.71 \pm 0.06)$ THz. The scan along $\theta = 24°$ is phase shifted by π with respect to the other two scans. The dashed lines are guides to the eye. (b) Side view on the bulk Brillouin zones. The curves of full and empty diamonds indicate the value of the final state k-vector in the electronic structure measurement. Full diamonds correspond to excitation by $h\nu = 23.5$ and empty diamonds to excitation by 20.4 eV. E_0 is assumed to be 13.5 eV and a prominent peak is at $E_B = 3$ eV. The high symmetry points of the Brillouin zone are indicated. The red ellipses denote the three directions of $\boldsymbol{k}$ that are compared in this section.

Also this is a phase shift of π and the question of its origin arises. UPD simulations using SSC calculations are not presented here, since one important fact has to be considered: In the present measurement no full valence band was integrated, therefore simulations assuming localized initial

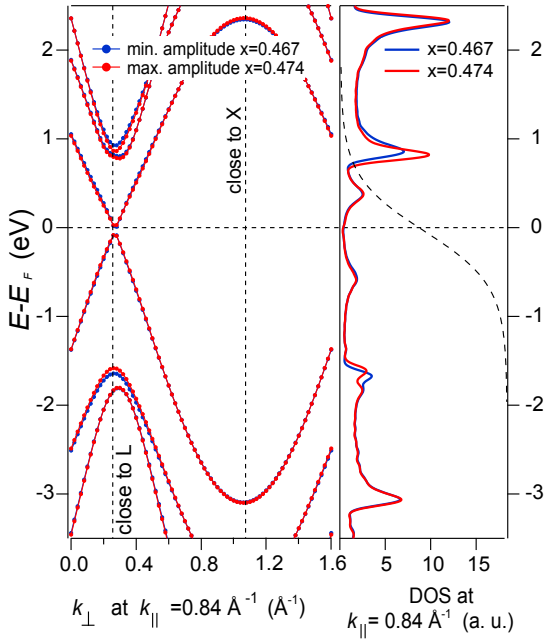

Figure 6.17: *left* The results of tight binding derived energy dispersion $E(k_\perp)$ at $k_\parallel$ corresponding to $\bar{\text{M}}$. L and X points are marked. *Right*: By integration along the full height of the Brillouin zone the DOS is generated. Additionally the Fermi-Dirac distribution function at $T = 2000$K is shown.

states as it is done in SSC, are not reliable. However as in the chapters before, simulations of the electronic structure using the tight binding model will be shown in Fig. 6.17.
The band structure along $k_\perp$ is shown at $k_\parallel = 0.84\text{Å}^{-1}$, *i. e.* close to the $\bar{\text{M}}$ point of the surface Brillouin zone. The band structure perpendicular to the $\bar{\text{M}}$' point is not presented here, since it can be derived by simply reversing the $k_\perp$ axis in Fig. 6.17 and the DOS integrated over the full height of the Brillouin zone would thus give exactly the same result. From Fig. 6.16 (b) one sees that the measurement at the $\bar{\text{M}}$ point probes the vicinity of the X point in the bulk Brillouin zone and the one at $\bar{\text{M}}$' a point close to the L point. The calculated DOS over the full Brillouin zone height shows again only few states (compare to numbers of the DOS at $\bar{\Gamma}$). The few available states only originate from bands around the L point except of the top most and the lowest peaks in the DOS. So the excitation of hot electrons is only to be expected at measurements close to the L point, *i. e.* with the here used photon energies at the $\bar{\text{M}}$' point. This explains why the creation of hot electrons is only seen in the curve extracted at $\theta = -24°$. Furthermore the cosine-shaped oscillation is explained by the distortion dependent integrated DOS in Fig. 6.18. The integration boundaries correspond to the measured energy range ($E_{kin} = 18$ eV to 24.5 eV): $E - E_F = -3$ eV to 2 eV. Again each value was multiplied by the energy dependent Fermi-Dirac distribution function for an electronic temperature of $T = 2000$ K.
With a low surface Debye temperature of $\theta_D = 48$ K and a low melting point at $T = 271°$ C [105] inelastically scattered states will contribute considerably at room temperature measurements. Thus even so no energy bands are available in the probed region at the X point, electron intensities can be measured. However with no electronic structure being present, no fast electronic excitation is expected, which is seen in the topmost graph of Fig. 6.16. An explanation for the π phase shift over the whole duration of the delay scan can only be guessed but it might be that in

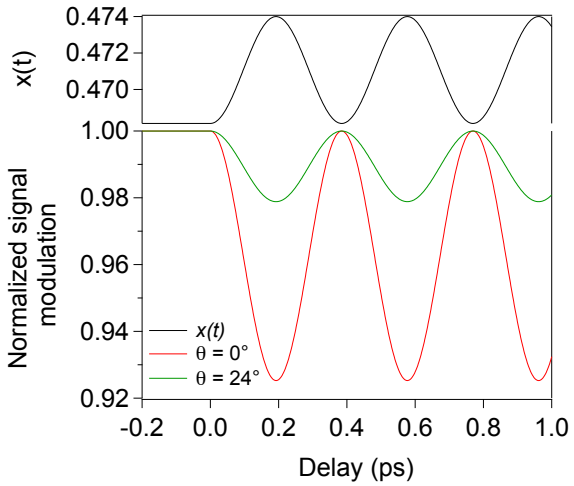

Figure 6.18: Distortion dependent signal modulation. For larger lattice distortions x(t) towards the cubic crystal lattice, the electronic structure at $\theta = 24°$ ($\bar{\mathrm{M}}$) decreases (green). For comparison the calculated change of signal at $\bar{\Gamma}$ is plotted (red).

the absence of large electron densities structural changes of the lattice and thus UPD effects are dominant and show the respective phase in their oscillation. For an exact calculations of these effects scattering calculations for electrons from delocalized initial states would be required.
The findings of this section considering the two points $\bar{\mathrm{M}}$' and $\bar{\mathrm{M}}$ together with the results at $\theta = 50°$ leave an intuitive picture: If electronic states are scarce, no fast electronic response is to be expected but UPD effects can become important that directly follow the motion of nuclei.
Concluding, this whole chapter 6 showed a proof of principle measurement of time-resolved UPD. Due to very low count rates and limited laser stability the measured region at $\theta = 50°$ covers only a part of the full 2π hemisphere on top of the sample. Since tight binding calculations alone could not explain the modulation strength of the measured signal and SSC calculations predicted the measured oscillatory phase, a major contribution of the measured signal was attributed to time-resolved UPD effects. Two regions in reciprocal phase were found where the measured signal directly followed the time evolution of nuclear motion giving direct access to structural dynamics measurements.

6.8 Appendix - Signal background

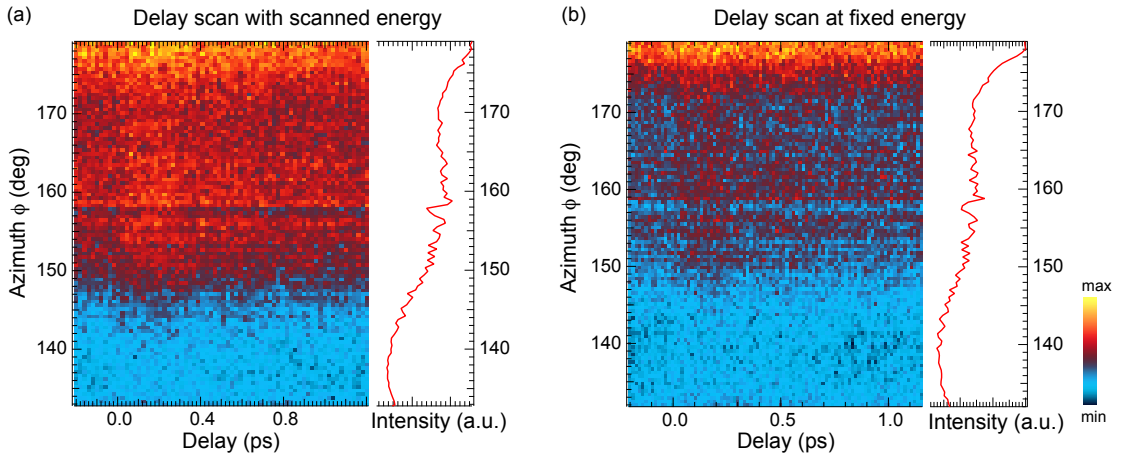

Figure 6.19: (a) The same delay scan as shown before in section 6.5 at $(\theta, \phi) = (50°, 155°)$ recorded in the energy scanning mode. The red curve shows the time integrated angle dependent signal. (b) Delay scan at the same sample position as in (a) but in the fixed energy mode. Again the red curve shows the time integrated angular distribution.

Apart from a normalization using the TOF signal from the Ar gas-phase measurement, no more corrections were made in the delay scan graph in Fig. 6.12. As discussed in chapter 4 the detector shows a pronounced angle-dependent transmission function T(E,α). In the framework of this work only for a fixed kinetic electron energy $E_{kin} = 16.3$ eV a function T(α) was recorded but not for the integrated energy window used for the delay scan. Thus a normalization of the delay scan was not possible.
Figure 6.19 (a) shows the discussed delay scan and its time integrated signal. The time integrated signal is a superposition of the slope in the azimuthal scan of the UPD signal (see Fig. 6.10) and the transmission function. Delay scans were not only conducted using the energy scanning mode of the analyzer, but also using the fixed energy mode, resulting in worse signal to noise ratios but otherwise the same results (Fig. 6.19 (b)). Also here the time integrated signal is presented. Both delay scans were recorded at the same sample positions. For fixed energy measurements a normalization with the transmission function is possible. Figure 6.20 (b) shows how the correctly normalized fixed energy scan leads to a linear increase of the signal, as expected from the azimuthal scan. In (a) it becomes obvious that using the same function for normalization of the energy scan induces a misleading non-physical maximum. As this normalization procedure only changes the signal along the angular axis, all delay dependent findings are not affected and thus the data can be presented non-normalized as in the previous sections.

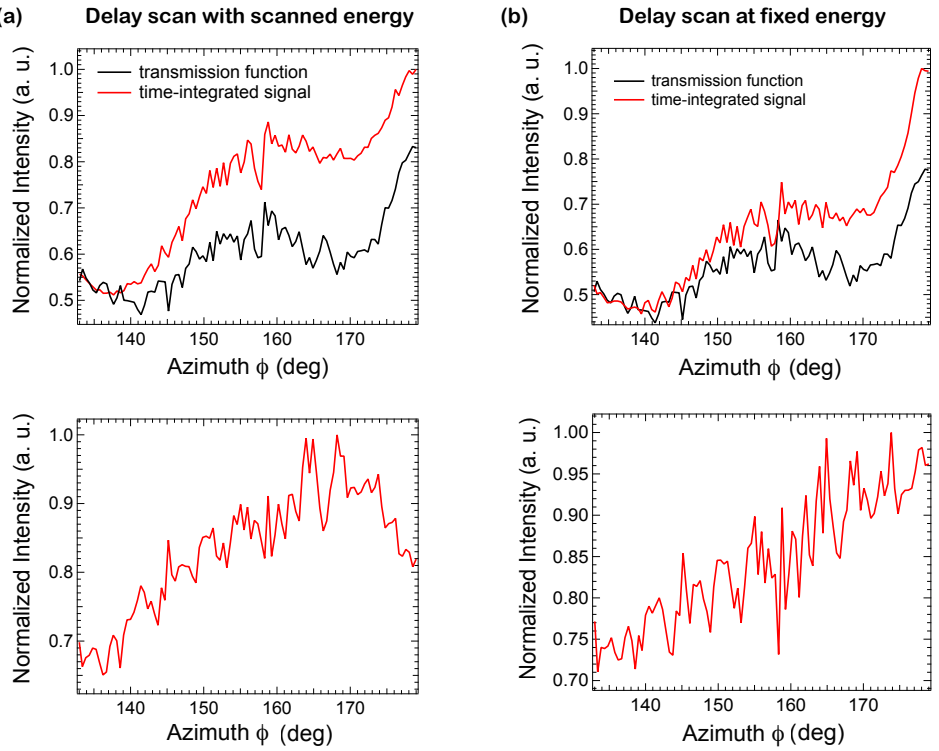

Figure 6.20: (a) The time-integrated angle-resolved signal of the delay scan in scanning energy mode (red) and the transmission function (black) at fixed $E_{kin} = 16.6$ eV are both shown in the upper panel. The black curve was multiplied in order to coincide with the red curve at small angles. In the lower part the normalized angle resolved signal of the delay scan is plotted. In (b) in the upper panel the time-integrated angle-resolved signal of the fixed energy delay scan is plotted in red. In black the transmission function is given. In the lower panel the normalized angle-resolved signal of the fixed energy delay scan is given.

7 Time-resolved XPD of CO on Pt(111) - A theoretical study

As an outlook on potential applications of the "time-resolved photoelectron diffraction"-method a time-resolved XPD measurement for a molecular case is simulated. The experiment could be performed in a THz-pump - x-ray-probe setup. With a combination of DFT and molecular dynamics calculations the vibrations of carbon monoxide (CO) molecules on a platinum (111) surface excited by a laser pulse with a frequency of 2 THz are computed. The resulting cluster coordinates for different time steps are then used in SSC calculations to mimic a real time-dependent XPD measurement using the C1s core level as emitter. By averaging over 50 trajectories, which all start at different thermal excitation states, a molecular movie is created. The movie follows the angular position of the oxygen scatterer with atomic resolution. Before excitation the averaging over many molecules leads to high intensity at the center of the diffraction map at $\theta = 0°$. After excitation by the 2 THz pulse, the molecular dipoles start to align azimuthally in the strong electric field and a coherent wagging motion of the molecules following the oscillation of the electric field becomes visible. After the pulse has passed azimuthal disordering can be observed.

7.1 The system

With platinum being a heterogeneous catalyst for the reactions of carbon monoxide, the system has been of great interest to technology for a long time. Thus there have also been many studies examining the system CO on Pt(111) for many years and with different experimental methods. From LEED and desorption experiments, the CO adsorption behavior is well known. For a coverage $\theta < 0.17$, the molecules adsorb exclusively on energetically favored "on top"-sites of the platinum surface. For a coverage of $\theta > 0.17$ the carbon monoxide also adsorbs on the "bridging"-site until at $T = 300$ K the coverage is saturated at $\theta = 0.5$, *i. e.* there are half as many molecules as Pt-atoms on the surface. At this coverage 50% of the molecules are adsorbed on the "bridging" and 50% on the "on top"-site [106–108]. With increasing coverage the change in work function of the CO/Pt(111) system shows a peculiar behavior: Until the coverage reaches $\theta = 0.17$ the work function is constantly lowered but for larger coverages rises again until at $\theta = 0.5$ it has nearly the same value as the pristine metal. This behavior could be explained by different dipole moments of CO due to the two different adsorption sites [106]. Later calculations showed that the dipole moment of CO has opposite sign, when adsorbed on the "bridging"-site compared to the "on top"-site [109].
The molecules are chemisorbed mainly by a hybridization of the molecular 5σ-bond and the sp-band of the platinum [106, 110]. The 5σ molecular orbital is located in large part at the carbon

atom of the CO. Thus the carbon is close to the surface, while the oxygen atom points upwards away from the surface [15, 108]. This model was corroborated in an XPD analysis of the system by Wesner *et al.* [111]. The C1s forward scattering peak was located at normal emission. Moreover a width analysis showed that, assuming an isotropic azimuthal distribution, the mean tilting angle of the molecules goes up to $\theta = 10°$.
In order to characterize the diffusion, desorption and dissociation characteristics of the molecules, the system was also examined with vibrational spectroscopy. Thereby one of the normal modes discovered in a helium scattering experiment was attributed to a hindered or frustrated translational mode of the CO on Pt(111) leading to a wagging motion of the molecule. The corresponding vibrational frequency at a saturated coverage was measured to be $\nu = 1.79$ THz [112]. The normal mode shows no dispersion, meaning that the interaction of the molecules amongst each other is only weak. With the advent of very intense THz pulses it was suggested that the wagging of the polar carbon monoxide could be enhanced by laser pulses of resonant frequency so that the molecules tilt down close enough to the surface to initiate surface catalytic reactions [15]. The idea of this chapter, however, deals with a regime where the THz pulse does not tilt the molecules entirely down to the surface, but rather makes them oscillate. That way it is possible to follow the molecular motion with a time-resolved XPD experiment using a pump-probe setup. In such a measurement, the THz pulse acts as the pump pulse to excite the molecular mode, while a synchronized pulsed x-ray beam, like from a free electron laser (FEL) acts as the probe pulse. Using the C1s state as emitter, a diffraction pattern with atomic resolution can be recorded that changes with the time delay between the two pulses. Thus a molecular movie becomes possible.

7.2 Computational work

To simulate such an experiment, first the motion of atoms has to be calculated. An established method for that are molecular dynamics (MD) calculations [113, 114], where harmonic forces between the bonded atoms are assumed, whose parameters are determined from electronic structure calculations or experiments. Solving the mechanical equation of motion of such a system not only gives vibrational frequencies, but also reveals the energy flow inside the system and makes it possible to follow molecular motion. The coupling to the $6 \cdot 10^8$ V/m strong electric field was modeled via point charges on the atoms of the polar CO molecule and the system was thermalized to $T = 298$ K. To calculate the molecular motion a simple cosine pulse with $\nu = 2$ THz and a pulse duration of 5 ps was assumed. The calculations of the molecular motion were performed by collaborators from the Markus Meuwly Group in the Chemistry Department of the University of Basel [115].
The output of the MD calculations gave time-dependent coordinates of atoms in a cluster consisting of two layers of Pt atoms with an adsorbed CO molecule on top. Figure 7.1 shows a representative cluster used for calculations. The CO is adsorbed at the "on-top" site with its dipole moment pointing away from the surface along the molecular axis [106, 109]. For each time step of 5 fs a new cluster file was created and served as input to SSC calculations to simulate time-dependent XPD patterns.
In the SSC calculations a photon energy of $E = 1000$ eV was assumed and the C1s core level was chosen as emitter. Since the spatial resolution of the electron detector is usually on a macroscopic scale, the electron signal is averaged over large parts of the light spot, *i. e.* integrated over the signals from many molecules. To mimic this, the results from SSC calculations of 50 different molecular trajectories were summed up for each time step. Each trajectory started at a different

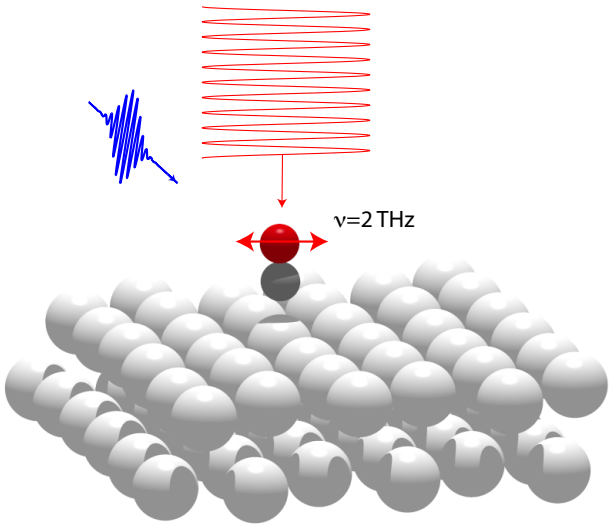

Figure 7.1: Sketch of the pump-probe experiment to record time-resolved XPD. The red 2 THz pulse acts as pump and the CO molecule on top of the Pt(111) surface follows the laser oscillations. With the blue x-ray pulse the molecular position is probed by recording an XPD pattern. Depending on the delay between blue and red pulse the position of the CO atoms vary.

initial point on the reaction coordinate, due to thermal motion.
One has to consider that a time-resolved XPD experiment will only reveal molecular oscillations, if most of the molecules undergo a coherent motion.

7.3 Results

As the electrons of the C 1s core level are excited with $h\nu = 1000$ eV photons, they are strongly forward focussed when they scatter at the potential well of the oxygen atom. The position in the diffractogram where the highest intensities appear can therefore clearly be attributed to the angular position of the oxygen atom and hence the tilting angle of the molecule [111]. It turns out that the position of the main maximum gives the tilting angle θ as well as the azimuthal angle ϕ very precisely, as can be proven by simply comparing with atomic coordinates of the input cluster. In order to distinguish the behavior of single molecules from that of the averaged ensemble, the oscillation of the polar angle from only a single molecular trajectory is plotted in Fig. 7.2 (a). These data were taken from the coordinate files coming from the MD simulation directly. The polar angle of molecules with azimuthal angles $90° < \phi < 270°$ were multiplied by a factor of -1, in order to encode the correct oscillatory behavior of the wagging motion. The figure shows that even before the excitation by the pump pulse, the molecule has a significant hindered translational wagging motion. This is due to thermal activation at $T = 298$ K and it has already been estimated that this mode is active at room temperature [116, 117]. Although the mean tilting angle should be around $\theta = 10°$, single molecules can have larger amplitudes, due to a statistical energy distribution. When excited by the pump pulse, more energy is transferred into the frustrated translational mode and the angular amplitude of the wagging increases. After the pump pulse is gone, it does not seem to relax in the time window shown up to delays of 25 ps. Figure 7.2

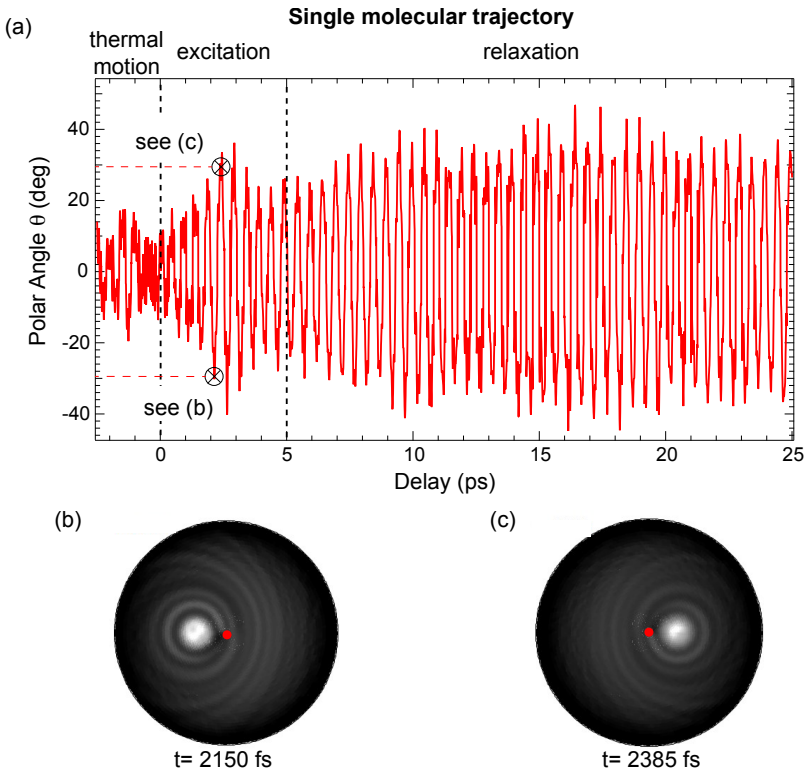

Figure 7.2: (a) Time evolution of the wagging motion of a CO molecule on a Pt(111) surface for a single trajectory. For delays between the dashed lines the pump pulse is present At two points the full XPD maps are extracted and shown in (b) and (c). Both points are marked. (b) XPD map of the single trajectory at delay $t = 2150$ fs. (c) XPD map of the single trajectory at delay $t = 2385$ fs.

(b) and (c) show XPD maps of the single molecule trajectory at two different time steps. The angular position that can be drawn from the intensity maximum of the XPD maps nicely fits to the angular position calculated from the input clusters. Around the intensity maximum appear interference fringes between scattered and unscattered wave.
A real XPD experiment however can only be mimicked by averaging over an ensemble of molecules. With the SSC calculations averaged over 50 trajectories a molecular movie was created that shows the time-resolved structural changes of the full ensemble. In Fig. 7.3 parts of the movie are presented. It shows a delay scan of 25 ps, where the 5 ps long pump pulse is present from 0 to 5 ps. Before and after these delays the system is unperturbed, when the probe beam arrives. In (a) the average polar angle of the CO is plotted, which was determined by extracting the emission maximum of the averaged SSC calculated diffraction maps. The averaging was carried out over all 50 trajectories at each time step.
One sees that the molecules have an average polar angle around 0 before excitation. Although single molecules show an activated hindered translational mode, first their isotropic azimuthal ordering and second the incoherent phases of their oscillations lead to an averaging out of the polar angle that is extracted from the averaged XPD maps. At the instance when the pump pulse arrives the molecules start to align in azimuthal orientation and coherent hindered translational oscillation begins. This can be understood by the picture of a dipole in an electrical field: The

rotational frequency of CO on Pt(111) is $\nu = 12.33$ THz [108]. Hence the rotational movement of a CO molecule is about one order of magnitude faster then its wagging motion. As a consequence within a half cycle of the 2 THz pulse, during which the electrical field has a constant sign, the molecules have enough time to align their tilting motion parallel to the laser field. Thus in Fig. 7.3 (a) a coherent oscillation with $\nu = 2$ THz starts for delays $\Delta t > 0$ fs. While the pump pulse is present the amplitude of the oscillation increases constantly to approximately $\theta = 20°$ as more and more energy is deposited in the tilting modes of the molecules. Fig. 7.3 (b) and (c) show snapshots from the created molecular movie of such averaged diffraction maps. It can be seen that a distinct maximum is visible, due to the coherent molecular movement. The clear interference fringes that are visible in the snapshots from the single trajectory are less pronounced due to the averaging. After 5 ps, when the 2 THz pulse has passed one can still see an increase of the

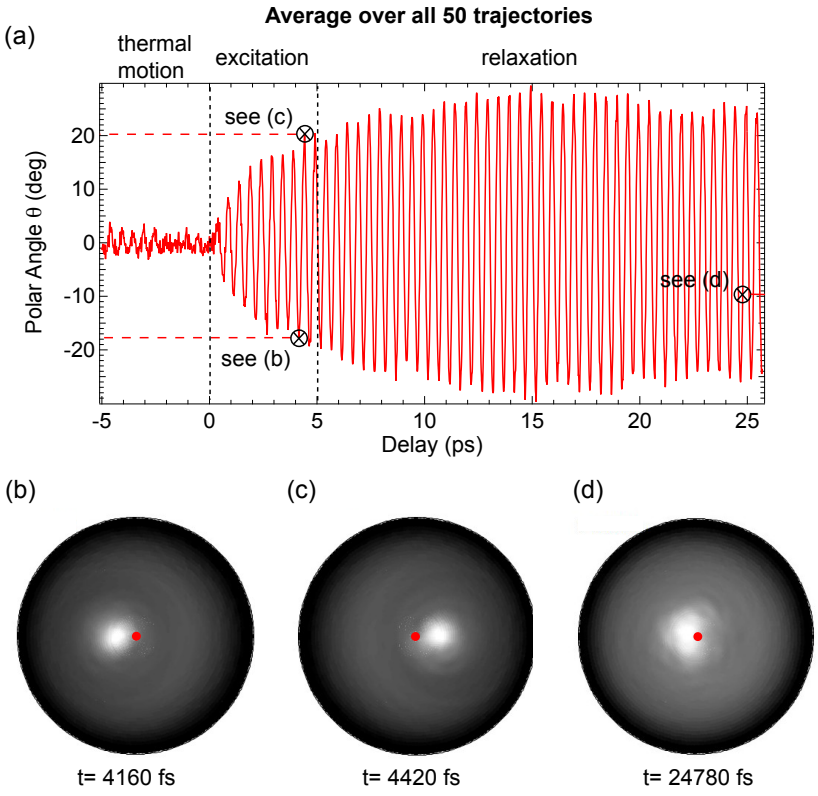

Figure 7.3: Simulation of a pump-probe XPD measurement. In (a) the time-dependent polar angle of maximum emission from the averaged diffraction maps is plotted. It represents the ensemble-averaged orientation of the CO molecules on Pt(111). For positive delays an oscillation with $\nu = 2.0$ THz is visible. At delays between the dashed lines the pump pulse is present. (b) (c) and (d) show the full averaged diffraction maps that were calculated with SSC simulations. No normalization was applied. The delay times of all three patterns are marked with black circles in (a). Each diffraction map is ensemble averaged over calculations from 50 different cluster files. The red points in the middle of the maps show the normal emission direction.

amplitude. This suggests that energy from the substrate or other excited modes is transferred into the hindered translational mode after the pulse is gone. In Fig. 7.3 (d) at a late time after

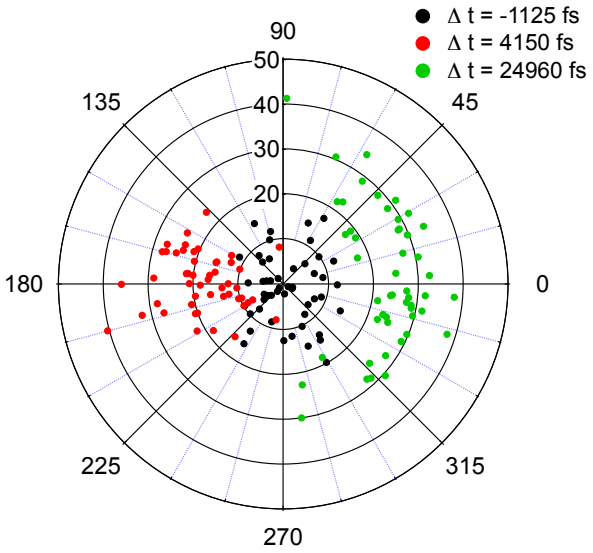

Figure 7.4: Angular order of the CO molecules: At 3 different time steps the angular position (θ, ϕ) of the oxygen atom respective to the carbon emitter is plotted for each of the 50 trajectories. Dots from the same color belong to the same delay step.

excitation the high intensity spot is broadened, showing that the azimuthal alignment is partially lifted. This is expected as no aligning field is present anymore. The temporal evolution of the azimuthal ordering is illustrated in Fig. 7.4, in which the polar positions of the oxygen atoms with respect to the carbon emitters are plotted.
While the azimuthal distribution of the 50 different molecular trajectories at delay $\Delta t = -1125$ fs is isotropic, at the end of the pump period, *i. e.* at $\Delta t = 4150$ fs the molecules have the highest azimuthal order. At long delays after the pump pulse like at $\Delta t = 24960$ fs the azimuthal order is partially lost. At both, $\Delta t = 4150$ and $\Delta t = 24960$ fs the wagging oscillation is at extremal amplitudes.
From the given arguments one can conclude that the increase of the polar amplitude as seen in Fig. 7.3 stems from two effects: First the amplitudes of the single molecules increase due to the energy deposited into the frustrated translational mode by the pump pulse, second the azimuthal ordering of the CO particles is important otherwise an isotropic ordering would cancel out to zero polar angle. One thing that seems puzzling in Fig. 7.3 (a) as well as in Fig. 7.2 is the fact that the excited hindered translational mode shows very long lifetimes. The computed lifetime of the wagging mode with only electronic relaxation is $\tau = 29.4$ ps [118]. In the simulations of the present work higher levels were excited by the THz pump pulse than in [118], making a comparison of lifetimes more difficult. However the observation of very long life times can be rationalized by the fact that electronic excitations of the surface are not considered in the MD calculations. In the method used here the only way to dissipate energy into the Pt(111) cluster is by coupling of vibrational excitations. Accordingly the lifetime of the hindered translational excitations is overestimated here.
Summarizing this simulation shows how time-resolved XPD can visualize structural dynamics taking advantage of coherent motion. An example of a molecular movie was presented in this chapter, in which molecular motion can in fact be followed in real time and with atomic resolution. However

a special treatment of relaxation processes like the introduction of so-called "electronic friction" [119] in the MD calculations might improve the results. Due to different adsorption regimes and accordingly opposite dipole orientations, a coverage of $\theta = 0.17$ should not be exceeded in a real experiment. Another experimental limit might be desorption of the CO due to the uptake of too much vibrational energy from too intense pump pulses. Excited with IR photons the CO desorption rate depends on both the pulse duration and fluence. It was shown that desorption is negligible for pulse durations larger than 500 fs but up to a fluence of $F = 5 \frac{\mathrm{mJ}}{\mathrm{cm}^2}$ only [120]. In the calculations of this chapter with a field strength of $E = 6 \cdot 10^8 \frac{\mathrm{V}}{\mathrm{m}}$ and the pulse duration of $t = 5$ ps a comparably large fluence of $F = 239 \frac{\mathrm{mJ}}{\mathrm{cm}^2}$ was applied. The mechanisms of thermal desorption in the THz regime will most likely be different from those in the IR regime. A discussion of these mechanisms and the limits of field strength is out of the scope of this work. The same applies to the ability of the substrate to screen the electrical field and thus to influence the strength of the wagging motion of CO.

A digital version of the molecular movie from CO on Pt(111) is on the media CD of this work.

8 Summary

In this dissertation a route towards the measurement of femtosecond resolved structural dynamics, using photoelectron diffraction, was presented. The advantages of this method are large scattering cross sections compared to x-ray diffraction measurements and high time-resolution compared to electron diffraction experiments.
In the beginning of the thesis the setup of a new apparatus including a hemispherical electron analyzer, featuring a wide angle lens (WAL), was an integral part of the work. The analyzer was characterized and its ability to swiftly record large parts of the 2π hemispherical electron distribution was proven in chapter 4. Difficulties in the measurements of diffraction maps arose from the strong gradients of the angle dependent transmission function at low energies. Although in the presented data the angular dependence from the transmission function could be averaged out by normalization procedures, the problems cannot be completely solved for signals with low anisotropy. Currently the manufacturer is working on new lens modes that should result in more isotropic transmission functions along the angular axis at the cost of smaller angular ranges, however. One prototype of such a lens mode with range $\Delta\alpha = \pm 18°$ was already used to record the delay scan shown in Fig. 6.12 and gave improved results.
In parallel to the setup of the new chamber with the WAL detector and its characterization, the UPD method was applied to SnPc molecules adsorbed on Ag(111) in order to test the sensitivity and structural resolution of the method (chapter 5). It came out that UPD is perfectly suited to resolve structural parameters like bonding distances with sub-Ångstrom resolution and therefore is an ideal candidate for structural dynamics measurements. For the UPD simulations of SnPc the already existing SSC code was modified in order to calculate emission from non isotropic orbitals. In case this code shall be further modified, a next step could be the implementation to calculate not only single l-type states but also mixed states like sp-dominated orbitals for example.
Only by combining a modern 2D hemispherical analyzer and a laser beamline being able to create pulsed XUV photons from HHG, it became possible to realize the measurement of structural dynamics on a femtosecond time scale (chapter 6). A remarkable feature of this setup was the fact that the experiment could be conducted in a table top laboratory environment.
As the system of choice a Bi(111) crystal was used, since coherent optical phonons (A_{1g}) of the crystal lattice can be excited with IR pulses. It was shown that apart from the electronic response caused by the phonons, structural changes of the Bi(111) lattice could be accessed by the measurement of photoelectron diffraction effects, giving similar results as x-ray diffraction experiments. Not the whole UPD pattern but specific parts of it were examined and time- and angle-dependent changes were observed. Tight binding calculations alone could not explain the strength of the oscillating signal. However SSC calculations predicted the observed oscillatory behavior, giving rise to the statement that structural changes of the lattice contribute to the measured signal. Furthermore two regions are compared, showing that UPD effects might become dominating, if only few states in the band structure are available.

For future experiments the data quality of the time-resolved measurements has to be increased. Therefore higher photon fluxes or longer integration times are needed. The factor that hindered the use of larger photon fluxes was clearly the occurrence of space charge effects at too high laser intensities. A measure to increase the photon flux without increasing the laser intensity would hence be the use of higher pulse repetition rates. In order to increase the possible measurement times the laser stability needs to be improved or better means to normalize fluctuations applying shutter techniques are required.
In the last chapter of the thesis a theoretical study about the possibility to expand time-resolved photoelectron diffraction towards the XPD regime was presented. It could be shown that by the emission from the C 1s state a distinct forward scattering signal of the oxygen atom in an oscillating CO molecule on Pt(111) can be expected, when CO molecules are coherently excited by strong THz fields. In this way a molecular movie becomes feasible that images moving atoms of a molecule in a very direct manner. For a realization of this experiment a 2 THz source would need to be synchronized with a pulsed x-ray source like a free electron laser.
Finally time-resolved XPD is a promising method to directly follow adsorbed molecules in real time, if they exhibit a coherent motion. Time-resolved UPD gives another possibility to measure structural dynamics on ultrafast timescales. As it can be used in combination with HHG light pulses that are generated in more and more laboratories, UPD is a great alternative method compared to those that require pulsed x-rays, like x-ray diffraction.

Bibliography

[1] F. Crick, What Mad Pursuit, Basic Books, 1990.

[2] M. Dantus, M. J. Rosker, A. H. Zewail, Real-time femtosecond probing of "transition states" in chemical reactions, The Journal of Chemical Physics 87 (4) (1987) 2395.

[3] J. C. Williamson, J. M. Cao, H. Ihee, H. Frey, A. H. Zewail, Clocking transient chemical changes by ultrafast electron diffraction, Nature 386 (6621) (1997) 159–162.

[4] C. Y. Ruan, V. A. Lobastov, R. Srinivasan, B. M. Goodson, H. Ihee, A. H. Zewail, Ultrafast diffraction and structural dynamics: The nature of complex molecules far from equilibrium, Proceedings of the National Academy of Sciences of the United States of America 98 (13) (2001) 7117–7122.

[5] B. J. Siwick, J. R. Dxyer, R. E. Jordan, M. R. J, An Atomic-Level View of Melting Using Femtosecond Electron Diffraction, Science 302 (5649) (2003) 1382–1385.

[6] R. J. D. Miller, R. Ernstorfer, M. Harb, M. Gao, C. T. Hebeisen, H. Jean-Ruel, C. Lu, G. Moriena, G. Sciaini, 'Making the molecular movie': first frames, Acta Cryst (2010). A66, 137-156 [doi:10.1107/S0108767309053926] (2010) 1–20.

[7] P. Beaud, S. Johnson, A. Streun, R. Abela, D. Abramsohn, D. Grolimund, F. Krasniqi, T. Schmidt, V. Schlott, G. Ingold, Spatiotemporal Stability of a Femtosecond Hard–X-Ray Undulator Source Studied by Control of Coherent Optical Phonons, Physical Review Letters 99 (17) (2007) 174801.

[8] A. H. Chin, R. W. Schoenlein, T. E. Glover, P. Balling, W. P. Leemans, C. V. Shank, Ultrafast structural dynamics in InSb probed by time-resolved x-ray diffraction, Physical Review Letters 83 (2) (1999) 336–339.

[9] K. Sokolowski-Tinten, C. Blome, J. Blums, A. Cavalleri, C. Dietrich, A. Tarasevitch, I. Uschmann, E. Förster, M. Kammler, M. Horn-von Hoegen, Femtosecond X-ray measurement of coherent lattice vibrations near the Lindemann stability limit, Nature 422 (6929) (2003) 287–289.

[10] R. Fasel, J. Wider, C. Quitmann, K.-H. Ernst, T. Greber, Determination of the Absolute Chirality of Adsorbed Molecules, Angewandte Chemie International Edition 43 (21) (2004) 2853–2856.

[11] M. Greif, L. Castiglioni, A. P. Seitsonen, S. Roth, J. Osterwalder, M. Hengsberger, Photoelectron diffraction in the x-ray and ultraviolet regime: Sn-phthalocyanine on Ag (111), Physical Review B 87 (2013) 085429. doi:10.1103/PhysRevB.87.085429.

[12] T. Greber, Exploiting the photoelectron source wave with near-node photoelectron holography, Journal of Physics: Condensed Matter 13 (2001) 10561–10576.

[13] A. McPherson, G. Gibson, H. Jara, U. Johann, T. S. Luk, I. A. McIntyre, K. Boyer, C. K. Rhodes, Studies of multiphoton production of vacuum-ultraviolet radiation in the rare gases, JOSA B 4 (4) (1987) 595–601.

[14] P. B. Corkum, Plasma perspective on strong field multiphoton ionization, Physical Review Letters 71 (1993) 1994–1997.

[15] B. D. Patterson, J. Sa, A. Ichsanow, C. P. Hauri, C. Vicario, C. Ruchert, I. Czekaj, R. Gehrig, H. C. Sigg, J. A. van Bokhoven, B. Pedrini, R. Abela, Can Energetic Terahertz Pulses Initiate Surface Catalytic Reactions on the Picosecond Time Scale?, CHIMIA International Journal for Chemistry 65 (5) (2011) 323–325.

[16] H. Hertz, Über einen Einfluss des ultravioletten Lichtes auf die electrische Entladung, Annalen der Physik 267 (8) (1887) 983–1000. doi:10.1002/andp.18872670827.

[17] A. Einstein, Über einen die Erzeugung und Verwandlung des Lichtes betreffenden heuristischen Gesichtspunkt, Ann. Phys. 17 (1905) 132.

[18] S. Huefner, Photoelectron spectroscopy: Principles and Applications, Springer Science and Business Media, 2003.

[19] D. Leuenberger, Electron dynamics in low-dimensional surfaces studied by time-resolved photoelectron spectroscopy, Ph.D. thesis, University of Zurich (2012).

[20] H. Haken, H. C. Wolf, Molekülphysik und Quantenchemie, Springer, 2006.

[21] C. Cohen-Tannoudji, D. Bernard, F. Laloe, Quantum Mechanics, Vol. 2, John Wiley and Sons, New York, London, Sydney, Toronto, 1977.

[22] W. Demtroeder, Experimentalphysik 3 Atome, Moleküle und Festkörper, 3rd Edition, Springer, 2005.

[23] J. Osterwalder, T. Greber, P. Aebi, R. Fasel, L. Schlapbach, Final-state scattering in angle-resolved ultraviolet photoemission from copper, Physical Review B 53 (15) (1996) 10209–10216.

[24] D. Briggs, J. Grant (Eds.), J. Osterwalder in Surface Analysis by Auger and X-Ray Photoelectron Spectroscopy, IM Publications and Surface Spectra Limited, 2003.

[25] R. Fasel, M. Gierer, H. Bludau, P. Aebi, J. Osterwalder, L. Schlapbach, Surface alloy formation and interdiffusion in $(\sqrt{5} \times \sqrt{5})$ R27°-YbAl (001): a combined low-energy electron diffraction and X-ray photoelectron diffraction study, Surface Science 374 (1) (1997) 104–116.

[26] P. Krueger, F. Da Pieve, J. Osterwalder, Real-space multiple scattering method for angle-resolved photoemission and valence-band photoelectron diffraction and its application to Cu(111), Physical Review B 83 (11) (2011) 115437.

[27] S. M. Goldberg, C. S. Fadley, S. Kono, Photoionization cross-sections for atomic orbitals with random and fixed spatial orientation, Journal of Electron Spectroscopy and Related Phenomena 21 (4) (1981) 285–363.

[28] D. J. Friedman, F. C. S, Final-state effects in photoelectron diffraction, Journal of Electron Spectroscopy and Related Phenomena 51 (1990) 689 – 700. doi:10.1016/0368-2048(90)80191-C.

[29] M. Sagurton, E. L. Bullock, R. Saiki, A. Kaduwela, C. R. Brundle, C. S. Fadley, J. J. Rehr, Spherical-Wave Effects in Photoelectron Diffraction, Physical Review B 33 (4) (1986) 2207–2213.

[30] S. Kono, S. M. Goldberg, N. Hall, C. S. Fadley, Chemisorption geometry of c(2x2) oxygen on Cu (001) from angle-resolved core-level x-ray photoemission, Physical Review B 22 (1980) 6085.

[31] P. J. Orders, C. S. Fadley, Single-scattering cluster calculations and Fourier-transform analyses of normal photoelectron diffraction, Physical Review B 27 (1983) 781.

[32] J. C. Slater, An augmented plane wave method for the periodic potential problem, Physical Review 92 (3) (1953) 603.

[33] L. F. Mattheiss, Energy bands for the iron transition series, Physical Review 134 (4A) (1964) A970.

[34] T. L. Loucks, Augmented Plane Wave Method: A Guide to Performing Electronic Structure Calculations, W.A. Benjamin, Inc., New York, 1967.

[35] T. Mayer-Kuckuk, Physik der Atomkerne Eine Einführung, 2nd Edition, B. G. Teubner, 1974.

[36] J. M. de Leon, J. J. Rehr, C. R. Natoli, C. S. Fadley, J. Osterwalder, Spherical-wave corrections in photoelectron diffraction, Physical Review B 39 (9) (1989) 5632.

[37] J. J. Rehr, R. C. Albers, C. R. Natoli, E. A. Stern, New high-energy approximation for X-ray-absorption near-edge structure, Physical Review B 34 (6) (1986) 4350.

[38] J. J. Rehr, R. C. Albers, Scattering-Matrix Formulation of Curved-Wave Multiple-Scattering Theory - Application to X-Ray-Absorption Fine-Structure, Physical Review B 41 (12) (1990) 8139–8149.

[39] M. Hösch, Photoemission from Oriented Orbitals, Master's thesis, University of Zurich (Sep. 2006).

[40] M. Hösch, Basic ingredients for oriented SSC, Private Communications.

[41] J. J. Sakurai, Modern Quantum Mechanics, The Benjamin/Cummings Publishing Company, Inc., Menlo Park, 1985.

[42] X. F. Li, X F, A. L'Huillier, M. FERRAY, L. A. LOMPRE, G. MAINFRAY, Multiple-Harmonic Generation in Rare-Gases at High Laser Intensity, Physical Review A 39 (11) (1989) 5751–5761.

[43] Z. Huang, K.-J. Kim, Review of x-ray free-electron laser theory, Physical Review Special Topics - Accelerators and Beams 10 (3) (2007) 034801.

[44] B. Patterson, R. Abela, H.-H. Braun, R. Ganter, B. Pedrini, M. Pedrozzi, S. Reiche, M. Van Daalen, Ultrafast phenomena at the nanoscale: Novel science opportunities at the swissfel X-ray laser, Europhysics News 41 (5) (2010) 28–32.

[45] R. Locher, M. Lucchini, J. Herrmann, M. Sabbar, M. Weger, A. Ludwig, L. Castiglioni, M. Greif, M. Hengsberger, L. Gallmann, U. Keller, Versatile attosecond beamline in a two-foci configuration for simultaneous time-resolved measurements, Review of Scientific Instruments 85 (2014) 013113. doi:10.1063/1.4862656.

[46] U. Bovensiepen, Coherent and incoherent excitations of the Gd(0001) surface on ultrafast timescales, Journal of Physics: Condensed Matter 19 (8) (2007) 083201.

[47] B. Rethfeld, A. Kaiser, M. Vicanek, G. Simon, Ultrafast dynamics of nonequilibrium electrons in metals under femtosecond laser irradiation, Physical Review B 65 (21) (2002) 214303.

[48] U. Bovensiepen, H. Petek, M. Wolf (Eds.), P. Hofmann, E. Chulkov, I. Sklyadneva in Dynamics at Solid State Sufraces and Interfaces, Vol. 1, Wiley-VCH Verlag, Weinheim, Germany, 2010.

[49] C. Kirkegaard, T. K. Kim, P. Hofmann, Self-energy determination and electron–phonon coupling on Bi(110), New Journal of Physics 7 (2005) 99–99.

[50] R. Locher, Attosecond photoemission dynamics from noble metal surfaces, Ph.D. thesis, ETH Zurich (2013).

[51] D. Leuenberger, H. Yanagisawa, S. Roth, J. Osterwalder, M. Hengsberger, Disentanglement of electron dynamics and space-charge effects in time-resolved photoemission from h-BN/Ni(111), Phys. Rev. B 84 (2011) 125107. doi:10.1103/PhysRevB.84.125107.

[52] Specs, Phoibos WAL - Wide Angle Lens Hemispherical Energy Analyzer Release 3, Specs, manual version 3.0 Edition (2012).

[53] T. Greber, O. Raetzo, T. J. Kreutz, P. Schwaller, W. Deichmann, E. Wetli, J. Osterwalder, A photoelectron spectrometer for k-space mapping above the Fermi level, Review of Scientific Instruments 68 (1997) 4549–4554. doi:10.1063/1.1148429.

[54] Focus, VUV HIS 13 Manual, Focus, 1st Edition (1997).

[55] C. Spielmann, N. H. Burnett, S. Sartania, R. Koppitsch, M. Schnurer, C. Kan, M. Lenzner, P. Wobrauschek, F. Krausz, Generation of coherent X-rays in the water window using 5-femtosecond laser pulses, Science 278 (1997) 661–664. doi:10.1126/science.278.5338.661.

[56] M. Greif, L. Castiglioni, D. Becker-Koch, J. Osterwalder, M. Hengsberger, Journal of Electron Spectroscopy and Related Phenomena, Journal of Electron Spectroscopy and Related Phenomena 197 (2014) 30–36.

[57] D. Eastman, J. Donelon, N. Hien, F. Himpsel, An ellipsoidal mirror display analyzer system for electron energy and angular measurements, Nuclear Instruments and Methods 172 (1980) 327 – 336. doi:10.1016/0029-554X(80)90655-2.

[58] H. Daimon, Y. Tezuka, A. Otaka, N. Kanada, S. Lee, S. Ino, H. Namba, H. Kuroda, Two-dimensional photoelectron diffraction patterns by display-type spherical mirror analyzer, Surface Science 242 (1991) 288 – 293. doi:10.1016/0039-6028(91)90281-V.

[59] H. Daimon, F. Matsui, Two-dimensional angle-resolved photoelectron spectroscopy using display analyzer—atomic orbital analysis and characterization of valence band, Progress in Surface Science 81 (2006) 367 – 386. doi:10.1016/j.progsurf.2006.05.001.

[60] L. Tóth, H. Matsuda, F. Matsui, K. Goto, H. Daimon, Details of 1π sr wide acceptance angle electrostatic lens for electron energy and two-dimensional angular distribution analysis combined with real space imaging, Nuclear Instruments and Methods in Physics Research Section A: Accelerators, Spectrometers, Detectors and Associated Equipment 661 (2012) 98 – 105. doi:10.1016/j.nima.2011.09.018.

[61] H. Matsuda, K. Goto, L. Toth, M. Morita, S. Kitagawa, F. Matsui, M. Hashimoto, C. Sakai, T. Matsushita, H. Daimon, Development of display-type ellipsoidal mesh analyzer: Computational evaluation and experimental validation, Journal of Electron Spectroscopy and Related Phenomena (2014) –doi:10.1016/j.elspec.2014.05.001.

[62] R. Leckey, J. Riley, A toroidal angle-resolving electron spectrometer for surface studies, Applications of Surface Science 22–23, Part 1 (1985) 196 – 205. doi:10.1016/0378-5963(85)90052-2.

[63] L. Broekman, A. Tadich, E. Huwald, J. Riley, R. Leckey, T. Seyller, K. Emtsev, L. Ley, First results from a second generation toroidal electron spectrometer, Journal of Electron Spectroscopy and Related Phenomena 144–147 (2005) 1001 – 1004, proceeding of the Fourteenth International Conference on Vacuum Ultraviolet Radiation Physics. doi:j.elspec.2005.01.022.

[64] D. Shirley, High-resolution X-ray photoemission spectrum of the valence bands of gold, Physical Review B 5 (1972) 4709–4714. doi:10.1103/PhysRevB.5.4709.

[65] L. Weng, G. Vereecke, M. J. Genet, P. Bertrand, W. E. E. Stone, Quantitative XPS Part I: Experimental Determination of the Relative Analyzer Transmission Function of Two Different Spectrometers - A Critical Assessment of Various Methods, Parameters Involved and Errors Introduced, Surface and Interface Analysis 20 (1993) 179–192. doi:10.1002/sia.740200302.

[66] H. Aebischer, T. Greber, J. Osterwalder, A. Kaduwela, D. Friedman, G. Herman, C. Fadley, Material dependence of multiple-scattering effects associated with photoelectron and auger electron diffraction along atomic chains, Surface Science 239 (1990) 261 – 264. doi:10.1016/0039-6028(90)90229-2.

[67] F. García de Abajo, M. Van Hove, C. Fadley, Multiple scattering of electrons in solids and molecules: A cluster-model approach, Physical Review B 63 (7) (2001) 075404.

[68] J. Osterwalder, Fermi surface mapping by photoemission, Surface Review and Letters 4 (1997) 391–408. doi:10.1142/S0218625X97000390.

[69] D. P. Woodruff, Surface structural information from photoelectron diffraction, Journal of Electron Spectroscopy and Related Phenomena 178-179 (2010) 186–194.

[70] D. Naumovic, A. Stuck, T. Greber, J. Osterwalder, L. Schlapbach, Full-Hemispherical Photoelectron-Diffraction Data From Cu(001) - Energy-Dependence and Comparison with Single-Scattering-Cluster Simulations, Physical Review B 47 (12) (1993) 7462–7479.

[71] M.-H. Shang, M. Nagaosa, S.-i. Nagamatsu, S. Hosoumi, S. Kera, T. Fujikawa, N. Ueno, Photoemission from valence bands of transition metal-phthalocyanines, Journal of Electron Spectroscopy and Related Phenomena 184 (2011) 261–264.

[72] P. Puschnig, S. Berkebile, A. J. Fleming, G. Koller, K. Emtsev, T. Seyller, J. D. Riley, C. Ambrosch-Draxl, F. P. Netzer, M. G. Ramsey, Reconstruction of Molecular Orbital Densities from Photoemission Data, Science 326 (5953) (2009) 702–706.

[73] P. Puschnig, E. M. Reinisch, T. Ules, G. Koller, S. Soubatch, M. Ostler, L. Romaner, F. Tautz, C. Ambrosch-Draxl, M. Ramsey, Orbital tomography: Deconvoluting photoemission spectra of organic molecules, Physical Review B 84 (23).

[74] J. Ziroff, F. Forster, A. Schöll, P. Puschnig, F. Reinert, Hybridization of Organic Molecular Orbitals with Substrate States at Interfaces: PTCDA on Silver, Physical Review Letters 104 (2010) 233004.

[75] C. Stadler, S. Hansen, I. Kröger, C. Kumpf, E. Umbach, Tuning intermolecular interaction in long-range-ordered submonolayer organic films, Nature Physics 5 (2009) 153–158.

[76] C. Stadler, S. Hansen, F. Pollinger, C. Kumpf, E. Umbach, T. L. Lee, J. Zegenhagen, Structural investigation of the adsorption of SnPc on Ag(111) using normal-incidence x-ray standing waves, Physical Review B 74 (3).

[77] J. D. Baran, J. A. Larsson, Structure and Energetics of Shuttlecock-Shaped Tin-Phthalocyanine on Ag(111): A Density Functional Study Employing Dispersion Correction, The Journal of Physical Chemistry C (2012) 120418120133009.

[78] M. Häming, C. Scheuermann, A. Schöll, F. Reinert, E. Umbach, Coverage dependent organic–metal interaction studied by high-resolution core level spectroscopy: SnPc (sub)monolayers on Ag(111), Journal of Electron Spectroscopy and Related Phenomena 174 (1-3) (2009) 59–64.

[79] M. Toader, M. Hietschold, SnPc on Ag(111): A Scanning Tunneling Microscopy Study at the Submolecular Level, The Journal of Physical Chemistry C 115 (25) (2011) 12494–12500.

[80] M. Toader, M. Hietschold, Tuning the Energy Level Alignment at the SnPc/Ag(111) Interface Using an STM Tip, The Journal of Physical Chemistry C 115 (7) (2011) 3099–3105.

[81] G. Attard, C. Barnes, Surfaces, Oxford University Press, 1998.

[82] http://www.turbomole.com.

[83] C. Adamo, V. Barone, Toward reliable density functional methods without adjustable parameters: The PBE0 model, The Journal of Chemical Physics 110 (13) (1999) 6158.

[84] C. Stadler, Strukturuntersuchungen organischer Monolagen auf Ag(111), Ph.D. thesis, University of Würzburg (2009).

[85] F. Reinert, G. Nicolay, S. Schmidt, D. Ehm, S. Hüfner, Direct measurements of the L-gap surface states on the (111) face of noble metals by photoelectron spectroscopy, Physical Review B 63 (2001) 115415.

[86] A. Tamai, A. Seitsonen, F. Baumberger, M. Hengsberger, Z. X. Shen, T. Greber, J. Osterwalder, Electronic structure at the C60/metal interface: An angle-resolved photoemission and first-principles study, Physical Review B 77 (7) (2008) 075134.

[87] C. H. Schwalb, M. Marks, S. Sachs, A. Schöll, F. Reinert, E. Umbach, U. Höfer, Time-resolved measurements of electron transfer processes at the PTCDA/Ag(111) interface, The European Physical Journal B 75 (1) (2010) 23–30.

[88] M. Häming, M. Greif, C. Sauer, A. Schöll, F. Reinert, Electronic structure of ultrathin heteromolecular organic-metal interfaces: SnPc/PTCDA/Ag(111) and SnPc/Ag(111), Physical Review B 82 (23) (2010) 235432.

[89] P. Aebi, J. Osterwalder, R. Fasel, D. Naumovic, L. Schlapbach, Fermi surface mapping with photoelectrons at UV energies, Surface Science 307 (1994) 917–921.

[90] O. K. Andersen, Z. Pawlowska, O. Jepsen, Illustration of the linear-muffin-tin-orbital tight-binding representation: Compact orbitals and charge density in Si, Physical Review B 34 (8) (1986) 5253–5269.

[91] P. Hofmann, The surfaces of bismuth: Structural and electronic properties, Progress In Surface Science 81 (2006) 191–245.

[92] R. Peierls, More Surprises in Theoretical Physics, Princeton University Press, Princeton, 1991.

[93] T. K. Cheng, J. Vidal, H. J. Zeiger, G. Dresselhaus, M. S. Dresselhaus, E. P. Ippen, Mechanism for displacive excitation of coherent phonons in Sb, Bi, Te, and Ti2O3, Applied Physics Letters 59 (1991) 1923.

[94] D. M. Fritz, D. A. Reis, B. Adams, R. A. Akre, J. Arthur, C. Blome, P. H. Bucksbaum, A. L. Cavalieri, S. Engemann, S. Fahy, R. W. Falcone, P. H. Fuoss, K. J. Gaffney, M. J. George, J. Hajdu, M. P. Hertlein, P. B. Hillyard, M. Horn-von Hoegen, M. Kammler, J. Kaspar, R. Kienberger, P. Krejcik, S. H. Lee, A. M. Lindenberg, B. McFarland, D. Meyer, T. Montagne, E. D. Murray, A. J. Nelson, M. Nicoul, R. Pahl, J. Rudati, H. Schlarb, D. P. Siddons, K. Sokolowski-Tinten, T. Tschentscher, D. von der Linde, J. B. Hastings, Ultrafast Bond Softening in Bismuth: Mapping a Solid's Interatomic Potential with X-rays, Science 315 (2007) 633–636.

[95] D. Fausti, Phase transitions and optically induced phenomena in cooperative systems, Ph.D. thesis, University of Groningen (2008).

[96] M. Hase, M. Kitajima, S.-I. Nakashima, K. Mizoguchi, Dynamics of Coherent Anharmonic Phonons in Bismuth Using High Density Photoexcitation, Physical Review Letters 88 (6) (2002) 067401.

[97] M. Hase, K. Mizoguchi, H. Harima, S. Nakashima, K. Sakai, Dynamics of coherent phonons in bismuth generated by ultrashort laser pulses, Physical Review B 58 (9) (1998) 5448–5452.

[98] U. Bovensiepen, H. Petek, M. Wolf (Eds.), M. Hase, O. Misochko, K. Ishioka in Dynamics at Solid State Sufraces and Interfaces, Vol. 1, Wiley-VCH Verlag, Weinheim, Germany, 2010.

[99] E. Papalazarou, J. Faure, J. Mauchain, M. Marsi, A. Taleb-Ibrahimi, I. Reshetnyak, A. van Roekeghem, I. Timrov, N. Vast, B. Arnaud, L. Perfetti, Coherent Phonon Coupling to Individual Bloch States in Photoexcited Bismuth, Physical Review Letters 108 (25) (2012) 256808.

[100] D. Leuenberger, H. Yanagisawa, S. Roth, J. Dil, J. Wells, P. Hofmann, J. Osterwalder, M. Hengsberger, Excitation of Coherent Phonons in the One-Dimensional Bi(114) Surface, Physical Review Letters 110 (13) (2013) 136806.

[101] C. Ast, H. Höchst, Fermi Surface of Bi(111) Measured by Photoemission Spectroscopy, Physical Review Letters 87 (17) (2001) 177602.

[102] A. Tanaka, M. Hatano, K. Takahashi, H. Sasaki, S. Suzuki, S. Sato, Bulk and surface electronic structures of the semimetal Bi studied by angle-resolved photoemission spectroscopy, Physical Review B 59 (3) (1999) 1786.

[103] G. Jezequel, Y. Petroff, R. Pinchaux, F. Yndurain, Electronic-Structure of the Bi(111) Surface, Physical Review B 33 (6) (1986) 4352–4355.

[104] Y. Liu, R. E. Allen, Electronic structure of the semimetals Bi and Sb, Physical Review B 52 (3) (1995) 1566.

[105] R. M. Goodman, Low-Energy Electron Diffraction Studies of Surface Melting and Freezing of Lead, Bismuth, and Tin Single-Crystal Surfaces, The Journal of Chemical Physics 52 (12) (1970) 6325.

[106] G. Ertl, M. Neumann, K. Streit, Chemisorption of {CO} on the pt(111) surface, Surface Science 64 (2) (1977) 393 – 410. doi:http://dx.doi.org/10.1016/0039-6028(77)90052-8.

[107] H. Steininger, S. Lehwald, H. Ibach, On the adsorption of {CO} on pt(111), Surface Science 123 (2–3) (1982) 264 – 282. doi:http://dx.doi.org/10.1016/0039-6028(82)90328-4.

[108] A. P. Graham, The low-frequency vibrational modes of c(4×2) CO on Pt(111), The Journal of Chemical Physics 109 (21) (1998) 9583.

[109] P. Deshlahra, J. Conway, E. E. Wolf, W. F. Schneider, Influence of Dipole–Dipole Interactions on Coverage-Dependent Adsorption: CO and NO on Pt(111), Langmuir 28 (22) (2012) 8408–8417.

[110] G. Blyholder, Molecular Orbital View of Chemisorbed Carbon Monoxide, Journal of Physical Chemistry 68 (10) (1964) 2772.

[111] D. A. Wesner, U. Breuer, O. Knauff, H. P. Bonzel, Xpd Studies of Adsorbates and Surface Melting, Physica Scripta T31 (1990) 247–254.

[112] A. Lahee, J. Toennies, C. Wöll, Low energy adsorbate vibrational modes observed with inelastic helium atom scattering: CO on Pt(111), Surface Science 177 (2) (1986) 371 – 388. doi:http://dx.doi.org/10.1016/0039-6028(86)90146-9.

[113] M. P. Allen, D. J. Tildesley, Computer Simulation of Liquids, Oxford UNiversity Press, Oxford, 1991.

[114] B. R. Brooks, R. E. Bruccoleri, B. D. Olafson, D. J. States, S. Swaminathan, M. Karplus, Charmm - a Program for Macromolecular Energy, Minimization, and Dynamics Calculations, Journal of Computational Chemistry 4 (2) (1983) 187–217.

[115] T. Nagy, M. Soloviov, M. Meuwly, Molecular Dynamics Calculations of CO/Pt(111), unpublished.

[116] E. Schweizer, B. N. J. Persson, M. Tüshaus, D. Hoge, A. M. Bradshaw, The potential energy surface, vibrational phase relaxation and the order-disorder transition in the adsorption system Pt111-CO, Surface Science 213 (1) (1989) 49 – 89. doi:http://dx.doi.org/10.1016/0039-6028(89)90252-5.

[117] H. Over, W. Moritz, G. Ertl, Anisotropic Atomic Motions in Structural-Analysis by Low-Energy Electron-Diffraction, Physical Review Letters 70 (3) (1993) 315–318.

[118] V. Krishna, J. C. Tully, Vibrational lifetimes of molecular adsorbates on metal surfaces, The Journal of Chemical Physics 125 (5) (2006) 054706.

[119] M. Head-Gordon, J. C. Tully, Molecular dynamics with electronic frictions, The Journal of Chemical Physics 103 (23) (1995) 10137.

[120] L. Cai, X. D. Xiao, M. Loy, Femtosecond laser desorption of CO from the Pt(111) surface, Surface Science 464 (2-3) (2000) L727–L731.

Acknowledgement

I would like to thank all the people that helped me in this four year long project of my dissertation. Many helped actively and many others mentally by keeping up good fate.
At first I want to thank the people closely involved in my project, of course:
Many thanks go out to Matthias Hengsberger for setting this whole project up, giving the main ideas and helping wherever help was needed, be it in the lab or in numerous discussion. His expertise and knowledge were great to experience and helped so much. Thanks also for creating a nice and fruitful working atmosphere. It was a pleasure to come to work every day, not to forget the nice stays at conferences and MUST retreats.
Thanks also to Jürg Osterwalder, although being busy as head of the group, with his great competence he was always open to questions from my side. It is amazing how he keeps up to date with the numerous projects in the group. So thanks for always caring for the project and helping a lot with the SSC part of it.
I also want to thank Peter Krüger who is not only part of the dissertation committee but helped a lot in my understanding of photoemission processes. Thanks for having me in Dijon, which was a great time.
Thanks also go to Luca Castiglioni. Together we kept WALüre running and as my office mate he endured my presence most of all. I could profit from many fruitful discussions about physics but also about all the rest that drives the world. There is no topic he did not know what to say about.
I am also grateful for the huge amount of help from the ultrafast laser group at ETH in general and from Lamia and Matteo especially. Thanks for long but fruitful shifts at the Attoline.
Thanks also go to all the former and present members of the surface physics group: Thomas Greber, Dominik Leuenberger, who gave me a warm welcome in the first time not only at university but in Zurich in general, Silvan Roth for good times in the lab and outside university, Bartosz Slomski for great times at conferences and outside university, Hugo Dil for letting me use COPHEE for an experiment, Adrian Hemmi, Gabriel Landolt, Martin Morscher, Huanyao Cun, Thomas Kälin, Roland Stania, Carlo Bernhard, Stefan Muff, Adrian Schuler, Rasmus Westerström, Gerson Mette, Aram Kostanyan, Elisa Miniuzzi, Pavlo Kliuiev, Wolf Zabka, Stefan Förster and Claude Monney.
Furthermore I thank Ari Seitsonen for the help with DFT calculations of adsorbed molecules and Anna Butterfiled and Jay Siegel for the help with subliming SnPc molecules.
I am also very grateful for the presence of people outside of University:
Thanks to my good friends Nico, Peter, Stefano and the whole swim team. Swimming was a wonderful counter part to working at university.
I want to thank my parents and my family for preparing me for a venture like this dissertation from my child days on.
Finally and most overwhelmed I thank my great Elli, for being by my side from the very beginning on, for keeping her faith in me and us despite the long distance and thank you for your love.

3. R. Locher, L. Castiglioni, M. Lucchini, M. Greif, L. Gallmann, J. Osterwalder, M. Hengsberger, and U. Keller, Attosecond interferometry unravels complex delays in photoemission from solids, arXive (2014).

4. M. Greif, L. Castiglioni, A. P. Seitsonen, S. Roth, J. Osterwalder, M. Hengsberger, Photoelectron diffraction in the x-ray and ultraviolet regime: Sn-phthalocyanine on Ag (111), Physical Review B 87 (2013) 085429.

5. L. Castiglioni, D. Leuenberger, M. Greif, and M. Hengsberger, Attosecond Transversal Streaking to Probe Electron Dynamics at Surfaces, in K. Yamanouchi and K. Midorikawa (eds.), Multiphoton processes and attosecond physics, Springer Proceedings in Physics 125, pp. 365, Springer (Berlin, Heidelberg) 2012.

6. L. Castiglioni, M. Greif, D. Leuenberger, S. Roth, J. Osterwalder, and M. Hengsberger, Time-Resolved Photoelectron Spectroscopy to Probe Ultrafast Charge Transfer and Electron Dynamics in Solid Surface Systems and at Metal- Molecule Interfaces, CHIMIA 65 (2011) 342.

7. M. Häming, M. Greif, C. Sauer, A. Scholl and F. Reinert, Electronic structure of ultra-thin heteromolecular organic-metal interfaces: SnPc/PTCDA/Ag(111) and SnPc/Ag(111), Physical Review B 82 (23) (2010) 235432.

8. M. Häming, M. Greif, M. Wießner, A. Schöll, and F. Reinert, Characterization of ultra-thin organic hetero-interfaces - SnPc/PTCDA/Ag(111), Surface Science, 604 (2010) 1619.